

Gran Sasso Science Institute  
**MATHEMATICS IN NATURAL, SOCIAL AND LIFE SCIENCES**  
**DOCTORAL PROGRAMME**  
Cycle XXXIII - AY 2017-2020

## **Thermally driven flows in spherical geometries**

PHD CANDIDATE  
**Luca Santelli**

ADVISOR  
**Prof. Roberto Verzicco**  
GSSI & Università di Roma, Tor Vergata







Gran Sasso Science Institute

**MATHEMATICS IN NATURAL, SOCIAL AND LIFE SCIENCES DOCTORAL PROGRAMME**

Cycle XXXIII- AY 2017-2020

---

**THERMALLY DRIVEN FLOWS IN SPHERICAL GEOMETRIES**

---

PhD Candidate

LUCA SANTELLI

Advisor

PROF. ROBERTO VERZICCO

GSSI & Università di Roma, Tor Vergata

Thesis submitted for the degree of Doctor of Philosophy

December 2021

**Thesis Jury Members**

Prof. Giorgio Querzoli (Jury President, Unica)

Dr. Francesco Viola (GSSI)

Prof. Roberto Camussi (Uniroma3)

Prof. Vincenzo Mulone (Uniroma2)

Prof. Mauro Chinappi (Uniroma2)

**Thesis Referees**

Roberto Camusso (Università degli Studi Roma Tre, Dipartimento di energia meccanica e industriale)

Giorgio Querzoli (Università degli Studi di Cagliari, dipartimento di Ingegneria Civile Ambientale e Architettura)

---

## Abstract

---

In this manuscript we describe an efficient numerical scheme for simulations of three-dimensional Navier-Stokes equations for incompressible viscous flows in spherical coordinates. The code is second order accurate in space and time and relies on a finite-difference discretization in space. The nonphysical singularities induced by the change of coordinates are addressed by exploiting a change of variables and special treatments of few discrete terms. Thanks to these precautions the time-step restrictions caused by the region around the polar axis are alleviated and the sphere center is source of limitations only in very unfavorable flow configurations.

We test the code and compare results with literature, always obtaining an excellent agreement. The flexibility due to the structure of the code allows it to perform efficiently in several applications without requiring changes in the structure: the mesh can be stretched (in two of the three directions), complex boundary conditions can be implemented, and in addition to full spheres, also spherical shells and sectors can be easily simulated.

Characterization of the behaviour of fluids between spherical shells is the focus of the second part of the manuscript. We firstly explored the low-Rayleigh number regime for non rotating Rayleigh-Bénard convection. Various radial gravity profiles are analysed for both air and water. We observe how the effect of the different gravity can be reabsorbed by the introduction of an effective Rayleigh number, yielding a critical  $Ra_c \approx 1750$  for the onset of convection regardless of the specific gravity profile. The exploration of higher values of  $Ra$  shows that the system is subjected to hysteresis, i.e. the dynamic has a very strong dependence on initial conditions and flow parameters.

We then explore the effect of an offset between the sphere center and the gravity center, which might be used to simulate the effect of a dishomogeneity in the Earth core. Even a small displacement between the two points gives rise to a distorted temperature profile, with a hot jet emerging from the inner sphere in the direction opposite to the shift. Nevertheless, while the local heat flux and temperature profile are greatly modified, the global heat flux seems to be mostly unaffected by these changes.

Lastly, we analysed the diffusion-free scaling regime for slowly rotating Rayleigh-Bénard convection between spherical shells. This regime is characterized by a bulk-dominated flow and its emergence, for the parameters used, is due to the peculiar properties of the spherical geometry.



# Contents

<b>1</b>	<b>Introduction</b>	<b>1</b>
1.1	Properties of fluids . . . . .	1
1.2	Study of a flow field . . . . .	2
1.3	Navier–Stokes equation . . . . .	2
1.4	Thermal convection . . . . .	3
1.4.1	Model of convection: Boussinesq approximation . . . . .	5
1.5	Computational Fluid Dynamics . . . . .	6
1.5.1	Fractional time step discretization . . . . .	7
1.6	Thesis overview . . . . .	8
<b>2</b>	<b>A finite-difference scheme for three-dimensional incompressible flows in spherical coordinates</b>	<b>11</b>
2.1	Introduction . . . . .	11
2.2	Equations . . . . .	14
2.3	Variable discretization . . . . .	16
2.4	Numerical method . . . . .	19
2.5	Validation . . . . .	20
2.5.1	Hill vortex . . . . .	20
2.5.2	Flow in a precessing and spinning sphere . . . . .	25
2.5.3	Rayleigh–Bénard convection with vertical gravity . . . . .	27
2.5.4	Rayleigh–Bénard convection with central gravity . . . . .	28
2.5.5	Space-developing jet . . . . .	30
2.6	Concluding remarks . . . . .	32
<b>3</b>	<b>Effect of gravity profiles on Rayleigh–Bénard convection in spherical shells</b>	<b>35</b>
3.1	Introduction . . . . .	35
3.2	Numerical simulation . . . . .	37
3.2.1	Problem description . . . . .	37
3.2.2	Numerical setup . . . . .	39
3.3	Results . . . . .	41
3.3.1	Onset of convection . . . . .	41
3.3.2	Non-stationary convection . . . . .	44
3.3.3	Hysteresis . . . . .	47
3.3.4	Higher Pr Number . . . . .	50
3.4	Concluding remarks . . . . .	51

<b>4 Off-center gravity induces large-scale flow patterns in spherical Rayleigh-Bénard</b>	<b>53</b>
4.1 Introduction . . . . .	53
4.2 Numerical method and parameters . . . . .	54
4.2.1 Numerical method . . . . .	55
4.2.2 Considered parameter regime . . . . .	56
4.3 Results . . . . .	57
4.3.1 Generation of convective jet and large-scale circulation . .	57
4.3.2 Modal analysis to identify large-scale structures . . . . .	59
4.3.3 Modulation of temperature distribution and heat-transfer rate . . . . .	61
4.3.4 Additional parameters: $n_g$ and $Ra$ . . . . .	62
4.4 Concluding remarks . . . . .	63
<b>5 Diffusion-free scaling in rotating spherical Rayleigh-Bénard convection</b>	<b>67</b>
5.1 Introduction . . . . .	67
5.2 Numerical method, control and response parameters . . . . .	69
5.3 Heat transfer in rotating spherical RB convection . . . . .	71
5.4 Identification of three flow regimes . . . . .	72
5.5 Diffusion-free scaling in region II . . . . .	74
5.6 Conclusions . . . . .	75
<b>6 Conclusions</b>	<b>77</b>
<b>A Harmonic analysis and spectrum</b>	<b>81</b>
A.1 Fourier decomposition . . . . .	81
A.2 Spherical harmonic decomposition . . . . .	81
<b>B Transformation of gravity center to any random point</b>	<b>83</b>
<b>C Supporting Information for Chapter 5</b>	<b>85</b>
C.1 Simulation details . . . . .	85
C.2 Grid independence and longitudinal domain size . . . . .	88
C.3 Line Integral Convolution for spherical surfaces . . . . .	89
C.4 Diffusive free region for $\eta = 0.35$ and $n_g = -1$ . . . . .	90

# List of Figures

1.1	Examples of thermal convection in nature. (a) Outer core convection, primary candidate for the dynamo effect related to Earth's magnetic field. (b) Convection in the mantle, responsible of tectonic plates motion. (c) Convection cells in the atmosphere. (d) Convection in the interior of the Sun. Images from the web, links are provided by clicking the corresponding alphabets. . . . .	4
2.1	Sketch of the system and coordinate definition. . . . .	12
2.2	a) Staggered arrangement of the discrete variables and cells next to the sphere centre. b) Cells near the North pole of the sphere. . . . .	17
2.3	a) Sketch of the Hill vortex setup in the longitudinal sections $\theta = 0, \pi$ of the spherical domain. b) Time evolution of the vortex centre coordinates for the case at $Re = 2500$ with $\theta_C = \pi$ , $r_C = 1$ , $\phi_C = \pi/2$ . —— $X_C = r_C \cos \theta_C \sin \phi_C$ , ---- $X_C$ from the code in Cartesian coordinates [157], thin ..... theoretical $X_C$ ; ---- $Y_C = r_C \sin \theta_C \sin \phi_C$ ; —— $Z_C = r_C \cos \phi_C$ . . . . .	21
2.4	Time evolution of the Hill vortex at $Re = 2500$ in the longitudinal sections $\theta = 0, \pi$ ; longitudinal vorticity ( $\Delta\omega_\theta = \pm 0.4$ ) ..... for negative values; a) ) $t = 0.5$ , b) $t = 1.$ , c) $t = 1.5$ . Initial centre of the vortex: $\theta_C = \pi$ , $r_C = 1$ , $\phi_C = \pi/2$ . Hereinafter, the black bullet indicates the origin of the spherical system. . . . .	22
2.5	Time evolution of the Hill vortex at $Re = 2500$ evolved on a Cartesian uniform mesh; out-of-the-page vorticity ( $\Delta\omega = \pm 0.4$ ) ..... for negative values; a) ) $t = 0.5$ , b) $t = 1.$ , c) $t = 1.5$ . . . . .	23
2.6	a) Decay of the total kinetic energy in time for the Hill vortex: —— results from the code in spherical coordinates --- results from the Cartesian code [157]. In the inset: —— and $Re = 2500$ for the Hill vortex with initial offset. —— and $Re = 2500$ for the Hill vortex resolved on a mesh refined around the singular points. b) $L_2$ -norm of the error as function of the mesh size for the case at $Re = 2500$ . ---- 2-slope, ..... 1-slope. $\bar{\Delta}$ is the mean grid spacing defined as $\bar{\Delta} \equiv [V/(N_i N_j N_k)]^{1/3}$ with $V$ the volume of the computational domain. $\theta_C = \pi$ , $r_C = 1$ , $\phi_C = \pi/2$ . . . . .	23

2.7	Time evolution of the Hill vortex at $Re = 2500$ in the longitudinal sections $\theta = 0, \pi$ ; top panels show longitudinal vorticity ( $\Delta\omega_\theta = \pm 0.4$ ) ..... for negative values; ( $\Delta u = 0.1$ ) bottom panels for pressure ( $\Delta p = 0.02$ ); the background mesh is shown with light gray lines. a) and d) $t = 0.5$ , b) and e) $t = 1.$ , c) and f) $t = 1.5$ . Initial centre of the vortex: $\theta_C = \pi$ , $r_C = 1$ , $\phi_C = 2\pi/3$ . . . . .	24
2.8	a) Zoom of velocity magnitude ( $\Delta u = 0.1$ ) of a Hill vortex at $Re = 2500$ and $t = 1$ in the longitudinal sections $\theta = 0, \pi$ ; the computational mesh is refined on purpose around the singular points. b) Time evolution of the maximum divergence of the velocity field. Initial centre of the vortex: $\theta_C = \pi$ , $r_C = 1$ , $\phi_C = \pi/2$ . . . . .	25
2.9	Flow in a precessing, spinning sphere at $\Gamma = 0.1$ and $Re = 500$ . The velocity vectors of the field rotating with the spinning sphere $\mathbf{v}$ are reported in the sections $z = -0.66$ , a) and d); $z = -0.33$ , b) and e); $z = 0$ , c) and f). The contours are for the velocity component $v_z$ . a), c) and e) are the results adapted from Fig. 7 of [12], b) ,d) and f), present results. . . . .	26
2.10	a) Section through the meridional planes $\theta = 0, \pi$ of temperature contours ( $\Delta T = 0.1$ ) for the flow at $\eta = R_i/R_o = 0.5$ , $Ra = 10^5$ and $Pr = 0.7$ . Grid $65 \times 49 \times 49$ . b) Time evolution of the Nusselt numbers — simulation with the gravity aligned with the polar axis, - - - gravity perpendicular to the polar axis, - - - reference value of $Nu = 3.4012$ from [42]. . . . .	28
2.11	a) Section through the meridional planes $\theta = 0, \pi$ of temperature contours ( $\Delta T = 0.1$ ) overlaid with velocity vectors for the flow at $\eta = R_i/R_o = 0.6$ , $Ra = 3 \times 10^4$ and $Pr = 1$ . Grid $129 \times 97 \times 97$ . b) Time evolution of the Nusselt numbers: — value computed at the inner surface, — value computed at the outer surface, — value computed from $\epsilon_u$ , — value computed from $\epsilon_T$ . . . . .	29
2.12	a) Computational set-up for the space developing jet. The isosurface is velocity magnitude $ \mathbf{u}  = 0.2$ . b) Instantaneous snapshot plane section ( $\theta = (\Theta_i + \Theta_f)/2$ ) of velocity magnitude (from blue to red) $\Delta  \mathbf{u}  = 0.1$ . . . . .	31
3.1	Sketch of the configuration. . . . .	37
3.2	Overview of the dimensionless gravity profiles used (summarised in table 3.1) as a function of radius: - - - quadratic gravity; — parabolic gravity; - - - mantle-like gravity; - - - linear gravity. . . . .	38
3.3	Analysis of $Nu$ vs $t$ at different number of grid points. — grid with ( $N_\theta = 33, N_r = 35, N_\phi = 35$ ) points; - - - (65, 69, 69); - - - (129, 121, 121). Only a small mismatch at the beginning of the simulation is present for the less refined grid, while the other two are almost coincident at every step. A vertical black line separate the two different $Ra$ analysed: $Ra = 1600$ for $t < 5000$ , $Ra = 1500$ after. . . . .	39

3.4	Evolution of $Nu$ as function of $t$ . Vertical bars of (a) and (b) separate zones with different $Ra$ . . . . .	41
3.5	Evolution of $Nu$ as function of $Ra$ . ♦ red diamonds for increasing- $Ra$ , • black circles for decreasing- $Ra$ . Error bars shown when bigger than the symbols. . . . .	42
3.6	Temperature profile (a,c,e) and spherical harmonic spectrum (b,d,f) for quadratic gravity in various situations. Temperature ranges from yellow (hotter) to blue (colder). For spectra, — for $C_l$ and reference scale on the left; ..... for $C_m$ and reference scale on the right. . . . .	43
3.7	Analysis of quadratic gravity at $Ra_1 = 1700$ . In figure (a) the time needed for stabilising is approximately $t_s \approx 1.2 \times 10^4$ . Temperature of figures (b,c) ranges from yellow (hotter) to blue (colder). For spectra (d,e): — for $C_l$ and reference scale on the left; ..... for $C_m$ and reference scale on the right. . . . .	45
3.8	Analysis of quadratic gravity at $Ra_2 = 2100$ . Temperature of figure (b) ranges from yellow (hotter) to blue (colder). For the harmonic spectrum (d): — for $C_l$ and reference scale on the left; ..... for $C_m$ and reference scale on the right. . . . .	46
3.9	Analysis of quadratic gravity at $Ra = 5000$ (a,b,e,f) and $Ra = 10000$ (c,d,g,h). Temperature of figures (e,g) ranges from yellow (hotter) to blue (colder). For the harmonic spectra (f,h): — for $C_l$ and reference scale on the left; ..... for $C_m$ and reference scale on the right. . . . .	48
3.10	On the left, comparisons for different initial conditions (vertical black lines in (a,c) indicate changes in $Ra$ ); on the right, behaviour around $Ra_2$ . (a): — decreasing case (with reversed time scale) starting from $Ra > Ra_1$ ; ..... increasing case starting from $Ra_c$ . (b): — oscillating state; ..... rest state; —— region II state. (c): — decreasing case starting at $Ra < Ra_2$ ; ..... decreasing case starting at $Ra > Ra_2$ . Temperature of figure (d) ranges from yellow (hotter) to blue (colder). For the harmonic spectra (e,f): — for $C_l$ and reference scale on the left; ..... for $C_m$ and reference scale on the right. . . . .	49
4.1	Schematic of spherical Rayleigh-Bénard convection in between two concentric spheres with radius ratio $\eta = r_i/r_o$ between the inner and outer sphere and gap size $d = r_o - r_i$ . A no-slip boundary condition with constant temperature is used on the inner and outer sphere. In spherical coordinates the longitudinal, co-latitudinal, and radial directions are represented by $\hat{\theta}$ , $\hat{\varphi}$ and $\hat{r}$ , respectively. $G$ indicates the gravity center, which is offset from the geometric center $O$ , and point $P$ indicates an arbitrary fluid parcel. . . . .	54

- 4.2 The temperature isosurface for  $T = 0.3$  is indicated in white, while the color indicates the temperature field in the equatorial plane and two meridian cuts for  $Ra = 3 \times 10^7$  and  $n_g = 0$ . (a-f) correspond to  $\varepsilon = 0, 0.1, 0.2, 0.4, 0.6$  and  $0.8$ , respectively. . . . . 59
- 4.3 (a) Mean temperature  $\langle T \rangle(r, \varphi)$  in the meridian plane for  $Ra = 3 \times 10^7$ ,  $n_g = 0$ , and  $\varepsilon = 0.8$ . (b) Instantaneous velocity in the meridian plane for  $Ra = 3 \times 10^7$ ,  $n_g = 0$ , and  $\varepsilon = 0.8$  colored by temperature; (c) Schematic illustration of gravity decomposition  $\mathbf{g} = \mathbf{g}_{\text{PO}} + \mathbf{g}_{\text{PO},\perp}$  when the gravity center  $G$  does not coincide with the geometrical center  $O$ . . . . . 60
- 4.4 (a) Volume averaged  $Re_{rms}(\varepsilon)/Re_{rms}(\varepsilon = 0)$  as a function of  $\varepsilon$  for  $Ra = 3 \times 10^7$  and  $n_g = 0$ . The error bars indicate the corresponding standard deviations. We note the standard error is smaller than the symbol size. (b) TKE Spectrum of  $\langle C_m \rangle$ , normalized by  $\langle C_{m=1} \rangle$ , as a function of the spherical harmonic order  $m$  for different  $\varepsilon$ . . . . . 60
- 4.5 (a) Mean temperature  $\langle T \rangle(r, \varphi)$  in the meridian plane for  $Ra = 3 \times 10^7$ ,  $n_g = 0$ , and  $\varepsilon = 0, 0.1, 0.4$ , and  $0.8$ . Panel (b) shows mean temperature profiles at different co-latitudinal locations for  $\varepsilon = 0.8$ . 61
- 4.6 (a)  $Nu$  number on the inner and (b) outer sphere as a function of the co-latitudinal direction for  $Ra = 3 \times 10^7$  and  $n_g = 0$ . . . . . 62
- 4.7 (a)  $Nu(\varepsilon)/Nu(\varepsilon = 0)$  as a function of  $\varepsilon$  for (a)  $Ra = 3 \times 10^7$  and (b)  $Ra = 7 \times 10^6$  and different gravity profiles. The error bars indicate the standard deviations of the  $Nu$  values averaged over the inner and outer sphere. We note the standard error and the  $Nu$  difference between the inner and outer sphere are both smaller than the symbol size so that they are not visible. . . . . 63
- 4.8 Instantaneous isosurface of  $T = 0.3$  for different gravity distributions from  $n_g = 1$  to  $n_g = -2$  (see equation 4.6) for  $Ra = 7 \times 10^6$  and  $\varepsilon = 0.8$ . The rightmost panel shows  $Ra = 3 \times 10^7$ ,  $n_g = 0$ , and  $\varepsilon = 0.8$  for comparison. The color represents for velocity magnitude at the isosurface. . . . . 64
- 4.9 TKE spectrum for different gravity profiles when  $\varepsilon = 0.8$ : (a) normalized by  $\langle C_{m=1} \rangle$ ; (b) normalized by  $\langle C_m \rangle(n_g = 1)$ . . . . . 64
- 4.10 TKE spectrum for different  $Ra$  when  $\varepsilon = 0.8$ : (a) normalized by  $\langle C_{m=1} \rangle$ ; (b) normalized by  $\langle C_m \rangle(Ra = 7 \times 10^6)$ . . . . . 64

5.1 Schematics showing the alignment of the axial convective columns in (a) canonical framework heated from bottom and cooled from above and (b) spherical rotating RB convection heated from inner and cooled from outer, in which the gravity points towards the geometrical centre. The longitudinal (azimuthal), co-latitudinal (polar), and radial directions are represented by $\hat{\theta}$ , $\hat{\varphi}$ and $\hat{r}$ , respectively. The rotation axis aligns with the $z$ -direction. The angle between gravity and rotation axis is $\varphi$ . The tangent cylinder is shown with dashed-dotted grey line. Panel (b) is adapted from [22, 23, 10]. . . . .	69
5.2 $Nu$ as function of $Ra$ for different $Ek$ . Rotating cases: open symbols indicate the present results, filled-in symbols are those from [50]. Non-rotating cases from [49] are indicated by $Ek = \infty$ . The shaded wedge-shaped region indicates the diffusion-free scaling regime ( $6Ek^{4/3} \leq Ra \leq 0.4Ek^{-8/5}$ ), which corresponds to the quasi-geostrophic regime identified by [50]. The dot-dashed grey line gives the diffusion-free scaling $Nu = 0.149R^{3/2}$ for $Ek = 3 \times 10^{-6}$ . The error bars are smaller than the symbol sizes. . . . .	71
5.3 (a) Contour of the temperature fluctuation $T'$ on two meridional cuts, equatorial section, and two spherical surfaces (corresponding to the surface located at the inner ( $r = r_i + \lambda_{T,i}$ ) and outer ( $r = r_o - \lambda_{T,o}$ ) thermal boundary layers. (b) Contour of $T'$ with streamlines illustrated by using line integral convolution on the outer radial surface. The definition of the three regimes I, II, III is given in the text and figure 5.4. (c) $Nu$ as function of the co-latitude $\varphi$ on the outer sphere. In all cases (a)-(c), $Ek = 1 \times 10^{-5}$ and $Ra = 5 \times 10^7$ . . . . .	72
5.4 (a) Cylindrical polar coordinates $(z, z_\perp, \theta)$ , $z$ is the rotation axis, $z_\perp$ is the cylindrical radius and $\theta$ is the azimuthal angle and of which the regimes I, II, III can be defined as shown. (b) Ensemble averaged azimuthal velocities $U_\theta$ (zonal flows) as a function of $z_\perp$ in equation (5.6). $(z_\perp - r_i)/d = 0$ and 1 correspond to the tangent cylinders of the inner and outer spheres, respectively. $\varphi_2$ is determined by the $z_\perp$ location close to the outer sphere ( $(z_\perp - r_i)/d = 1$ ) where the zonal flow is strongest. (c) Time and Azimuthal averaged thermal dissipation $\overline{(\nabla T)^2}_\theta$ in the meridional plane for case No.76 of $Ek = 1 \times 10^{-5}$ and $Ra = 5 \times 10^7$ . (d) Pie chart for (c) showing the distribution of the thermal dissipation rate over the different regions in the boundary layer and bulk, see equation (5.8). . . . .	73
5.5 $Nu$ on the outer sphere compensated by $R^{-3/2}$ and as a function of $R \equiv RaEk^{4/3}$ . (a) Integration over the whole sphere; (b-d) $Nu$ in regions (I – III), see figure 5.3(b). The symbols have the same meaning as in figure 5.2. . . . .	75

5.6	$Nu$ compensated by $R^{-3/2}$ as a function of $RaEk^{8/5}$ . (a) Integration over the whole sphere. The horizontal line is $NuR^{-3/2} = 0.149$ and the vertical line is $RaEk^{8/5} = 0.4$ ; (b) Region II. The horizontal line is $NuR^{-3/2} = 0.105$ and the vertical line is $RaEk^{8/5} = 1$ . The symbols have the same meaning as in figure 5.2. . . . .	76
B.1	Schematic figure of the two-step transformation of a vector <b>GP</b> in Cartesian coordinate $xyz$ to spherical coordinate $\varphi\theta r (x''y''z'')$ frame. Circular arrows about $z'$ -axis and $y'$ -axis show rotating axis. . . . .	83
C.1	Grid convergence test for case No.76. $Nu$ as function of (a) the longitudinal number of grid point $N_\theta$ ; (b) the radial number of grid points $N_r$ ; (c) and the co-latitudinal number of grid points $N_\varphi$ . The dotted line in (a-c) indicates $Nu = 5.103$ obtained using $N_\theta \times N_r \times N_\varphi = 251 \times 111 \times 451$ . (d,e) Corresponding $T_{rms}$ and $u_{r,rms}$ profiles as a function of radial direction, which show that higher order statistics are also converged. . . . .	89
C.2	Number of rotational symmetry order $n_s$ tests for $\langle T \rangle$ (a,c) and $\langle T_{rms} \rangle$ (b,d) as a function of radial direction for case No.76 (a,b) and case No.80 (c,d). . . . .	90
C.3	Resolution and CFL number tests for case No.76 of $Ek = 1 \times 10^{-5}$ , $Ra = 5 \times 10^7$ . Time and azimuthal averaged $Nu$ as function of the co-latitude $\varphi$ on the outer sphere. . . . .	91
C.4	Schematic process of line integral convolution (LIC) computation for a 2D non-rotating RB flow: {vector field $\rightarrow$ streamline} + {input texture (white noise)} $\rightarrow$ {output texture (pixel grey level determined by the streamline)}. . . . .	91
C.5	(a) Temperature fluctuation at the outer thermal boundary layer displayed in a Hammer projection for case No.105, corresponding to the filled-in symbol in (b). (b) $Nu$ integration over the whole sphere and in region II on the outer sphere compensated by $R^{-3/2}$ and as a function of $R \equiv RaEk^{4/3}$ . . . . .	92

# List of Tables

2.1	Main input and out parameters and comparison with the results from [49]. All the simulations are run at $\eta = 0.6$ and $Pr = 1$ . . . . .	30
3.1	Different gravity profiles. $\lambda$ , $R_m$ and $\Delta R$ are parameters. . . . .	38
3.2	Parameters of the spherical RB simulations with $Pr = 1$ , which are compared to the results ( $Nu(\text{ref})$ and $Re_{rms}(\text{ref})$ ) of [49]. $N_{\theta,r,\varphi}$ indicates the number of grid points in the longitudinal, radial, and co-latitudinal direction, respectively. . . . .	40
3.3	Critical Rayleigh $Ra_c$ and effective critical Rayleigh $Ra_c^e$ for different gravity profiles. $Ra_c^e$ coincides for all the profiles except the parabolic. . . . .	42
3.4	$Ra_1$ , $Ra_2$ and effective value $Ra_1^e$ , $Ra_2^e$ for different gravity profiles. $Ra_{1,2}^e$ coincides for all the profiles except the parabolic. . . . .	45
3.5	Values of $Ra$ for the first occurrence of different states when $Pr = 7.1$ for quadratic gravity on the first line, and effective value on the second line. $Ra_{S_9}$ is equivalent to $Ra_c$ and $Ra_{S_8}$ is equivalent to $Ra_1$ . Confidence interval at $\pm 5\%$ for $Ra_c$ and $Ra_2$ , $\pm 10\%$ for the others. . . . .	51
4.1	Parameters of the spherical RB simulations with $Pr = 1$ , $Ra = 3 \times 10^4$ , $n_g = -2$ and $\eta = 0.6$ . $G(\theta, r, \varphi)$ is the gravity center location. $N_{\theta,r,\varphi} = (129, 49, 97)$ indicates the number of grid points in the longitudinal, radial, and co-latitudinal direction, respectively. The last five simulations are used to verify that the coefficients $C_{g,i}$ , see Eq. (B.6), are correctly implemented by putting the gravity center $G$ in five different locations with the same $L_{OG}$ , see figure 4.1. . . . .	56
4.2	Details of the simulations. The columns from left to right indicate: $Ra$ , the gravity profile exponent $n_g$ (see equation (4.6)), the number of grid points in the longitudinal, radial, and co-latitudinal direction $N_\theta \times N_r \times N_\phi$ , the shift of the gravity center with respect to the geometrical center $\varepsilon$ (see equation (4.1)), the average heat transfer across the inner and outer sphere (see equation (2.19)) $Nu$ , $\langle Nu_h(r) \rangle_r = \int_{r_i}^{r_o} Nu_h(r) dr$ (see equation (4.7)), and $Re_{rms}$ (see equation (4.8)). . . . .	58

C.1 Simulation details. We use the conduction state  $T(\theta, r, \varphi) = T_c(r)$  and  $\mathbf{u} = 0$  as the initial conditions for the simulations. Simulations of 1 – 94 are run at  $Pr = 1$ ,  $\eta = 0.6$  and  $g \sim (r_o/r)^{n_g}$  with  $n_g = 2$ . Simulations of 95 – 111 are run at  $Pr = 1$ ,  $\eta = 0.35$  and  $n_g = -1$ . The columns from left to right indicate: case number, Rayleigh number  $Ra$ , Rossby number  $Ro$ , the number of grid points in the longitudinal, radial, and co-latitudinal direction  $N_\theta \times N_r \times N_\varphi$ . A rotational symmetry order  $n_s$  is applied to reduce computational costs, indicating the longitude of the computational domain as  $2\pi/n_s$ . The average heat transfer  $Nu$  across the inner and the outer sphere, and the regional heat transfer across the outer sphere  $Nu_{I,II,III}$  (see figure 3(b) of the paper). Note that region II and III are only defined when a maximum prograde velocity is identified. 85

# CHAPTER 1

## Introduction

### 1.1 *Properties of fluids*

In everyday life any of us can experience, at least intuitively, the concept of fluids and flow. The air we breathe and the water we drink are fluids, and the flows of water in rivers and the sea are flows of our concern. Also the blood flow or the motion of air involved in heating and air conditioning systems. Moreover, the understanding of fluid behaviours and properties is of great importance in several fields ranging from meteorology to biomedical applications, from civil engineering to sportswear optimization, from microelectromechanical systems to renewable energy. Therefore, it is clear the crucial role of fluid dynamics in order to understand the behaviours which fluids exhibit. Indeed, in very general terms, fluid dynamics is the branch of science concerned with fluids in motion. In this chapter we will give a brief overview of the mathematical basics of fluid dynamics and the reasoning behind the application of these studies before introducing the content of the following chapter.

The fundamental property that defines fluids, being them liquids or gasses, is the absence of a defined shape and the easiness they can be deformed. On the other side, solids have a preferred shape. The separation line between solids and liquids, however, is not as clear as it seems: there exist substances, like paint, pitch and albumen, that exhibit properties typical of both states. Nevertheless, most common fluids (including water, air, and those analysed in this manuscript) can be easily catalogued using the typical definition.

When we consider their composition, we discover that fluids are made of an enormous number of particles in constant motion, with gasses having vast regions of emptiness between them. Studying the motion of each single particle is incredibly complex and does not bring any particularly useful information for a deeper understanding of the physics behind. Moreover, typical quantities studied in fluids, like velocity and mass distribution, can be highly non homogeneous and uniform when analysed at a molecular scale. Luckily, in order to understand the fluid dynamics we can focus on the average behaviour of the whole system. Indeed, we can introduce some quantities observable at a macroscopic level which are directly linked to the dynamic at a microscopic scale. For example the pressure, a macroscopic quantity, for a perfect gas is roughly defined as the

statistical average of the strength of the collisions between gas particles and the walls of the container. The microscopical structure of the matter can be neglected when the molecular density of the fluid is high enough and the region analysed is sufficiently big to explain these macroscopic effects: the fluid to all effects can be considered as a continuum distribution, where all the properties in each point of the fluid are defined as averages. This hypothesis, called continuum hypothesis, is valid when the mean free path of molecules (i.e. the average distance a molecule covers between collisions) is much shorter than the length scale of the system. This condition is usually well satisfied given that the typical mean free path of air in standard conditions is  $50\text{nm}$ , water being even lower. We will henceforth assume the hypothesis holds during our analysis of fluid behaviours.

## 1.2 Study of a flow field

The continuum hypothesis allows us to give a meaning to simple concepts like the local velocity of the fluid. We can now describe the entire flow field as an aggregate of these local velocities. There are two different approaches for this description, known as Eulerian and Lagrangian specifications. In the Eulerian specification the flow quantities are defined by two variables: the position in the space  $\mathbf{x}$  and the time  $t$ . Thus, we can then define a velocity vector  $\mathbf{u}(\mathbf{x}, t)$ , and we also note that for a steady fluid  $\mathbf{u}(\mathbf{x})$  does not depend on  $t$ . In the Lagrangian specification, on the other side, the focus is on the material element of the fluid and its evolution, defined by the position of its center of mass  $\mathbf{x}_c$  at the time  $t_0$ , and consequently the velocity vector is defined in terms of these variables as  $\mathbf{v}(\mathbf{x}_c, t)$ . There are situations for which the Lagrangian specification has advantages, but this is not the case for the problems analysed in the rest of this manuscript, so we will use the Eulerian specification. Using this specification, we can now define the acceleration of an element of the fluid as

$$\frac{\partial \mathbf{u}}{\partial t} + \mathbf{u} \cdot \nabla \mathbf{u}. \quad (1.1)$$

It is then convenient to add the operator of the material derivative

$$\frac{D}{Dt} = \frac{\partial}{\partial t} + \mathbf{u} \cdot \nabla \quad (1.2)$$

so that the acceleration becomes simply  $D\mathbf{u}/Dt$ . This operator can only be applied to variables function of  $\mathbf{x}$  and  $t$ .

## 1.3 Navier–Stokes equation

Without entering too much in the mathematical derivation, which can be found in [14, 90], we introduce now an equation that describes the motion of incompressible fluids: the famous Navier–Stokes equation

$$\begin{cases} \rho \frac{D\mathbf{u}}{Dt} = \rho \mathbf{F} - \nabla p + \mu \nabla^2 \mathbf{u} \\ \nabla \cdot \mathbf{u} = 0 \end{cases} \quad (1.3)$$

where  $\mu$  is the dynamic viscosity of the fluid,  $\rho$  the density,  $p$  the pressure and  $\mathbf{F}$  are body forces.

If we assume that the density of the fluid is uniform, we can introduce a new variable, the kinematic viscosity  $\nu = \mu/\rho$ . Under this assumption, in the equation of motion appears the term  $\nu \nabla^2 \mathbf{u}$  which shows that  $\nu$  has the role (and dimensions) of a diffusivity.

By noting that, when the flow velocity is zero, we have  $0 = \rho_s \mathbf{F} - \nabla p_s$ , where the subscript  $s$  indicates the hydro-static value, we can make an additional simplification: subtracting this value from equation (1.3) leads to

$$\rho \frac{D\mathbf{u}}{Dt} = \rho' \mathbf{F} - \nabla p' + \mu \nabla^2 \mathbf{u}, \quad (1.4)$$

where  $p' = p - p_s$  and  $\rho' = \rho - \rho_s$ , thus, if the density is constant,  $\rho' = 0$  and the effect of body forces disappear.

Until now, the equation contains dimensional quantities. It might be useful to consider the same equation written for dimensionless quantities. In order to do that, we apply the following transformations

$$\tilde{\mathbf{u}} = \frac{\mathbf{u}}{U}, \quad \tilde{\mathbf{x}} = \frac{\mathbf{x}}{L}, \quad \tilde{t} = \frac{tU}{L} \quad (1.5)$$

where  $L$  and  $U$  are some representative length and velocity of the system. To scale the pressure, we define  $\tilde{p} = \frac{p-p_0}{\rho U^2}$ , where  $p_0$  is a representative value for the pressure.

The dimensionless equation, in case of no body forces, can be written as

$$\frac{D\tilde{\mathbf{u}}}{D\tilde{t}} = -\nabla \tilde{p} + \frac{1}{Re} \nabla^2 \tilde{\mathbf{u}}, \quad \nabla \cdot \tilde{\mathbf{u}} = 0 \quad (1.6)$$

where the spatial derivatives are with respect to  $\tilde{x}$ . The parameter  $Re = \frac{LU}{\nu}$  is called Reynolds number and, being the only parameter that appears in equation (1.6), is responsible of all the changes in the dynamics of the system. When different terms appear in equation (1.3), it may be useful to introduce additional dimensionless parameters: they will be added when needed in the following sections.

## 1.4 Thermal convection

There are a number of physical situations for which density variation can not be neglected. When the variation is the driver of the flow, we speak of natural convection. One of the most typical representation of natural convection is thermally driven flows. We have the so called Rayleigh–Bénard convection

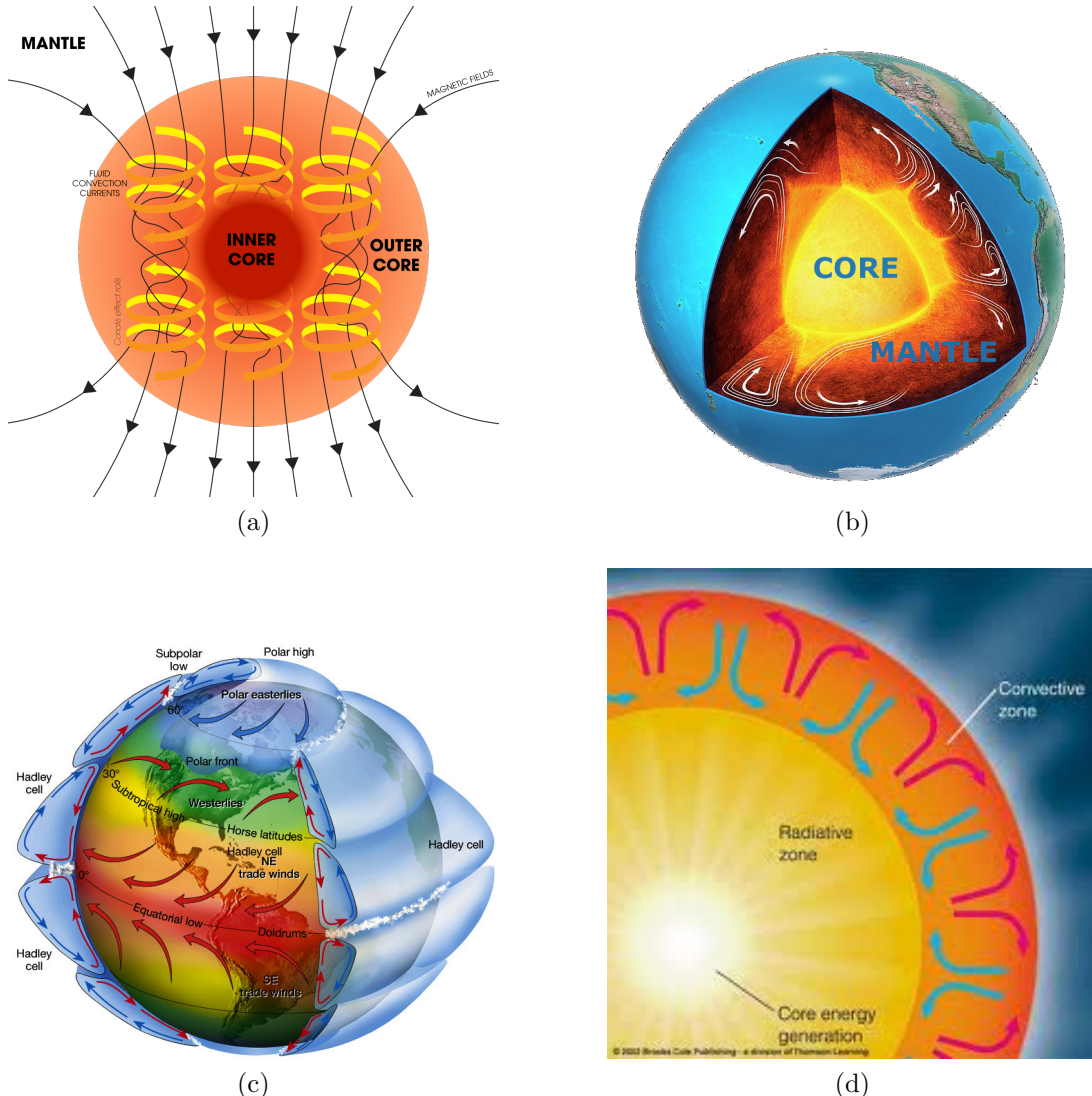


Figure 1.1: Examples of thermal convection in nature. (a) Outer core convection, primary candidate for the dynamo effect related to Earth’s magnetic field. (b) Convection in the mantle, responsible of tectonic plates motion. (c) Convection cells in the atmosphere. (d) Convection in the interior of the Sun. Images from the web, links are provided by clicking the corresponding alphabets.

when a system subjected to gravity is heated from below and cooled from above. Rayleigh–Bénard convection is omnipresent in nature, and fundamental in many aspects of life. In figure 1.1 we show some of the examples of the occurrence of this phenomenon in nature. Convection in the interior of Earth happens in the mantle and in the liquid outer core. In figure 1.1a the core is shown: it is strongly believed that the motion of liquid metal in the outer core, when coupled with the rotation of Earth (basic assumptions for the dynamo effect theory), plays a fundamental role in the genesis of Earth’s magnetic field, which protects the planet from the danger of solar winds [66, 104, 119]. To better

analyse this phenomenon, simulations were performed in spherical shells by [55, 56, 93, 151]. Convection in the mantle, shown in figure 1.1b, is instead considered responsible of tectonic plate motions and volcano activity [62, 170, 150, 70, 36]. Convection is also critical in the atmosphere (figure 1.1c): cold air sinks close to the poles and warm air rises around the equator, generating a circulation pattern called Hadley cell, which breaks into three smaller cells in each hemisphere [63]. Oceanic currents are a clear product of convection as well. Moving further away from Earth, we see that convection plays a role also in other planets and stars. Figure 1.1d shows the convective zone of the sun, which has an impact in the generation of internal gravity waves [39]. Furthermore, convection is often used in industrial applications such as cooling of electrical devices and nuclear reactors [71, 167, 168].

#### 1.4.1 Model of convection: Boussinesq approximation

To study this phenomenon it is crucial to proper model the problem. First we identify the physical logic behind the convection: fluid closer to the lower plane is hotter and less dense than the upper - colder - fluid, so a circulating flow appears with the denser fluid falling and the hotter fluid rising. For an ideal fluid this instability-driven flow happens immediately. However, when viscosity and thermal conduction are taken into consideration, the onset of convection happens only when a dimensionless parameter called Rayleigh number  $Ra$ , reaches a critical value.  $Ra$  is defined as

$$Ra = \frac{g_0 \alpha \Delta T d^3}{\nu \kappa} \quad (1.7)$$

where  $\alpha$  is the coefficient of thermal expansion,  $\kappa$  the thermal diffusivity,  $\Delta T$  the difference of temperature between the two planes and  $d$  the dept of the layer, and represents the ratio between the destabilizing effect of buoyancy over the stabilizing effect of viscosity.

The evolution of a fluid subjected to Rayleigh-Bénard convection can be characterized by three main states: when the Rayleigh number is lower than the critical value, the dynamic is conductive and no circulating flow appears. If  $Ra$  is increased, for example by increasing the temperature difference between the planes, we can observe the onset of convection: the fluid starts exhibiting a stable recirculating flow. Increasing the Rayleigh number even further brings additional instability in the system and leads to the rise of a turbulent and chaotic dynamic where, usually, no clear pattern can be recognised.

Boussinesq, in 1903, suggested an approximation that models with great accuracy systems under Rayleigh-Bénard convection: the density variation has an effect only in front of  $\mathbf{F} = \mathbf{g}$ , while we can consider constant the other factors<sup>1</sup>. This allows us to keep the incompressible form  $\nabla \cdot \mathbf{u} \approx 0$ . Equation (1.4) is

---

<sup>1</sup>notably, this approximation is not true for water close to the freezing point, since density varies nonlinearly with temperature

normalised by the static density  $\rho_s$

$$\frac{\rho}{\rho_s} \frac{D\mathbf{u}}{Dt} = \frac{\rho'}{\rho_s} \mathbf{g} - \frac{1}{\rho_s} \nabla p' + \frac{\mu}{\rho_s} \nabla^2 \mathbf{u} \quad (1.8)$$

and our approximation allows us to replace  $\rho/\rho_s \approx 1$  and  $\mu/\rho_s \approx \nu$  to obtain

$$\frac{D\mathbf{u}}{Dt} = \frac{\rho'}{\rho_s} \mathbf{g} - \frac{1}{\rho_s} \nabla p' + \nu \nabla^2 \mathbf{u}. \quad (1.9)$$

Then we need to consider the conservation of energy in the system. As before, we leave the mathematical derivation aside and provide the equation for the energy conservation under the Boussinesq approximation:

$$\frac{DT}{Dt} = \kappa \nabla^2 T. \quad (1.10)$$

By defining  $T = \Delta T \tilde{T}$  and  $\mathbf{g} = g \tilde{\mathbf{g}}$  and introducing another dimensional parameter, the Prandtl number  $Pr = \nu/\kappa$ , we can write the dimensionless equations for a fluid under the Boussinesq approximation:

$$\left\{ \begin{array}{l} \frac{D\tilde{\mathbf{u}}}{Dt} = -\nabla \tilde{p} + \tilde{T} \tilde{\mathbf{g}}(r) + \sqrt{\frac{Pr}{Ra}} \nabla^2 \tilde{\mathbf{u}} \\ \nabla \cdot \tilde{\mathbf{u}} = 0 \\ \frac{D\tilde{T}}{Dt} = \frac{1}{\sqrt{Ra} Pr} \nabla^2 \tilde{T}. \end{array} \right. \quad (1.11)$$

Finally, the response of the system to temperature differences (in terms of the ratio between convective and conductive heat transfers) can be measured with the dimensionless Nusselt number  $Nu = \frac{Qd}{k\Delta T}$ , where  $Q$  is the heat flux and  $k$  the thermal conductivity.

## 1.5 Computational Fluid Dynamics

The study of the evolution of fluids is often impossible to perform analytically. By using computational power and conservation laws governing fluid motion, it is possible to have a quantitative prediction of it.

Several types of numerical methods have been developed to simulate fluid flows, e.g. finite difference, finite-element, finite-volume, and spectral methods.

The accuracy of these methods has increased remarkably during the last decades, but the predictions are never completely exact. Discretization errors are intrinsic of all numerical methods and are related to the approximation of a continuum system to a discrete one. In the case of finite difference, a finite number of discrete grid points is used, and even the evolution of time is discretized. However, computational fluid mechanics (CFD) has several advantages:

- It is rather quick to produce results, and the cost of computational time and power has decreased in these years

- A lot of information can be extracted from a single simulation, which provides values for all the relevant variables
- Changing parameters or conditions can be done easily, and parameter spaces unreachable by experiments are easier to analyse, for example ideal conditions where some terms are switched off, or realistic conditions for which no practical experiment can be conducted.

### 1.5.1 Fractional time step discretization

The time evolution which the numerical scheme used for the analyses of this manuscript is based a fractional time discretization which leads to an error of order  $\Delta t^2$  [158, 157] and it is briefly summarised here.

We assume that the time integration scheme advances from  $t^n$  to  $t^{n+1}$  via  $L$  substeps of uneven size  $\tau(l)\Delta t$  for  $l \in [1, L]$  such that  $\sum_l \tau(l) = 1$ . The evolution of a dimensionless incompressible viscous flow, described by equation (1.6), can now be discretised in time as

$$\frac{\mathbf{u}^{l+1} - \mathbf{u}^l}{\tau(l)\Delta t} + [\gamma \nabla \cdot (\mathbf{u}\mathbf{u})^l + \rho \nabla \cdot (\mathbf{u}\mathbf{u})^{l-1}] = -\nabla p^{l+1} + \frac{1}{2Re} \nabla^2(\mathbf{u}^{l+1} + \mathbf{u}^l) \quad (1.12)$$

where  $\gamma$  and  $\rho$  are coefficients and clearly  $\mathbf{u}^0 \equiv \mathbf{u}^n, \mathbf{u}^L \equiv \mathbf{u}^{n+1}$ . The convective terms are evaluated explicitly in time using a forward extrapolation:

$$NL(\mathbf{u})^{l+1/2} = [\gamma \nabla \cdot (\mathbf{u}\mathbf{u})^l + \rho \nabla \cdot (\mathbf{u}\mathbf{u})^{l-1}] \quad (1.13)$$

while the viscous terms are implicitly computed with a Crank-Nicolson scheme

$$\mathbf{u}^{l+1/2} = \frac{\mathbf{u}^{l+1} + \mathbf{u}^l}{2}. \quad (1.14)$$

The continuity equations reads  $\nabla \cdot \mathbf{u}^{l+1/2} = 0$ , and to enforce the solenoidal velocity we must act on  $p^{l+1}$ .

Before enforcing the incompressibility, we compute a provisional (non solenoidal) field  $\tilde{\mathbf{u}}$ :

$$\frac{\tilde{\mathbf{u}} - \mathbf{u}^l}{\tau(l)\Delta t} + [\gamma \nabla \cdot (\mathbf{u}\mathbf{u})^l + \rho \nabla \cdot (\mathbf{u}\mathbf{u})^{l-1}] = -\nabla p^l + \frac{1}{2Re} \nabla^2(\tilde{\mathbf{u}} + \mathbf{u}^l) \quad (1.15)$$

and subtracting this equation from equation (1.12) we obtain

$$\frac{\mathbf{u}^{l+1} - \tilde{\mathbf{u}}}{\tau(l)\Delta t} = -\nabla p^{l+1} + \nabla p^l + \frac{1}{2Re} \nabla^2(\mathbf{u}^{l+1} - \tilde{\mathbf{u}}). \quad (1.16)$$

The non solenoidal field differs from  $\mathbf{u}^{l+1}$  because the gradient of the pressure is incorrectly evaluated, so we can enforce the correction with the gradient of a scalar  $\Phi$ :

$$\mathbf{u}^{l+1} = \tilde{\mathbf{u}} - \tau(l)\Delta t \nabla \Phi \quad (1.17)$$

such that

$$\nabla^2 \Phi = \frac{1}{\tau(l)\Delta t} \nabla \cdot \tilde{\mathbf{u}}. \quad (1.18)$$

The new velocity  $\mathbf{u}^{l+1}$  is then obtained inserting the solution of this elliptic equation into equation (1.17). To compute the new pressure, we substitute  $u^{l+1} - \tilde{\mathbf{u}} = \tau(l)\Delta t \nabla \Phi$  into equation (1.16) to obtain

$$p^{l+1} = p^l + \Phi - \frac{\tau(l)\Delta t}{2Re} \nabla^2 \Phi \quad (1.19)$$

defined up to a constant that can be chosen by fixing the pressure at one point in the field.

## 1.6 Thesis overview

In the following chapters we will analyse in more detail the problem of Rayleigh–Bénard convection in spherical shells under different circumstances. Each of them is taken from already published articles or works currently under the process of being published. We decided to remain as faithful as possible to the original content: this means that each chapter is a standalone and can be read independently, but it may cause the repetition of a few concepts.

In chapter 2, based on [124], we will present a numerical scheme developed to deal with the singularities related to spherical systems. Despite the existence of other approaches, e.g. spherical harmonic methods, our finite difference scheme has many customization options: it is able to perform simulations involving both the singularities at the polar axis and at the center, it offers great flexibility in the choice of boundary conditions, and allows for non-uniform grid refinements in two of the three spherical directions. The scheme was thoughtfully tested and compared with literature, verifying accuracy and stability under different conditions. A parallelization of the code has been then implemented, allowing for an extremely competitive simulation time.

The last part of the thesis is dedicated to reporting some of the applications of the scheme to open problems in physics. We start from chapter 3 (presented in [126]) with the characterization of the evolution of a fluid confined between spherical shells and subjected to radial gravity (and thus experiencing Rayleigh–Bénard convection). The primary focus is the determination of the onset of convection in such a system, followed by an analysis on the typical structures that arise as the Rayleigh number increases. Both air and water are studied: the difference between them is represented by a variation in the Prandtl number. The use of different fluids is expected to have an impact primarily in the viscous term, thus allowing for a decoupling of the various effects the system has experienced. Also the effect of different gravity profiles is taken into account. The analysed profiles are: inverse quadratic, that simulates the effect of gravity in the atmosphere; linear, that can be used as a model of the interior of a celestial body; a mixed profile, that is a more accurate representation of the difference in densities inside the Earth (between core and mantle); an artificial

parabolic profile; and a constant profile used as a reference. The behaviour of the system under this plethora of different conditions is thoughtfully analysed and reported. Another important parameter used to explore the configuration space is the Rayleigh number. The system has been studied under constant, increasing and decreasing  $Ra$ , and difference and similitude in the behaviour are reported. The various configuration of convective plumes and the existence of initial condition dependence (hysteresis phenomena) are discussed as well.

This study then leads to the analysis realised in chapter 4, based on [160]. This study is inspired by the knowledge that the inner core of Earth is reported to feature hemispherical asymmetries in density and non uniformity in the heat flux between the core and the mantle. Current studies connect this dishomogeneity to the amplification factor induced by the crystallization of the denser hemisphere and the melting of the other, leading to a shift in the gravity center toward the crystallizing side. We built a simplified model which may give insight about qualitative and quantitative flow properties by considering turbulent Rayleigh–Bénard convection between spherical shells and with an offset of the gravity center with respect to the spheres center. The investigation is done considering a generic gas between the shells, which have an aspect ratio similar to Earth’s outer core. The generation of convective jets is analysed, alongside the large-scale circulation and the heat transfer rate. The space of parameters studied includes different values of Rayleigh number and different gravity profiles.

In chapter 5, based on [159], another thermally driven flow structured is considered. Here, using the same structure of a fluid between spherical shells with radial gravity, we introduce rotation in the system. The rotational effects of the liquid core of Earth are said to be relevant for the magnetic field of our planet, as well as oceanic currents and in Sun interior structure. The study focuses on the diffusion-free scaling regime for fluids between spherical shells. This regime has already been studied for planar structures and it is characterized by unbroken vertical vortices, but a complete comparison with the spherical geometry was missing. The objective of this work is to analyse the appearance of diffusion-free scaling for slowly rotating spherical systems, which does not occur in planar geometry. The different regions that forms in the spherical model are studied to highlight whether the flow is following a standard convective pattern or if other effects dominate the evolution.

Finally, in the last chapter, we provide a conclusive overview of the researches carried out, with a focus on the results found and some suggestions for possible future works that, starting from the current ones, may sparkle interest and lead to new results.



## CHAPTER 2

# A finite-difference scheme for three-dimensional incompressible flows in spherical coordinates\*

### 2.1 *Introduction*

Thanks to the growing availability of computational power also the complexity of flows tackled by numerical simulations is increasing. Among many, one of the challenges of a computation is the mathematical description of non trivial domains and the flows developing within spherical geometries belong to this category.

Indeed, the mapping of spherical to Cartesian coordinates reads

$$x = r \cos \theta \sin \phi, \quad y = r \sin \theta \sin \phi, \quad z = r \cos \phi,$$

(Fig. 2.1) and it is not single valued at the centre ( $r = 0$ ) and on the polar axis ( $\phi = 0, \pi$ ) therefore, even if the sphere is among the simplest shapes, its natural coordinate system contains mathematical singularities that are reflected also in the governing equations for fluid flows (see next section).

Spherical domains have been traditionally used in geophysics [120], oceanography [34], meteorology [116], astrophysics [4], [54] and magnetohydrodynamics [87] although they are gaining popularity also for industrial [113] and fundamental problems [21], [81], [132].

In fact, an important advantage of the spherical coordinates is that their highest degree of symmetry imposes no preferred orientation and this is a desired property when the system evolves in an unbounded space [18]. That the mesh topology could interfere with the flow dynamics was shown by [158] who computed the evolution of an azimuthally unstable toroidal vortex ring on a Cartesian square mesh and obtained preferentially the  $n = 4$  wavenumber even if the linear stability analysis predicted the  $n = 5$  mode. On the other hand, the same phenomenon, simulated using a polar cylindrical mesh [112], correctly

---

\*Based on L. Santelli, P. Orlandi, R. Verzicco, *A finite-difference scheme for three-dimensional incompressible flows in spherical coordinates*, J. Comput. Phys., (2020), p. 109848.

showed the emergence of fivefold symmetric structures as expected from the theory [135].

Since the early stability analyses of thermal convection in spherical shells [21], also in later studies [54], [44], [88], [154] the variables were expressed by spherical harmonics for the longitude  $\theta$  and colatitude  $\phi$  while Chebyshev polynomials were mostly used for the radial direction  $r$  (Fig. 2.1). This expansion allowed the development of accurate pseudo-spectral methods that avoided the equation singularity at the polar axis.

All these studies, however, did not cope with the singularity at the sphere centre ( $r = 0$ ) since the equations were solved only in the gap between two concentric spheres.

On the other hand, [79] developed a spectral method that could discretize the equations up to the sphere centre by using only the even order Chebyshev polynomials for the radial direction that avoided the unnecessary mesh refinement near the origin. Also [82] simulated the whole sphere although they used Jacobi polynomials that, in addition to the previous property, satisfy also the regularity conditions at the poles. Using this numerical scheme [83] were able to simulate magnetohydrodynamic processes in a precessing sphere. [12] developed a Navier-Stokes spectral solver in a sphere employing a latitude dependent number of modes that avoided the difficulties with the sphere centre and polar axis.

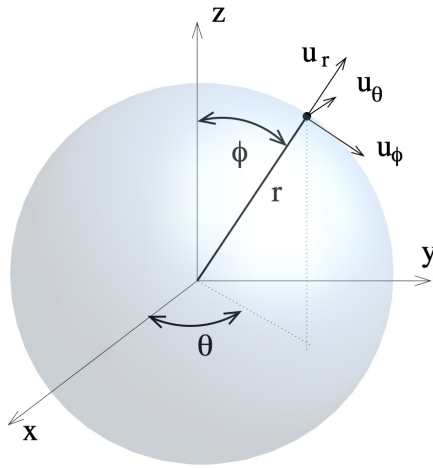


Figure 2.1: Sketch of the system and coordinate definition.

Spectral methods are generally preferred to other approaches since, although the overall accuracy depends also on the dealiasing schemes, they yield smaller numerical errors for a given number of nodes (modes). However, as shown by [106], finite-difference approximations, if properly implemented, become very competitive cost-wise with respect to spectral methods even considering that the former require more computational nodes to achieve the same precision. In addition, if the simulation has to cope with complex boundary conditions, variable fluid properties or generic node distributions then finite-differences are the best option.

Despite these advantages, the literature on finite-difference methods for the solution of the Navier–Stokes equations in spherical coordinates is scarce and, to the knowledge of the authors only few studies are available. [162] presented a method for solving the equations in a spherical shell by finite-difference approximations on a staggered mesh in all three directions; the variables were modified at the poles by semi-analytic corrections to avoid stability issues. [51] solved the linear Boussinesq convection in a spherical shell using Fourier modes along the latitude  $\theta$  and finite-differences in  $r$  and  $\phi$ . The model was completed with the nonlinear convective terms in [52] and, in both cases, in order to avoid the stability limitations at the polar axis, a low-pass filtering of the solution was applied around the poles. Apparently, this smoothing strategy was widely adopted in the atmospheric community and [35] described it in a systematic way.

[80] relied on finite-difference approximations in all three directions for the simulation of convection in a rotating spherical shell and, also in this case, a low-pass filter near the poles was employed.

[8] used the code PARODY to simulate convection-driven numerical dynamos in a spherical shell; in this case second-order finite differences were used only for the radial directions while spherical harmonics were adopted for the lateral ones. The scheme was very similar to that of [54] although the new radial discretization made the code suitable for parallel computation on distributed memory clusters.

In the paper [133], second-order finite-differences are employed to solve the Navier–Stokes equations in spherical coordinates relying only on the semi-conservative form of the equations and on the discretization on a staggered–mesh to remove the singularities. However, only flows within two spherical shells are considered, thus never coping with the singularity at  $r=0$ . In addition, all their examples had vanishing meridional velocity at the poles therefore the singularities of the equations were not really tackled.

[105] proposed a clever procedure to avoid the polar singularity (both, cylindrical and spherical) by extending the radial coordinate to negative values and discretizing the domain so that no nodes are located at  $r = 0$ . They consider the compressible Navier–Stokes equations and use a co-located discretization with high order finite-differences for the radial direction and spectral methods in the remaining ones. The application of the same method to a fully staggered discretization for the incompressible Navier–Stokes equations is not obvious and it would presumably require substantial changes.

The study by [19] uses a finite-volume method to solve the Navier–Stokes equations in spherical coordinates. In this case, however, neither the singularity at the centre nor at the polar axis is encountered since the domain of interest is restricted to a spherical sector in which the self-similar region of a round jet is computed.

In this chapter we present a novel numerical method for the solution of the incompressible Navier–Stokes equations in spherical coordinates. It is based on second-order finite-difference approximations on a staggered mesh that, combined with a change of variables and a special treatment of some discretized terms, eliminates the singularities at the polar axis and at the sphere centre, simultaneously. The same method can be applied both to flows developing in a

spherical shell and in the whole sphere up to  $r = 0$  without any change in the numerical procedure.

The time step restrictions introduced by the discretization around the polar axis and sphere centre are attenuated for the former region while the latter still gives strong time step limitations, although only in very unfavourable cases with the largest flow velocity occurring at  $r = 0$ .

We show that the method maintains the second-order accuracy and yields free-divergence velocity fields to machine precision even when using computational meshes that are unnecessarily refined at the polar axis and sphere centre.

The method is verified and validated by computing numerical examples that stress the treatment of the equations at the singular points and by comparing the results with analogous computations available from the literature.

Finally, since the proposed method takes after the scheme of [158] it shares the same variable arrangement and memory layout, therefore it is efficiently and massively parallelized as done in [144].

The chapter is organized as follows: in the next section we present the equations and the change of variables adopted to remove the singularity. In section 2.3 we discuss the discretization of the variables and the technicalities needed for some terms while in section 2.4 we briefly describe the numerical method. In section 2.5 a number of numerical examples is shown and discussed to assess the reliability and efficiency of the method. Finally in section 2.6 the closing remarks and perspectives for future work are given.

## 2.2 Equations

The continuity and momentum equations for an incompressible and viscous flow, in non dimensional form and in spherical coordinates, read [14]:

$$\begin{aligned}
& \frac{1}{r^2} \frac{\partial r^2 u_r}{\partial r} + \frac{1}{r \sin \phi} \frac{\partial u_\theta}{\partial \theta} + \frac{1}{r \sin \phi} \frac{\partial \sin \phi u_\phi}{\partial \phi} = 0, \quad (2.1) \\
& \frac{\partial u_r}{\partial t} + \mathbf{u} \cdot \nabla u_r - \frac{u_\phi^2}{r} - \frac{u_\theta^2}{r} = -\frac{\partial p}{\partial r} + f_r + \\
& \frac{1}{Re} \left( \nabla^2 u_r - \frac{2u_r}{r^2} - \frac{2}{r^2 \sin \phi} \frac{\partial u_\phi \sin \phi}{\partial \phi} - \frac{2}{r^2 \sin^2 \phi} \frac{\partial u_\theta}{\partial \theta} \right), \\
& \frac{\partial u_\theta}{\partial t} + \mathbf{u} \cdot \nabla u_\theta + \frac{u_\theta u_r}{r} + \frac{u_\theta u_\phi}{r \tan \phi} = -\frac{1}{r \sin \phi} \frac{\partial p}{\partial \theta} + f_\theta \\
& + \frac{1}{Re} \left( \nabla^2 u_\theta + \frac{2}{r^2 \sin^2 \phi} \frac{\partial u_r}{\partial \theta} + \frac{2 \cos \phi}{r^2 \sin^2 \phi} \frac{\partial u_\phi}{\partial \theta} - \frac{u_\theta}{r^2 \sin^2 \phi} \right), \\
& \frac{\partial u_\phi}{\partial t} + \mathbf{u} \cdot \nabla u_\phi + \frac{u_\phi u_r}{r} - \frac{u_\theta^2}{r \tan \phi} = -\frac{1}{r} \frac{\partial p}{\partial \phi} + f_\phi \\
& + \frac{1}{Re} \left( \nabla^2 u_\phi + \frac{2}{r^2} \frac{\partial u_r}{\partial \phi} - \frac{u_\phi}{r^2 \sin^2 \phi} - \frac{2 \cos \phi}{r^2 \sin^2 \phi} \frac{\partial u_\theta}{\partial \theta} \right), \quad (2.2)
\end{aligned}$$

where  $u_\theta$ ,  $u_r$  and  $u_\phi$  are the velocity components in the longitudinal, radial and colatitude directions, respectively,  $p$  the pressure and  $f_\theta$ ,  $f_r$  and  $f_\phi$  forcings that could be used for volume forcings such as Coriolis accelerations.  $Re = UL/\nu$  is the Reynolds number defined by appropriate velocity  $U$  and length  $L$  scales and  $\nu$  is the kinematic viscosity of the fluid.

In the above equations the following relations are used:

$$\mathbf{u} \cdot \nabla q \equiv u_r \frac{\partial q}{\partial r} + \frac{u_\theta}{r \sin \phi} \frac{\partial q}{\partial \theta} + \frac{u_\phi}{r} \frac{\partial q}{\partial \phi}$$

and

$$\nabla^2 q \equiv \frac{1}{r^2} \frac{\partial}{\partial r} r^2 \frac{\partial q}{\partial r} + \frac{1}{r^2 \sin \phi} \frac{\partial}{\partial \phi} \sin \phi \frac{\partial q}{\partial \phi} + \frac{1}{r^2 \sin^2 \phi} \frac{\partial^2 q}{\partial \theta^2}.$$

As anticipated in the Introduction, many terms of Equations (2.1–2.2) become singular at the origin ( $r = 0$ ) and at the North and South poles, respectively,  $\phi = 0$  and  $\phi = \pi$  (hereinafter referred to as ‘polar axis’) and this is not due to the physics described by the equations but to the spherical coordinate transformation that is not single valued at those points. Another drawback is that the coordinates  $r = 0$  and  $\phi = 0, \pi$  do not coincide with physical boundaries, such as a solid wall or a slip surface, therefore boundary conditions for the unknowns can not be easily computed there. The same argument does not apply to the longitudes  $\theta = 0, 2\pi$  that, being the same physical point, can benefit from periodic boundary conditions that do not need explicit values for the unknowns.

Following [158] and motivated by the above arguments, we introduce a new set of unknowns  $\mathbf{q} = (q_\theta, q_r, q_\phi) = (u_\theta, u_r r^2, u_\phi \sin \phi)$  that, according to Equation (2.1), can also be thought of as volume fluxes. An immediate advantage is that these variables yield  $q_r(\theta, 0, \phi) = q_\phi(\theta, r, 0) = q_\phi(\theta, r, \pi) \equiv 0$  therefore transforming the difficult singular points for  $\mathbf{u}$  in trivial boundary conditions for  $\mathbf{q}$ .

By proper manipulation of Equations (2.1–2.2) they can be easily rewritten in terms of the new variables  $\mathbf{q}$ :

$$\sin \phi \frac{\partial q_r}{\partial r} + r \frac{\partial q_\theta}{\partial \theta} + r \frac{\partial q_\phi}{\partial \phi} = 0, \quad (2.3)$$

$$\begin{aligned} \frac{\partial q_\theta}{\partial t} + \frac{1}{r^2} \frac{\partial q_r q_\theta}{\partial r} + \frac{1}{r \sin \phi} \frac{\partial q_\theta^2}{\partial \theta} + \frac{1}{r \sin \phi} \frac{\partial q_\theta q_\phi}{\partial \phi} + \frac{q_\theta q_r}{r^3} + \frac{q_\theta q_\phi}{r \tan \phi \sin \phi} &= -\frac{1}{r \sin \phi} \frac{\partial p}{\partial \theta} + f_\theta \\ + \frac{1}{Re} \left( \frac{1}{r^2} \frac{\partial}{\partial r} r^2 \frac{\partial q_\theta}{\partial r} + \frac{1}{r^2 \sin \phi} \frac{\partial}{\partial \phi} \sin \phi \frac{\partial q_\theta}{\partial \phi} + \frac{1}{r^2 \sin^2 \phi} \frac{\partial^2 q_\theta}{\partial \theta^2} \right. \\ \left. + \frac{2}{r^4 \sin \phi} \frac{\partial q_r}{\partial \theta} + \frac{2 \cos \phi}{r^2 \sin^3 \phi} \frac{\partial q_\phi}{\partial \theta} - \frac{q_\theta}{r^2 \sin^2 \phi} \right), \end{aligned} \quad (2.4)$$

$$\frac{\partial q_r}{\partial t} + \frac{\partial}{\partial r} \left( q_r \frac{q_r}{r^2} \right) + \frac{1}{r \sin \phi} \frac{\partial q_r q_\theta}{\partial \theta} + \frac{1}{r \sin \phi} \frac{\partial q_r q_\phi}{\partial \phi} - \frac{r q_\phi^2}{\sin^2 \phi} - r q_\theta^2 = -r^2 \frac{\partial p}{\partial r} + r^2 f_r$$

$$\frac{1}{Re} \left( \frac{\partial}{\partial r} r^2 \frac{\partial q_r / r^2}{\partial r} + \frac{1}{r^2 \sin \phi} \frac{\partial}{\partial \phi} \sin \phi \frac{\partial q_r}{\partial \phi} + \frac{1}{r^2 \sin^2 \phi} \frac{\partial^2 q_r}{\partial \theta^2} - \frac{2q_r}{r^2} - \frac{2}{\sin \phi} \frac{\partial q_\phi}{\partial \phi} - \frac{2}{\sin \phi} \frac{\partial q_\theta}{\partial \theta} \right), \quad (2.5)$$

$$\begin{aligned} \frac{\partial q_\phi}{\partial t} + \frac{1}{r^2} \frac{\partial q_r q_\phi}{\partial r} + \frac{1}{r \sin \phi} \frac{\partial q_\theta q_\phi}{\partial \theta} + \frac{1}{r} \frac{\partial}{\partial \phi} \left( q_\phi \frac{q_\phi}{\sin \phi} \right) + \frac{q_\phi q_r}{r^3} - \frac{q_\theta^2 \cos \phi}{r} = - \frac{\sin \phi}{r} \frac{\partial p}{\partial \phi} + \sin \phi f_\phi \\ + \frac{1}{Re} \left( \frac{1}{r^2} \frac{\partial}{\partial r} r^2 \frac{\partial q_\phi}{\partial r} + \frac{1}{r^2} \frac{\partial}{\partial \phi} \sin \phi \frac{\partial q_\phi / \sin \phi}{\partial \phi} + \frac{1}{r^2 \sin^2 \phi} \frac{\partial^2 q_\phi}{\partial \theta^2} \right. \\ \left. + \frac{2 \sin \phi}{r^2} \frac{\partial q_r / r^2}{\partial \phi} - \frac{q_\phi}{r^2 \sin^2 \phi} - \frac{2 \cos \phi}{r^2 \sin \phi} \frac{\partial q_\theta}{\partial \theta} \right), \end{aligned} \quad (2.6)$$

that now can be discretized on a computational grid.

It is worthwhile noticing that the above equations, once discretized on a staggered-mesh, are equivalent to those for the contravariant velocity components (multiplied by the cell volume) in general curvilinear coordinates as shown in [121]. However, the equations in general curvilinear coordinates entail several metric terms that add to the operation count and to the storage requirement, leaving aside the augmented data-transfer across nodes in parallel computing. On the other hand, in spherical coordinates the metric terms reduce to a one-dimensional vector for the radial direction and a two-dimensional array (obtained by the product of two one-dimensional vectors) for the azimuthal direction [14] thus largely reducing the mentioned drawbacks.

## 2.3 Variable discretization

Equations (2.3, 2.4–2.6) are discretized by central second-order accurate finite-difference approximations along the same line as [158]. Here we describe the technicalities needed for the calculation of some representative terms.

We refer to the sketch of Fig. 2.2 where the staggered arrangement of [64] is adopted and the node indices  $1 \leq i \leq N_i$ ,  $1 \leq j \leq N_j$ ,  $1 \leq k \leq N_k$  span the  $0 \leq \theta \leq 2\pi$ ,  $0 \leq r \leq R$  and  $0 \leq \phi \leq \pi$  coordinates, respectively.

Let the nodes **A** and **B** have, respectively,  $i, j, k$  and  $i+1, j+1, k+1$  indices then  $q_r(i, j, k)$  is located at the position  $(\theta_{i+1/2}, r_j, \phi_{k+1/2})$  which is the centre of the  $r$ -normal face of the cell. Similarly  $q_\theta(i, j, k)$  is at  $(\theta_i, r_{j+1/2}, \phi_{k+1/2})$ ,  $q_\phi(i, j, k)$  at  $(\theta_{i+1/2}, r_{j+1/2}, \phi_k)$  and the pressure at the cell centre  $(\theta_{i+1/2}, r_{j+1/2}, \phi_{k+1/2})$ . This implies that only the variable  $q_r$  has  $N_j$  values in the radial direction while it has  $N_i - 1$  and  $N_k - 1$  values in the longitude and colatitude directions, respectively. Similar considerations apply to the other velocity components.

Within the staggered discretization only  $q_r$  is located at the sphere origin  $r_1 = 0$  (Fig. 2.2a) where, however, Equation (2.5) does not need to be solved because  $q_r(i, 1, k) \equiv 0$  is a boundary condition.

The same argument applies to Equation (2.6) in which, for  $\phi = 0$  and  $\phi = \pi$ , it results  $q_\phi \equiv 0$ .

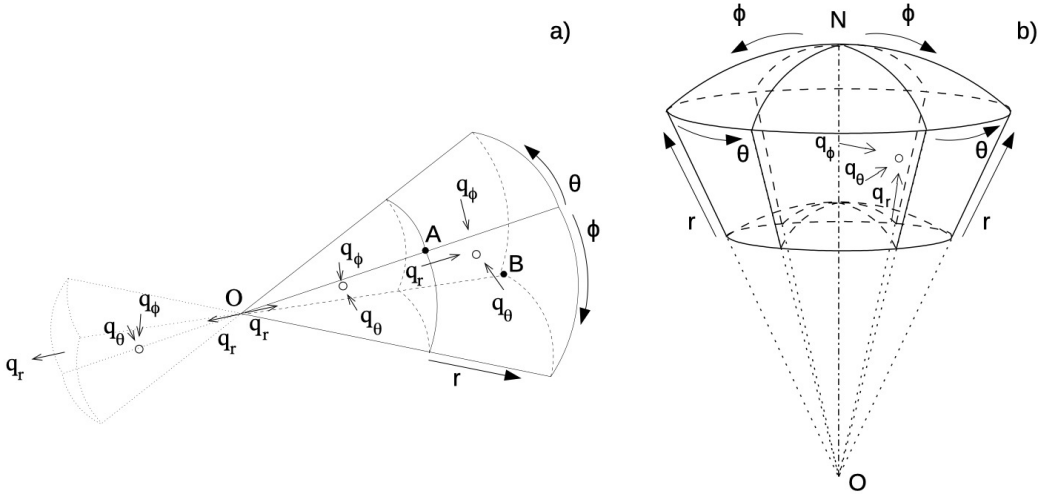


Figure 2.2: a) Staggered arrangement of the discrete variables and cells next to the sphere centre. b) Cells near the North pole of the sphere.

The variable change combined with the staggered discretization allows the straightforward computation of *almost* all terms of Equations (2.3, 2.4–2.6) without coping with the singularities. As an example, we take the term  $(1/r^2)\partial(q_r q_\phi)/\partial r$  of the  $q_\phi$  equation for which, because of the staggering, the first radial node is at  $j = 3/2$ . Evidencing by bold face the indices in the differentiated direction we obtain:

$$\frac{1}{r^2} \frac{\partial q_r q_\phi}{\partial r} \Big|_{i+\frac{1}{2}, \frac{3}{2}, k} \approx \frac{(q_r q_\phi)_{i+\frac{1}{2}, 2, k} - (q_r q_\phi)_{i+\frac{1}{2}, 1, k}}{r_{\frac{3}{2}}^2 (r_2 - r_1)}. \quad (2.5)$$

While we have omitted all the averages needed to locate the unknowns at the appropriate positions for the differentiation, (e.g.  $(q_r q_\phi)_{i+1/2, 2, k} = [q_r(i, 2, k+1) + q_r(i, 2, k)][q_\phi(i, 3, k) + q_\phi(i, 2, k)]/4$ ) we note that all the quantities are perfectly defined ( $r_{3/2} = \Delta r_1/2$  and  $(q_r)_{i+1/2, 1, k} = 0$ ) and the derivative can be computed without any problem.

Along the same line, the term  $1/(r \sin \phi)\partial(q_\theta q_\phi)/\partial \phi$  of the  $q_\theta$  equation computed at the North pole ( $k = 3/2$ ) node yields:

$$\frac{1}{r \sin \phi} \frac{\partial q_\phi q_\theta}{\partial \phi} \Big|_{i, j+\frac{1}{2}, \frac{3}{2}} \approx \frac{(q_\theta q_\phi)_{i, j+\frac{1}{2}, 2} - (q_\theta q_\phi)_{i, j+\frac{1}{2}, 1}}{r_{j+\frac{1}{2}} \sin \phi_{\frac{3}{2}} (\phi_2 - \phi_1)}, \quad (2.6)$$

that, again, is not singular neither at the North pole ( $\sin \phi_{3/2} \neq 0$ ) nor at the first radial node ( $r_{3/2} \neq 0$ ).

The evaluation of the viscous terms at the origin ( $r = 0$ ) and at the poles ( $\phi = 0$  and  $\phi = \pi$ ) benefits from the presence of the metrics that avoid the explicit computation of derivatives at these locations. For example, the discrete term  $(1/r^2)\partial/\partial r(r^2 \partial q_\theta/\partial r)$  in the  $q_\theta$  equation at  $j = 3/2$  is:

$$\frac{1}{r^2} \frac{\partial}{\partial r} r^2 \frac{\partial q_\theta}{\partial r} \Big|_{i, \frac{3}{2}, k+\frac{1}{2}} \approx \quad (2.7)$$

$$\frac{1}{r_{\frac{3}{2}}^2} \left[ \left( r^2 \frac{\partial q_\theta}{\partial r} \right)_{i,2,k+\frac{1}{2}} - \left( r^2 \frac{\partial q_\theta}{\partial r} \right)_{i,1,k+\frac{1}{2}} \right] / (r_2 - r_1),$$

that does not need the evaluation of  $\partial q_\theta / \partial r$  at  $j = 1$  being multiplied by  $r_1 \equiv 0$ .

Similarly, the term  $1/(r^2 \sin \phi) \partial / \partial \phi (\sin \phi \partial q_r / \partial \phi)$  of the  $q_r$  equation at the North pole reads:

$$\begin{aligned} & \frac{1}{r^2 \sin \phi} \frac{\partial}{\partial \phi} \sin \phi \frac{\partial q_r}{\partial \phi} \Big|_{i+\frac{1}{2},j,\frac{3}{2}} \approx \\ & \frac{1}{r_j^2 \sin \phi_{\frac{3}{2}}} \left[ \left( \sin \phi \frac{\partial q_r}{\partial \phi} \right)_{i+\frac{1}{2},j,2} - \left( \sin \phi \frac{\partial q_r}{\partial \phi} \right)_{i+\frac{1}{2},j,1} \right] / (\phi_2 - \phi_1) \end{aligned} \quad (2.8)$$

and it does not need the evaluation of  $\partial q_r / \partial \phi$  at  $k = 1$  since  $\sin \phi_1 \equiv 0$ . Note that the term  $1/r^2$  is not a problem because the  $q_r$  equation is evaluated only for  $j \geq 2$ .

Despite the change of variables and the staggered discretization still there are few terms that need a special treatment at the singular points; one of them is  $\partial / \partial r [r^2 \partial (q_r / r^2) / \partial r]$  of the  $q_r$  equation that for  $j = 2$  becomes

$$\begin{aligned} & \frac{\partial}{\partial r} r^2 \frac{\partial q_r / r^2}{\partial r} \Big|_{i+\frac{1}{2},2,k+\frac{1}{2}} \approx \left\{ r_{\frac{5}{2}}^2 \left[ \frac{(q_r)_{i+\frac{1}{2},3,k+\frac{1}{2}}}{r_3^2} - \frac{(q_r)_{i+\frac{1}{2},2,k+\frac{1}{2}}}{r_2^2} \right] / (r_3 - r_2) \right. \\ & \left. - r_{\frac{3}{2}}^2 \left[ \frac{(q_r)_{i+\frac{1}{2},2,k+\frac{1}{2}}}{r_2^2} - \frac{(q_r)_{i+\frac{1}{2},1,k+\frac{1}{2}}}{r_1^2} \right] / (r_2 - r_1) \right\} / (r_{\frac{5}{2}} - r_{\frac{3}{2}}), \end{aligned} \quad (2.9)$$

with the quantity  $(q_r)_{i+1/2,1,k+1/2}/r_1^2$  that can not be evaluated directly.

A possible strategy is to transform the derivative

$$\frac{\partial}{\partial r} r^2 \frac{\partial q_r / r^2}{\partial r} \equiv \frac{\partial^2 q_r}{\partial r^2} - \frac{\partial}{\partial r} \left( \frac{2q_r}{r} \right), \quad (2.10)$$

whose right hand side that can be computed in a straightforward way. It is worth mentioning, however, that the above equivalence is valid only in the continuum limit while differences arise when both sides are discretized.

A different approach is to maintain the formulation (2.9) and replace the singular quantity by a surrogate obtained by an average with the two counterparts ‘opposite’ to the singular point. This approach had already been used successfully for the axis of polar cylindrical coordinates by [41] and [158] although it has to be modified in the spherical case since the singularities at the centre and at the polar axis need a different treatment.

In the case of Equation (2.9) we recall that  $q_r / r^2 = u_r$  and use the second-order midpoint interpolation  $u_r(\theta, 0, \phi) = (u_r(\theta, \Delta r, \phi) - u_r(\theta + \pi, \Delta r, \pi - \phi)) / 2 + \mathcal{O}(\Delta r^2)$  in which the minus comes from the opposite orientation of the radial velocity in the mirror plane (Fig. 2.2a). With the discrete variables we have

$$\frac{q_r(i, 1, k)}{r_1^2} \approx \frac{1}{2} \left[ \frac{q_r(i, 2, k)}{r_2^2} - \frac{q_r(i + N_{ir}/2, 2, N_{kr} - k)}{r_2^2} \right], \quad (2.11)$$

with  $N_{ir} = N_i - 1$  and  $N_{kr} = N_k - 1$  the number of  $q_r$  points in the azimuthal and colatitude directions, that make possible the evaluation of the viscous term through (2.9).

All the other terms needing the evaluation at  $j = 1$  of  $q_r/r^2$  can be treated in the same way.

Similarly, for the  $q_\phi$  equation, the term  $(1/r)\partial(q_\phi q_\phi/\sin\phi)$  requires the evaluation of  $q_\phi/\sin\phi$  at  $k = 1$  and  $k = N_k$  which can not be done directly. Again we use the relation  $q_\phi/\sin\phi = u_\phi$  and write  $u_\phi(\theta, r, 0) = (u_\phi(\theta, r, \Delta\phi) - u_\phi(\theta + \pi, r, \Delta\phi))/2 + \mathcal{O}(\Delta\phi^2)$  that with the discrete variables becomes:

$$\frac{q_\phi(i, j, 1)}{\sin\phi_1} \approx \frac{1}{2} \left[ \frac{q_\phi(i, j, 2)}{\sin\phi_2} - \frac{q_\phi(i + N_{i\phi}/2, j, 2)}{\sin\phi_2} \right], \quad (2.12)$$

with  $N_{i\phi} = N_1 - 1$  and a similar expression for  $\phi = \pi$  ( $k = N_k$ ). The same approach can be adopted for the viscous term needing the evaluation of  $q_\phi/\sin\phi$  at the polar axis.

We remark that, differently from the sphere centre, at the polar axis there is no colatitude inversion to select the mirror point.

A possible cause of concern is that the special discretizations of some singular terms couple the meridional plane at  $\theta_i$  with that at  $\theta_i + \pi$  thus creating communication issues which would impede performance on highly parallel computers. This is however not the case since the above procedures require only one extra halo cell at the singular point and the involved data communication is irrelevant. In fact the same strategy is used in [144] for the equations in cylindrical coordinates that are solved on massive parallel computers using up to  $3.2 \times 10^4$  processors.

## 2.4 Numerical method

Equations (2.3, 2.4–2.6) are integrated using the fractional-step method detailed in section 1.5.1 and briefly summarised below. The momentum equation for  $\mathbf{q} = (q_\theta, q_r, q_\phi)$  is provisionally advanced in time using the old pressure field:

$$\frac{\hat{\mathbf{q}} - \mathbf{q}^l}{\Delta t} = \left[ \gamma^l \mathbf{N}^l + \rho^l \mathbf{N}^{l-1} - \alpha^l \nabla p^l + \alpha^l \frac{\hat{\mathbf{V}} - \mathbf{V}^l}{2} \right]. \quad (2.13)$$

Here the superscript  $l$  indicates the time-step level,  $\alpha^l$ ,  $\gamma^l$  and  $\rho^l$  are the coefficients of the time integration scheme (second-order Adams–Bashforth or third-order Runge–Kutta).  $\mathbf{N}$  contains the explicit nonlinear terms, body forces and the off-diagonal viscous terms, while  $\mathbf{V}$  the implicit diagonal viscous terms.

Since the pressure is not updated, the resulting velocity field is not locally free–divergent and is denoted by  $\hat{\mathbf{q}}$ . The correct velocity, however, must differ from the provisional one only by a gradient term, thus we can write:

$$\mathbf{q}^{l+1} = \hat{\mathbf{q}} - \alpha^l \Delta t \nabla \Phi, \quad (2.14)$$

whose divergence yields the elliptic equation for the unknown correction:

$$\nabla^2 \Phi = \frac{\nabla \cdot \hat{\mathbf{q}}}{\alpha^l \Delta t}. \quad (2.15)$$

Once the scalar field  $\Phi$  is determined, the solenoidal velocity  $\mathbf{q}^{l+1}$  is computed by Equation (2.14) and the new pressure through:

$$p^{l+1} = p^l + \Phi - \frac{\alpha^l \Delta t}{2Re} \nabla^2 \Phi. \quad (2.16)$$

The implicit treatment of the diagonal viscous terms of (2.13) would require the inversion of a large sparse matrix that is very time consuming; this is avoided by using the approximate factorization technique of [15] that requires only the inversion of three tridiagonal matrices with an error  $\mathcal{O}(\Delta t^3)$ .

Being the nonlinear convective terms computed explicitly, the equations should satisfy only the  $CFL = \max[\Delta t(|r \sin \phi \Delta \theta / u_\theta| + |\Delta r / u_r| + |r \Delta \phi / u_\phi|)]$  stability conditions that is  $CFL \leq 1$  for the Adams–Bashforth and  $CFL \leq \sqrt{3}$  for the third-order Runge–Kutta scheme. The off-diagonal viscous terms, however, are also computed explicitly to avoid the implicit coupling of the three momentum equations and this deteriorates the stability properties of the scheme. The actual  $CFL$  value used for the simulations therefore must be reduced with respect to the theoretical value and the amount of reduction depends on the Reynolds number and on the specific flow. In our applications we have found that halving the convective  $CFL$  limit yields a safe enough condition that allows the stable integration of the equations; it is worth mentioning, however, that this criterion must be taken as a rule of thumb and not as a strict limitation.

The current implementation of the method allows the use of generic non-uniform mesh distributions in the radial and colatitude directions. The reason for maintaining the uniform discretization in the remaining longitudinal direction is that we use trigonometric expansions and fast–Fourier–transforms to reduce the elliptic Equation (2.15) to a series of two-dimensional Helmholtz equations in the other two coordinates that are solved using the direct method of [149] or [98].

## 2.5 Validation

In this Section we assess the qualities of the proposed numerical method by showing several numerical examples and benchmarking them with the results from other codes or those available from the literature.

### 2.5.1 Hill vortex

As a first example we consider a spherical Hill vortex [68] which is an exact solution of the Euler equations and, in the inviscid limit, preserves its shape and propagates with a constant velocity along a rectilinear trajectory.

The vortex is defined by assigning its toroidal vorticity  $\omega = A\sigma$  within the sphere of radius  $a$  and centre  $C$  with an irrotational flow outside; the translation velocity of the ring is then  $U_0 = 2Aa^2/15$  (Fig. 2.3a) and the Reynolds number is defined as  $Re = 2aU_0/\nu$ . Different initial positions  $C$  and velocity orientations  $U_0$  have been simulated in order to stress the stability, the accuracy and the reliability of the method.

If not specified otherwise, the simulations have been performed in a domain of radius  $R = 7a$  discretized by a mesh of  $129^3$  nodes using  $Re = 2500$ .

In Fig. 2.3b we report the trajectory of the vortex, through the Cartesian coordinates of the velocity peak, that moves horizontally with a constant velocity and crosses the sphere centre ( $r = 0$ ) (Fig. 2.4). It can be noted that while  $Y_C$  and  $Z_C$  remain negligible in time,  $X_C$  increases linearly thus confirming the constant translation velocity. In fact, a close inspection of  $X_C$  reveals a small deviation with respect to the theoretical straight line; this is due to the finite viscosity of the flow ( $Re = 2500$ ) that perturbs the exact inviscid solution and deforms the initial vortex shape. That the vortex deformation is indeed due to viscosity and not to the discretization on spherical coordinates is confirmed by the results of Fig. 2.5 in which the same Hill vortex has been evolved using the code in Cartesian coordinates AFID [157]. From the same calculation we have extracted also the trajectory of the vortex that perfectly overlaps with its counterpart computed in spherical coordinates.

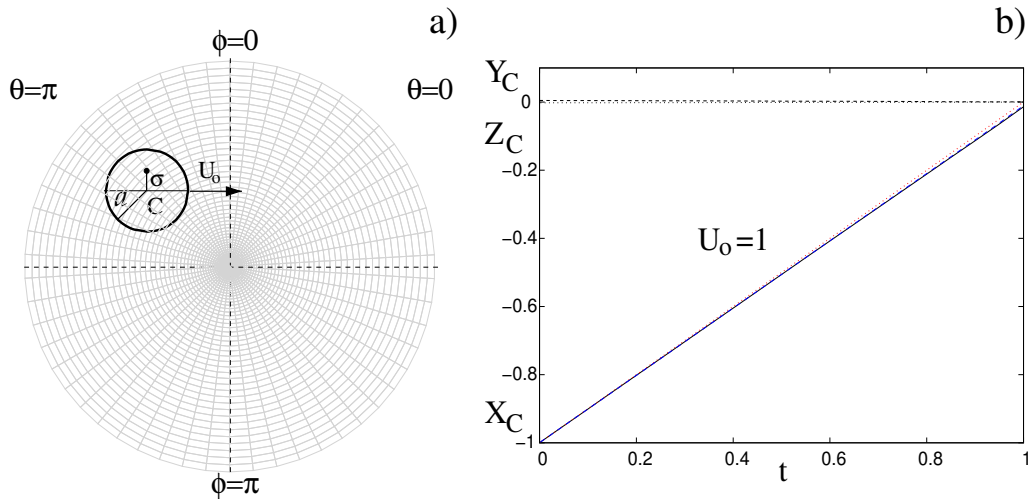


Figure 2.3: a) Sketch of the Hill vortex setup in the longitudinal sections  $\theta = 0, \pi$  of the spherical domain. b) Time evolution of the vortex centre coordinates for the case at  $Re = 2500$  with  $\theta_C = \pi$ ,  $r_C = 1$ ,  $\phi_C = \pi/2$ . —  $X_C = r_C \cos \theta_C \sin \phi_C$ ; ----  $X_C$  from the code in Cartesian coordinates [157], thin ..... theoretical  $X_C$ ; ----  $Y_C = r_C \sin \theta_C \sin \phi_C$ ; ——  $Z_C = r_C \cos \phi_C$ .

The same comparison between spherical and Cartesian codes has been repeated for a wide range of Reynolds numbers and in Fig. 2.6a we report the time evolution of the flow kinetic energy ( $K = 0.5 \int_V \mathbf{u}^2 dV$ ), normalized by the initial value, for several Reynolds numbers showing that, despite the very differ-

ent meshes, the kinetic energy decays always at an identical rate that depends only on  $Re$ .

Even if the results are the same, the simulations in spherical coordinates are more expensive than the Cartesian counterparts owing to the time step limitations introduced by the mesh around  $r = 0$ . For example, using the third-order Runge–Kutta as time integration scheme and a working  $CFL$  of 1.2, the simulation at  $Re = 2500$  on a  $129^3$  mesh in a  $4^3$  domain run with a time step  $\Delta t \simeq 2 \times 10^{-2}$  throughout the whole computation. The same case on the spherical mesh had  $CFL = 0.6$  with a dynamically adjusted time step of  $\Delta t \simeq 10^{-2}$  when the vortex was far from the sphere centre, and  $\Delta t \simeq 10^{-4}$  during the crossing phase. As a result, the CPU time for the latter simulation was about 14 times bigger than that of the former.

We wish to point out that the reason for this large computational overhead is the Hill vortex flow that, with its strongest velocity components perpendicular to the polar axis near the sphere centre, is particularly unsuitable for the spherical discretization. Nevertheless it has been chosen on purpose, in order to show that the numerical method can be used even in the most unfavourable conditions without loosing stability or precision. It is important to note that the time step limitation is mainly given by the discretization at the sphere centre and not by the polar axis. In fact, later in this section we show that when the Hill vortex has an initial offset of  $\phi_C = 2\pi/3$ , with respect to the symmetry plane  $\phi = \pi/2$ , the time step reduction during the crossing of the polar axis is only a factor  $\approx 3\text{--}4$  even if the largest velocity is still perpendicular to the coordinate line  $\phi = 0$ . Finally, in the next sections we will consider numerical examples in which the flow evolves in between two spherical shells and there the time step is limited only by the radial refinement of the mesh at the solid boundaries and not by the singularity at the polar axis.

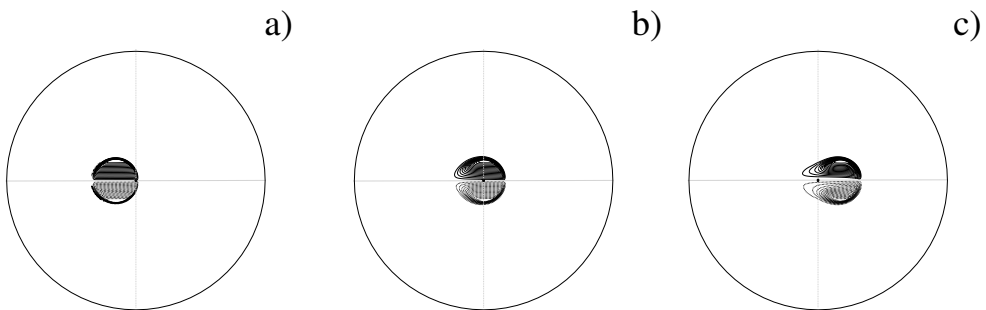


Figure 2.4: Time evolution of the Hill vortex at  $Re = 2500$  in the longitudinal sections  $\theta = 0, \pi$ ; longitudinal vorticity ( $\Delta\omega_\theta = \pm 0.4$ ) ..... for negative values; a) )  $t = 0.5$ , b)  $t = 1.$ , c)  $t = 1.5$ . Initial centre of the vortex:  $\theta_C = \pi$ ,  $r_C = 1$ ,  $\phi_C = \pi/2$ . Hereinafter, the black bullet indicates the origin of the spherical system.

Since the most critical phase of the simulation is the vortex centre crossing the point  $r = 0$ , here we have evaluated the code accuracy by assuming as reference

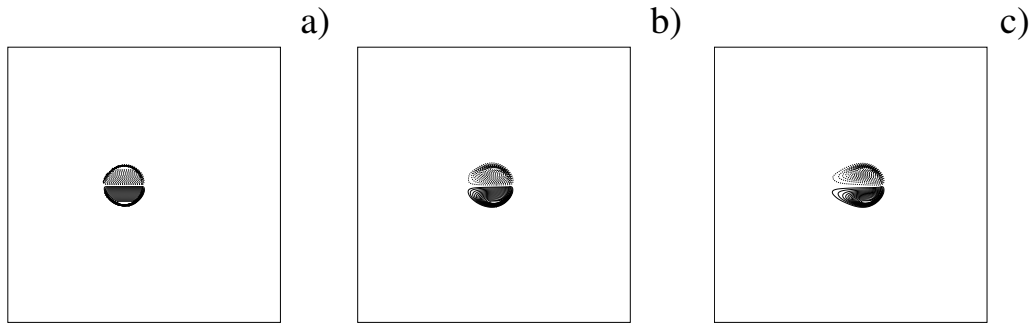


Figure 2.5: Time evolution of the Hill vortex at  $Re = 2500$  evolved on a Cartesian uniform mesh; out-of-the-page vorticity ( $\Delta\omega = \pm 0.4$ ) ..... for negative values; a) )  $t = 0.5$ , b)  $t = 1.$ , c)  $t = 1.5$ .

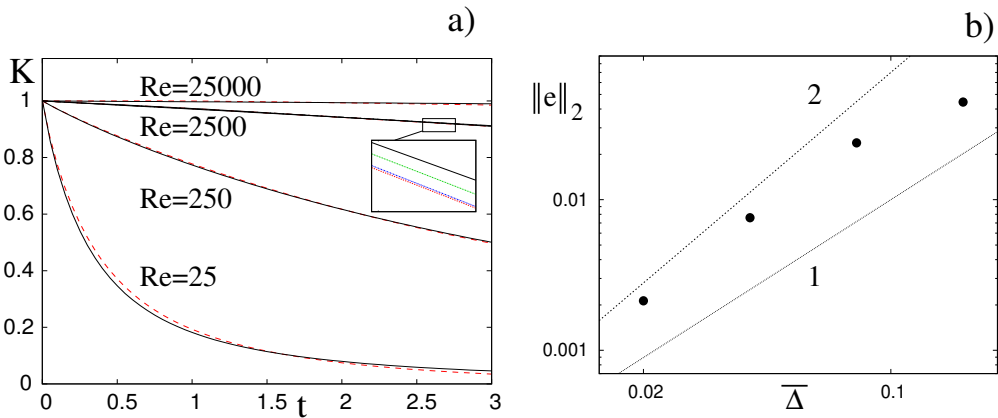


Figure 2.6: a) Decay of the total kinetic energy in time for the Hill vortex: — results from the code in spherical coordinates - - - results from the Cartesian code [157]. In the inset: — and  $Re = 2500$  for the Hill vortex with initial offset. — and  $Re = 2500$  for the Hill vortex resolved on a mesh refined around the singular points. b)  $L_2$ -norm of the error as function of the mesh size for the case at  $Re = 2500$ . ---- 2-slope, ..... 1-slope.  $\bar{\Delta}$  is the mean grid spacing defined as  $\bar{\Delta} \equiv [V/(N_i N_j N_k)]^{1/3}$  with  $V$  the volume of the computational domain.  $\theta_C = \pi$ ,  $r_C = 1$ ,  $\phi_C = \pi/2$ .

solution that performed on the finest mesh  $1459 \times 1297 \times 730$  (in  $\theta$ ,  $r$  and  $\phi$ ) and comparing it with grids successively coarsened by a factor 3 in each direction. This coarsening factor is such that, on a staggered mesh, it allows to compare the velocity components of different grids without interpolation and therefore to compute the raw accuracy of the numerical method. This set of simulations has been run with the same constant time step ( $\Delta t = 6 \times 10^{-6}$ ) that was imposed by the stability of the simulation run on the finest mesh.

In Fig. 2.6b we report the  $L_2$ -norm of the error computed for four meshes

and, apart for the coarsest ( $19 \times 17 \times 10$ ), the error decreases quadratically with the mesh size thus confirming the second-order accuracy.

We have further stressed the numerical method by giving the Hill vortex an initial offset with respect to the symmetry plane  $\phi = \pi/2$ . It can be observed from Fig. 2.7 that in this case no coordinate lines are aligned with the vortex axis and nevertheless the vortex translates along a horizontal rectilinear trajectory showing the same dynamics as in Fig. 2.4. Also the total kinetic energy of the flow decays in time in the same way as the other  $Re = 2500$  cases (Fig. 2.6a) and this confirms that the vortex evolution does not depend on the mesh orientation. Similarly to the case of Fig. 2.4, also for this simulation the time step has been dynamically computed in time to keep the *CFL* constant at the value of 0.6. In this case, however, it resulted  $\Delta t \simeq 10^{-2}$  at the beginning of the simulation and it decreased to  $\Delta t \simeq 2.7 \times 10^{-3}$  during the crossing of the polar axis. Considering that for a Hill vortex the largest velocity occurs at the centre, comparing Figs. 2.4b and 2.7b, it is clear that the most important limitation to the time step comes from the singularity around the sphere centre and not by that at the polar axis.

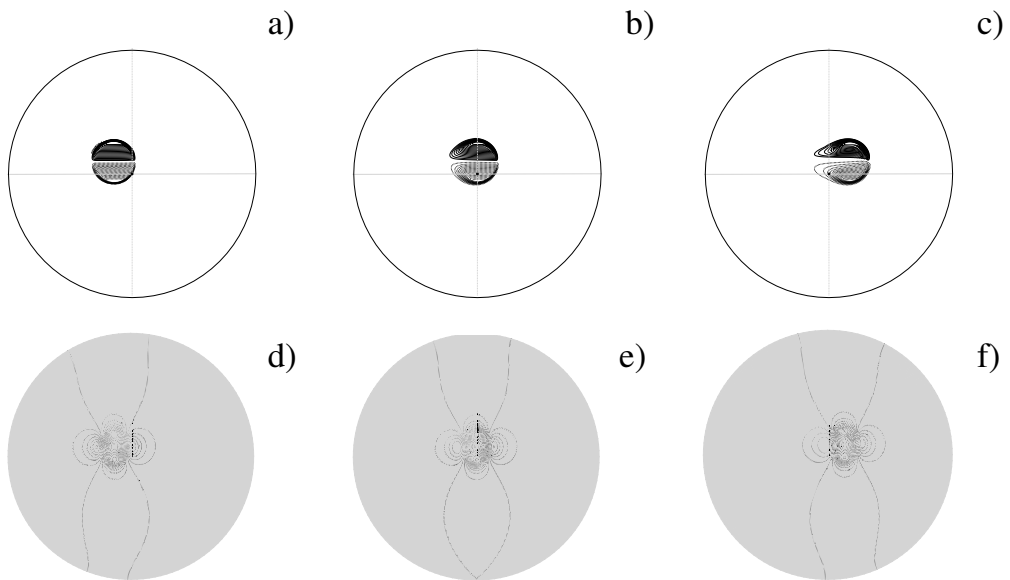


Figure 2.7: Time evolution of the Hill vortex at  $Re = 2500$  in the longitudinal sections  $\theta = 0, \pi$ ; top panels show longitudinal vorticity ( $\Delta\omega_\theta = \pm 0.4$ ) ..... for negative values; ( $\Delta u = 0.1$ ) bottom panels for pressure ( $\Delta p = 0.02$ ); the background mesh is shown with light gray lines. a) and d)  $t = 0.5$ , b) and e)  $t = 1.$ , c) and f)  $t = 1.5$ . Initial centre of the vortex:  $\theta_C = \pi$ ,  $r_C = 1$ ,  $\phi_C = 2\pi/3$ .

In another test we have positioned the vortex as in the case of Fig. 2.4 but the mesh has been refined at the sphere centre and at the polar axis (in both cases using a hyperbolic tangent distribution with stretching parameter 1.5) in order to exacerbate the stability problems of the integration in spherical coordinates. The results of Fig. 2.8a show that also in this case the vortex crosses the singular region without being distorted and the maximum divergence of the flowfield

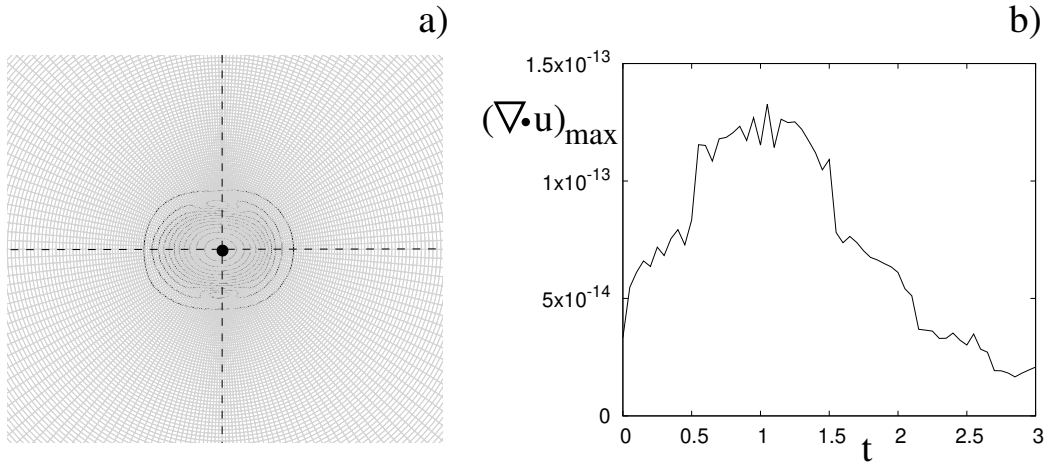


Figure 2.8: a) Zoom of velocity magnitude ( $\Delta u = 0.1$ ) of a Hill vortex at  $Re = 2500$  and  $t = 1$  in the longitudinal sections  $\theta = 0, \pi$ ; the computational mesh is refined on purpose around the singular points. b) Time evolution of the maximum divergence of the velocity field. Initial centre of the vortex:  $\theta_C = \pi$ ,  $r_C = 1$ ,  $\phi_C = \pi/2$ .

remains at machine precision throughout all the evolution (Fig. 2.8b). Also the total kinetic energy decay is identical to those of the other  $Re = 2500$  cases (Fig. 2.6a) again showing a vortex dynamics independent of the mesh distribution.

### 2.5.2 Flow in a precessing and spinning sphere

[12] validated their pseudo-spectral method by replicating the same problem as in [82] who studied the flow in a precessing and spinning sphere. We benchmark our code using the same test case and, referring to the sketch of Fig. 2.1, we consider flow inside a sphere of radius  $R$  spinning about the  $x$ -axis at constant angular velocity  $\Omega_s$ . The system has an additional precession angular velocity  $\Omega_p$  about the  $z$ -axis and the sphere surface ( $r = R$ ) is no-slip. Assuming  $R$  and  $\Omega_s R$ , respectively, as scaling length and velocity, the flow depends on two nondimensional parameters  $Re = \Omega_s R^2 / \nu$  and  $\Gamma = \Omega_p / \Omega_s$ .

Following [82], [12] we solve the equations in the precessing reference frame

$$\frac{\partial \mathbf{u}}{\partial t} + \nabla \cdot (\mathbf{u} \mathbf{u}) = -\nabla P - 2\Gamma \hat{k} \wedge \mathbf{u} + \frac{1}{Re} \nabla^2 \mathbf{u}, \quad \nabla \cdot \mathbf{u} = 0, \quad (2.17)$$

being  $\hat{k}$  the unit vector of the  $z$ -axis and  $P = p - (\Gamma^2/2)(\hat{k} \wedge \mathbf{r})^2$  the reduced pressure. The boundary condition for the nondimensional velocity at the sphere surface is  $\mathbf{u}|_{r=R} = \hat{x} \wedge \hat{r}$  with  $\hat{x}$  and  $\hat{r}$  the unit vectors of the  $x$ -axis and of the radius  $\mathbf{r}$ .

[82] analysed the flow for  $\Gamma = 0.1$  and  $Re \leq 500$  finding that a steady state is eventually achieved with increasingly entangled toroidal structures developed within the sphere. On the other hand, [12] observed that the flow structure could

be better understood by plotting the velocity field in a reference frame rotating with the spinning sphere  $\mathbf{v} = \mathbf{u} - \hat{x} \wedge \mathbf{r}$ .

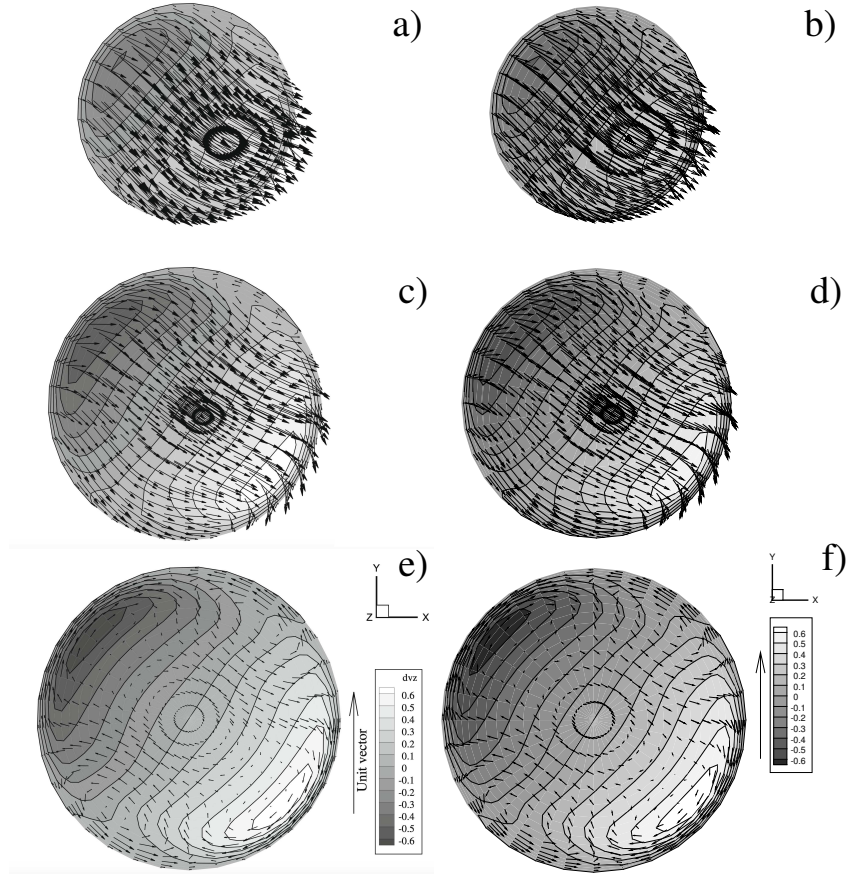


Figure 2.9: Flow in a precessing, spinning sphere at  $\Gamma = 0.1$  and  $Re = 500$ . The velocity vectors of the field rotating with the spinning sphere  $\mathbf{v}$  are reported in the sections  $z = -0.66$ , a) and d);  $z = -0.33$ , b) and e);  $z = 0$ , c) and f). The contours are for the velocity component  $v_z$ . a), c) and e) are the results adapted from Fig. 7 of [12], b), d) and f), present results.

Here we consider the case at the highest Reynolds number  $Re = 500$  and compare our results for the steady state solution of  $\mathbf{v}$  at the same three  $z = const$  planes as reported by [12]. The simulations have been performed at the same resolution and the comparison, given in Fig. 2.9, shows excellent agreement.

Once again we note that in this numerical example, being the flow velocities very small at the sphere centre (see Figs. 2.9cf) the integration could be carried out at constant  $CFL = 0.6$  with a nondimensional time step of  $\approx 4 \times 10^{-2}$  and the limitation was generated by the fine mesh stretched at the sphere surface rather than from the singular points of the spherical coordinates.

### 2.5.3 Rayleigh–Bénard convection with vertical gravity

In this example we consider the thermally driven flow developing between two concentric spheres of radii  $R_i$  and  $R_o$  whose surfaces are maintained at a temperature difference  $\Delta T$ , the inner being hotter than the outer. Following the arrangement of [42] the gravity has a constant orientation and points vertically downward as in Fig. 2.10a.

The flow is solved using the Boussinesq approximation described in section 1.4. In addition to the conservation of mass and balance of momentum (Equations 2.2) here we need also the energy conservation that reduces to the convection–diffusion equation for the temperature field. The complete set of governing relations in non-dimensional vector form then reads:

$$\begin{aligned} \nabla \cdot \mathbf{u} &= 0, \\ \frac{\partial \mathbf{u}}{\partial t} + \mathbf{u} \cdot \nabla \mathbf{u} &= -\nabla p - \hat{g}T + \sqrt{\frac{Pr}{Ra}} \nabla^2 \mathbf{u}, \\ \frac{\partial T}{\partial t} + \mathbf{u} \cdot \nabla T &= \sqrt{\frac{1}{RaPr}} \nabla^2 T. \end{aligned} \quad (2.18)$$

$Ra = g\beta\Delta t(R_o - R_i)^3/(\nu\kappa)$  is the Rayleigh number with  $\beta$  the isobaric thermal expansion coefficient,  $\kappa$  the thermal diffusivity of the fluid,  $g$  the magnitude of the gravity and  $\hat{g}$  its unit vector;  $Pr = \nu/\kappa$  is the Prandtl number. Referring to Equations (2.2) we can also write  $\hat{g} = (f_\theta, f_r, f_\phi) = (\sin\theta, \sin\phi\cos\theta, \cos\phi\cos\theta)$ .

Being the temperature a scalar quantity, it is located at the cell centre (Fig. 2.2) and the solution of the last of Equations (2.18) in spherical coordinates does not present particular challenges at the singular points.

In the present flow, a buoyant plume vertically rising is produced by setting the gravity vector aligned with the polar axis so that there are no velocity vectors crossing it. In order to show that the proposed numerical method performs well also in supposedly unfavourable conditions, we have repeated the simulation also with the gravity perpendicular to the polar axis.

In Fig. 2.10 we report the results for a case at  $\eta = R_i/R_o = 0.5$ ,  $Ra = 10^5$  and  $Pr = 0.7$  that, after an initial transient, attains a steady state.

A usual way to express the heat transfer in thermally driven flows is by the Nusselt number, defined as the ratio between the heat flux through a surface and its counterpart in absence of flow motion. For this problem it can be computed for the inner and the outer spheres to obtain:

$$Nu_i = -\eta \overline{\frac{\partial T}{\partial r}} \Big|_{r=R_i}, \quad Nu_o = -\frac{1}{\eta} \overline{\frac{\partial T}{\partial r}} \Big|_{r=R_o}, \quad (2.19)$$

where the  $\overline{\cdot}$  indicates surface and time averages: if the flow is steady or it attains a statistical steady state the two values have to match.

Fig. 2.10b shows the time evolution of the inner and outer Nusselt numbers for the simulations with the gravity in two perpendicular orientations; it can

be observed that not only they converge exactly to the same value but also the transient evolutions are indistinguishable. The asymptotic Nusselt number is  $Nu = 3.4105$  in excellent agreement with the values  $Nu = 3.4012$  of [42], 3.4890 of [33] 3.4648 of [37] and 3.3555 of [30].

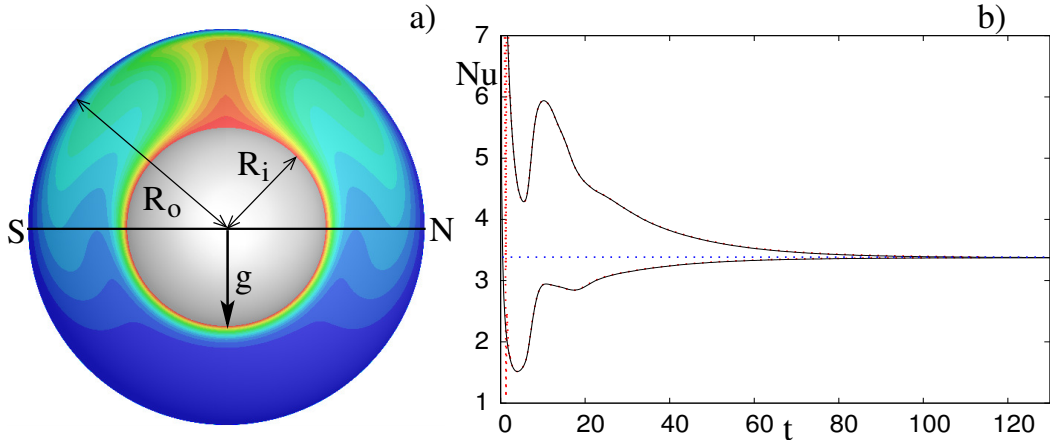


Figure 2.10: a) Section through the meridional planes  $\theta = 0, \pi$  of temperature contours ( $\Delta T = 0.1$ ) for the flow at  $\eta = R_i/R_o = 0.5$ ,  $Ra = 10^5$  and  $Pr = 0.7$ . Grid  $65 \times 49 \times 49$ . b) Time evolution of the Nusselt numbers — simulation with the gravity aligned with the polar axis, --- gravity perpendicular to the polar axis, ..... reference value of  $Nu = 3.4012$  from [42].

Another interesting result is that, no matter if the gravity is aligned or perpendicular to the polar axis, the simulation run at constant  $CFL = 1$  yielded a time averaged nondimensional time step  $\Delta t \approx 10^{-2}$  thus further confirming that the present numerical method alleviates the time step restrictions induced by the singularity at the poles.

#### 2.5.4 Rayleigh–Bénard convection with central gravity

In this numerical example we use the same configuration as in the previous section except for the gravity that now points towards the centre of the sphere.

We rely again on Equations (2.18) with the non-dimensional gravity vector that now reads  $\mathbf{g} = (f_\theta, f_r, f_\phi) = (0, g'(r), 0)$  with  $g'(r) = (R_o/r)^2$  the non-dimensional radial distribution of gravity. The reason for choosing this specific radial dependence is that, as shown by [49], in this case it is possible to derive exact relations among the Nusselt number and the dissipations:

$$Nu = \frac{Pr^2}{Ra} \frac{1 + \eta + \eta^2}{3} \epsilon_u + 1 = \frac{1 + \eta + \eta^2}{3\eta} \epsilon_T, \quad (2.20)$$

with  $\epsilon_u = <(\nabla \times \mathbf{u})^2>$  the kinetic energy and  $\epsilon_T = <(\nabla T)^2>$  the temperature variance–dissipation rates averaged over the fluid volume and in time, that can be used to verify both, the consistency of the numerical method and to assess the

statistical convergence of the results. In Fig. 2.11 we report the results for the case at  $\eta = R_i/R_o = 0.6$ ,  $Ra = 3 \times 10^4$  and  $Pr = 1$ . computed on a  $129 \times 97 \times 97$  mesh. It can be observed that, after the initial transient ( $t \leq 100$ ) the Nusselt numbers computed from Equations (2.19) and (2.20) oscillate around a common mean value and the simulation is stopped when their averages agree within 1%.

In addition to the heat transfer, also the strength of the flow is used to quantify the response of the system and, in non-dimensional form, it can be expressed by the Reynolds number. In [49] it was measured by computing the root mean square of the velocity field that, however, was scaled by the viscous velocity scale  $\nu/(R_o - R_i)$ . Since in Equations (2.18) we have used the convective velocity  $\sqrt{g\beta\Delta T(R_o - R_i)}$ , the root mean square Reynolds number  $Re'$  of [49] corresponds to the quantity  $\sqrt{2KRa/(VPr)}$  with  $V$  the fluid volume and  $K$  the kinetic energy of the flow.

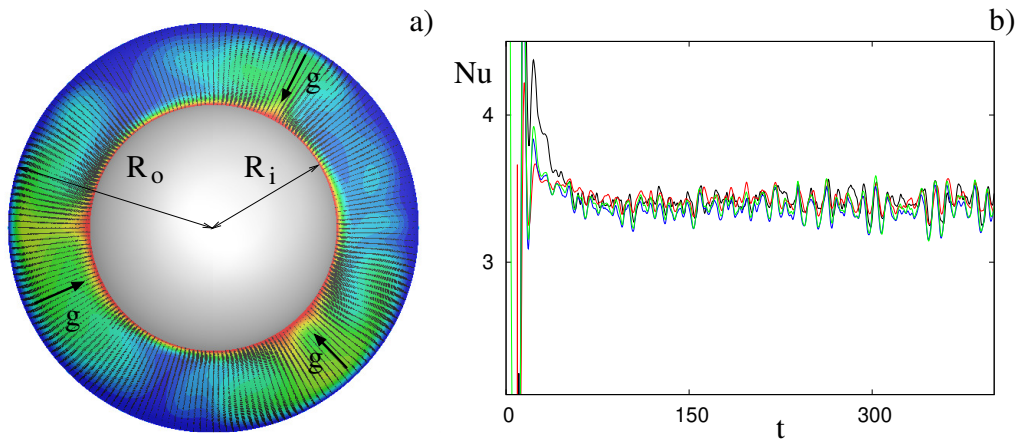


Figure 2.11: a) Section through the meridional planes  $\theta = 0, \pi$  of temperature contours ( $\Delta T = 0.1$ ) overlaid with velocity vectors for the flow at  $\eta = R_i/R_o = 0.6$ ,  $Ra = 3 \times 10^4$  and  $Pr = 1$ . Grid  $129 \times 97 \times 97$ . b) Time evolution of the Nusselt numbers: — value computed at the inner surface, — value computed at the outer surface, — value computed from  $\epsilon_u$ , — value computed from  $\epsilon_T$ .

In Table 2.1 we report the values of  $Nu$  and  $Re'$  for some cases that show excellent agreement with the analogous values obtained by [49]. In the sake of conciseness we have not presented the Nusselt numbers obtained by the dissipations from the expressions (2.20) that, however, deviate from those computed by the wall temperature gradients always by less than 1% for every simulation.

Cases #5–#7 are grid refinements of the same flow: it is worthwhile to note that Case #5 has a mesh that is coarser than Case #6 only in the radial direction and the results are still correct. For the radial distribution of the computational nodes of case #5 we have observed from Equations (2.19) that being  $Nu_i = Nu_o$  the temperature gradient at the inner sphere must exceed that at the outer sphere by a factor  $1/\eta^2$ . This implies that the wall resolution at the outer sphere can be coarser than that at the inner sphere and for the case at  $\eta = 0.6$ ,  $Pr = 1$  and  $Ra = 3.0 \times 10^4$  this resulted in a saving of about 25% of nodes. In this

case, in particular, the radial distribution of the nodes has been assigned as an input from an external file built by third-order splines with the conditions  $\Delta r = (R_o - R_i)/450$  at the inner sphere,  $\Delta r = (R_o - R_i)/200$  at the outer sphere and  $\Delta r = (R_o - R_i)/45$  halfway between the boundaries.

For these simulations, run only for validation purposes, this is not a crucial advantage since they can be run anyway within a few hours on a single Intel I7–2.7GHz processor. However, when the method is employed to tackle higher Rayleigh number flows implying meshes with hundreds of million ([49]) or billions ([144]) of nodes the asymmetric radial stretching of the mesh could become very attractive and this is possible thanks to the flexibility of the finite-difference schemes.

Case	$Ra$	$Nu$	$Re'$	$N_\theta \times N_r \times N_\phi$	$Nu$ [49]	$Re'$ [49]
1	$1.5 \times 10^3$	1.327	4.37	$65 \times 33 \times 49$	1.33	4.4
2	$3.0 \times 10^3$	1.812	9.70	$65 \times 33 \times 49$	1.80	9.6
3	$1.0 \times 10^4$	2.527	23.43	$65 \times 33 \times 49$	2.51	23.3
4	$1.5 \times 10^4$	2.828	29.83	$97 \times 65 \times 65$	2.81	29.8
5	$3.0 \times 10^4$	3.428	43.95	$97 \times 49 \times 65$	3.40	44.0
6	$3.0 \times 10^4$	3.443	43.94	$97 \times 65 \times 65$	3.40	44.0
7	$3.0 \times 10^4$	3.412	43.97	$129 \times 97 \times 97$	3.40	44.0
8	$5.0 \times 10^4$	3.924	57.24	$97 \times 65 \times 65$	3.89	57.5

Table 2.1: Main input and out parameters and comparison with the results from [49]. All the simulations are run at  $\eta = 0.6$  and  $Pr = 1$ .

### 2.5.5 Space-developing jet

In this last application we simulate the spatial evolution of a round jet of initial diameter  $d$  and mean inflow velocity  $U_{in}$  with a Reynolds number  $Re = U_{in}d/\nu$ . Here we follow the idea of [19] who noted that the coordinate lines of a spherical shell sector naturally follow the self-similar spreading of a jet. Another advantage is that the divergence of the  $\theta$ - and  $\phi$ -isolines yield a more refined mesh for small radii while it coarsens as the radius increases. The computational domain, reported in Fig. 2.12a, is defined as  $0 = \Theta_i \leq \theta \leq \Theta_f = \pi/6$ ,  $R_i = 3 \leq r \leq 12 = R_o$ , and  $11\pi/12 = \Phi_i \leq \phi \leq \Phi_f = 13\pi/12$  and, since it does not contain any of the singular points, the solution of the governing equations is performed easily. In fact, the reason for performing this last test case has not to do with the equation singularity but rather with the possibility of the scheme to deal with ‘complex’ boundary conditions.

At the inner boundary ( $r = R_i$ ) a radial velocity profile with mean  $U_{in}$  is prescribed within the circle of diameter  $d$  and centre  $([\Theta_i + \Theta_f]/2, [\Phi_i + \Phi_f]/2)$  and perturbed with a white noise of amplitude  $0.02U_{in}$ . At the outflow we impose

the convective boundary condition as in [123]:

$$\frac{\partial q_i}{\partial t} + U_R \frac{\partial q_i}{\partial r} = 0, \quad (2.21)$$

that advects all the velocity components  $q_i$  out of the domain with the velocity  $U_R$  that is dynamically adjusted to assure mass conservation to the machine precision. Periodicity is imposed in the azimuthal and colatitude directions.

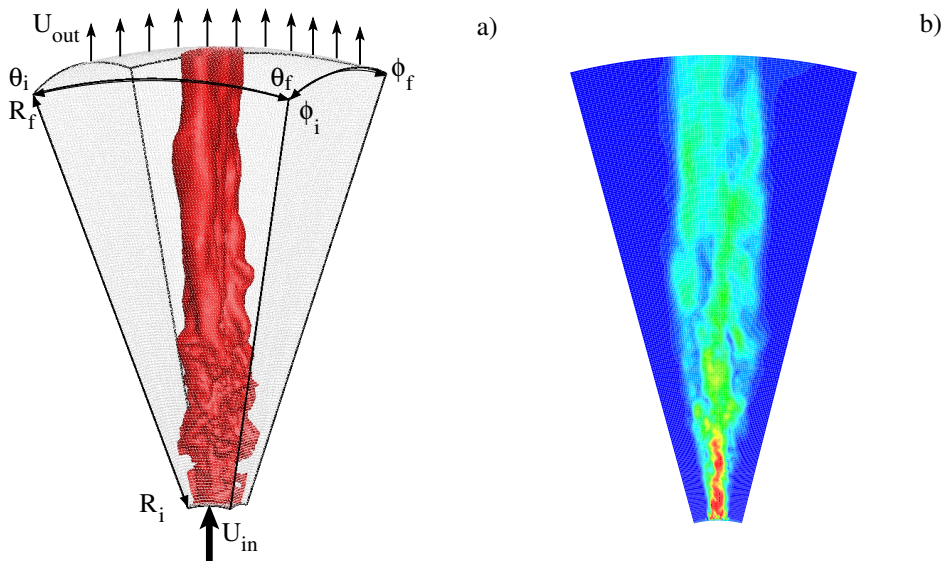


Figure 2.12: a) Computational set-up for the space developing jet. The isosurface is velocity magnitude  $|u| = 0.2$ . b) Instantaneous snapshot plane section ( $\theta = (\Theta_i + \Theta_f)/2$ ) of velocity magnitude (from blue to red)  $\Delta |u| = 0.1$ .

The simulation has been performed on a mesh of  $97 \times 257 \times 97$  nodes at a Reynolds number  $Re = 5000$  and an instantaneous snapshot of the velocity magnitude through the mean plane  $\theta = (\Theta_i + \Theta_f)/2$  is shown in Fig. 2.12b.

We wish to point out that our azimuthal and colatitude periodic boundaries are different from those of [19] who used traction-free conditions [57] at these lateral planes. The latter (obtained by imposing the scalar product between the total stress tensor and the boundary normal to be zero) are certainly more correct since they allow flow transpiration without yielding stress in contrast to periodicity that, representing an infinite array of jets, unavoidably induces some confinement. Owing to this important difference, we do not make any quantitative claim about the dynamics of the jet and do not attempt comparisons with [19]; we use this calculation only to show the flexibility of the proposed method that allows within the same ease the imposition of simple, homogeneous boundary conditions, such as the no-slip of sections 2.5.3 and 2.5.4, and the inhomogeneous inflow/outflow conditions of the space-developing jet.

## **2.6 Concluding remarks**

In this chapter we have shown that the combination of a change of variables with a central-, second-order accurate finite-differences on a staggered mesh and the special treatment of some discrete terms removes the singularities of the Navier–Stokes equations for an incompressible viscous flow in spherical coordinates.

Some numerical applications have been considered with the aim of stressing the stability of the scheme and its capability to reproduce reference results.

Most of the tests have been performed using a spherical Hill vortex that, in the inviscid limit, is an exact solution of the governing equations and propagates along a rectilinear trajectory with a constant velocity. The numerical procedure has shown to be second-order accurate and to reproduce the results obtained for the same flows by a code in Cartesian coordinates. The method performed equally well even when the vortex centre was offset with respect to the symmetry plane  $\phi = \pi/2$  or the mesh was unnecessarily refined around the singular points.

Another benchmark has been performed by simulating the flow within a precessing, spinning sphere for the same parameters as those considered by [82] and [12] obtaining a perfect agreement with their results produced by spectral methods.

Equally good results have been obtained for thermally driven flows in which only the singularity at the polar axis was present although the flow physics was enriched by the presence of the additional temperature field; the heat transfer of these flows was always in excellent agreement with other similar studies and even the exact relations between heat transfer and dissipation rates were perfectly satisfied.

An important drawback related to the spherical coordinates is the time step limitation introduced by the discretization around the singularities. The proposed numerical method has shown to alleviate this problem for the polar axis and, for the flow in spherical shells with the grid stretched radially at the solid boundaries, the restriction induced by the latter outweighs that of the former. On the other hand, the singularity at the sphere centre still introduces strong time step limitations, although only if the largest flow velocity occurs there.

Although the merits of the proposed numerical method have been evidenced by reproducing simple canonical flows, for which benchmark results are available, its main merits are related to the flexibility of finite-differences. In the evolution of a space developing round jet (Section 2.5.5) we have qualitatively shown the possibility to use complex inflow/outflow boundary conditions while for the thermal convection with central gravity we have employed generic nonuniform meshes (Case # 5 of Section 2.5.4).

These finite-difference features are particularly appealing if the code has to be applied to realistic flows, such as the mantle convection of a planet [128], in which complex boundary conditions, but also inhomogeneous forcings and variable fluid properties, have to be accounted for.

Another important advantage of finite-difference methods is the relative ease

of parallelization related to the local nature of the discrete differencing; this is true also for the present scheme inspired by that of [158] and with the same variable arrangement and memory layout. The latter has been massively parallelized in [144] and run on up to  $3.2 \times 10^4$  cores. Also the present scheme in spherical coordinates has been parallelized.

In the following chapters we will analyse in more details some of the applications of this parallelised version: the characterization of thermally driven flows between spherical shells and the effect of an off-centered gravity for Rayleigh-Bénard convection flows.



## CHAPTER 3

# Effect of gravity profiles on Rayleigh-Bénard convection in spherical shells\*

### 3.1 *Introduction*

Natural convection in spherical domains has been the focus of many studies thanks to the vast number of possible applications in different fields. This topic has been studied experimentally [17], analytically [99], and more recently numerically [48]. Many modern applications include geoscience, cosmoclimatology [148, 147], as well as exploration of extraterrestrial moons [43] and various engineering applications. Convection in spherical shells differs from the classical Rayleigh-Bénard convection in a planar layer configuration [138, 2, 29] due to the curvature of the plates, the radial dependence of buoyancy, and the geometrical asymmetry between the boundary layer at the inner and outer spheres [20, 139, 73, 153, 134, 38, 109, 49].

When considering a radial gravity profile, the main focus has been often on internal heat source problems, mostly due to their relevance to geophysics [21, 75]. Performing direct experiments with radial gravity on the surface of the Earth is a very demanding task, due to the presence of vertical gravity. Therefore this kind of experiments have been performed during space missions: on the Space Shuttle [65] and on the International Space Station [46, 156], where a micro-gravity with a profile  $g(r) \propto r^{-5}$  has been used.

Extensive studies focus on spherical Rayleigh-Bénard convection, mainly because the gravity center coincides with the geometric one. For the cases near the onset of convection, [21] found qualitative differences between convective patterns of odd and even spherical harmonic order by the perturbation analyses where solutions with different wavenumber differ only quantitatively in a planar configuration. With  $Ra$  up to 100 times larger than the critical value, [16] found the convective pattern persists with the solutions by perturbation analyses. When  $Ra$  is as high as  $Ra > 10^5$ , [72] showed that the axisymmetric convective patterns breakdown and flow patterns start to show time-dependent behavior, which is

---

\*Based on L. Santelli, G. Wang, D. Lohse, R. J. A. M. Stevens, R. Verzicco *Effect of gravity profiles on Rayleigh-Bénard convection in spherical shells*, in proceeding 2020APS..DFDF16019S

characterized by upwelling and downwelling thermal plumes [16, 164, 47, 49]. The thin sheet-like thermal plumes are formed near the inner and outer spheres, and these plumes undergo morphological change into mushroom-like plumes when they eject from the boundary layers to the bulk [49]. In the core region, the downwelling and upwelling flow originates from the boundary layers concentrate gradually into cylindrical flows [164]. Such morphology and dynamics of thermal plumes are, in fact, similar to the situation of classical Rayleigh-Bénard convection with planar configuration.

There are also studies on the heat transport properties in spherical Rayleigh-Bénard convection (the  $Nu - Ra$  relationship  $Nu \propto Ra^\gamma$ ). With  $Ra$  up to  $Ra = 10^6$ , [117] and [72] proposed  $\gamma \sim 0.25$  for  $\eta = 0.55$ , but [49] predicted  $\gamma \sim 0.28$  for  $\eta = 0.6$ . At higher  $Ra$ , [164, 49] found a higher  $\gamma$ . [164] presented  $\gamma \sim 0.3$  with  $Ra$  up to  $Ra = 10^8$ , while [49] predicted  $\gamma \sim 0.32$  with  $Ra$  as high as  $Ra = 10^9$ . The scaling  $\gamma$  is  $Ra$  dependent and smaller than the typical  $1/3$  power of  $Ra$  predicted by boundary layer theory [101], but in good agreement with  $0.28 \lesssim \gamma \lesssim 0.31$  suggested by the unifying theory of thermal convection [58, 59]. However, the heat transport and flow properties also depend on the boundary conditions, the aspect ratio  $\eta$ , and the employed gravity profile [73, 117, 153, 134, 38, 109, 49], which need to be better understood.

For what concern numerical schemes, [158] have shown that, in the case of cylindrical problems, symmetries in the grid structure may cause perturbations in the fluid evolution, thus is suggested to use models with an appropriate grid symmetry. [49] raise a similar concern, suggesting that a direct application of planar geometry models to spherical models is questionable, and direct numerical simulations in spherical shells are required. There exist some numerical simulations for non rotating radial gravity model with finite Prandtl number [49, 153] but the vast majority of them has been done with infinite Prandtl number, since this can be used to model a good approximation of the Earth mantle [165, 16].

Stability analysis, an important tool to characterize fluid behaviour, has been often used in the case of vertical gravity [155, 130, 131, 42]. The literature about application of this powerful tool to the scenario of non rotating spherical shells with radial gravity is more scarce: it has been analysed by [7], and further developed by [13, 102]. In the study of [7], a parameter-dependent radial gravity is used to perform a linear asymptotic analysis for  $R \gg 1$  and compare these theoretical results with numerical simulations at various different radii. The work of [13] uses gravity profiles of  $g \propto r$  and  $g \propto r^{-2}$  to perform analytical and numerical studies, finding a lower boundary for the critical Rayleigh number and some examples of most unstable modes. More recently, [102] used [7] framework to perform an analysis with considerations for weakly nonlinear mode interaction under the assumption of an axisymmetric spherical convection.

In this chapter we want to characterise the Rayleigh-Bénard convection of two common fluids, air and water, confined between two spherical shells in a non-rotating environment. The effect of different radial gravity profiles on the onset of convection and the structure of the flow is analysed.

The chapter is organized as follows: the physical problem is described in section 3.2 together with the numerical discretization, the behaviour of  $Nu$  as a

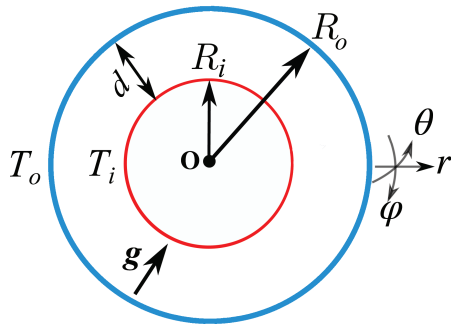


Figure 3.1: Sketch of the configuration.

function of  $Ra$  and the spectral analysis for both water and air, together with the rest of the results, are shown in section 3.3 and a final discussion is presented in section 3.4.

## 3.2 Numerical simulation

### 3.2.1 Problem description

The configuration of the problem, a sketch of which is given in figure 3.1, consists of an inner spherical shell of radius  $R_i$  and an outer concentric shell of radius  $R_o$ . We call  $d = R_o - R_i$  the distance between the shells. The aspect ratio  $\eta = R_i/R_o$  is fixed at  $\eta = 0.71$ . The fluid is subjected to a radial gravity of the form  $\mathbf{g}(r) = g_o \mathbf{g}^*(r)$ , where  $g_o$  is the magnitude of the gravity at the outer sphere and  $\mathbf{g}^*(r)$  a dimensionless radius-dependent function. A fixed temperature is set for inner and outer walls, with the outer wall temperature  $T_o$  being lower than the inner one  $T_i$ , and  $\Delta T = T_i - T_o$  the temperature difference. No-slip boundary conditions are chosen.

Let  $\nu$  the thermal viscosity and  $\kappa$  the thermal diffusivity of the fluid, then the Prandtl number is defined as  $Pr = \nu/\kappa$ . The setup for most of the following sections involves air, so we fix  $Pr = Pr_{air} = 0.71$ . For water, analysed in section 3.3.4,  $Pr_{water} = 7.1$  is used. Being  $\alpha$  the thermal expansion coefficient, the Rayleigh number is defined as  $Ra = \frac{g_o \alpha \Delta T d^3}{\nu \kappa}$ , and it will be used as the main control parameter in the following sections.

Reynolds number is defined as  $Re = U d / \nu = \sqrt{Ra/Pr}$ , where  $U$  is a free-fall velocity  $U = \sqrt{g_o \alpha \Delta T d}$ . The introduction of  $U$  allows us to set the representative scale for length ( $d/U$ ), time ( $d/U$ ) and temperature ( $\Delta T$ ).

The Nusselt number  $Nu$  is used to measure the dimensionless heat transfer between shells, and it has been computed by direct measurement of heat flux at

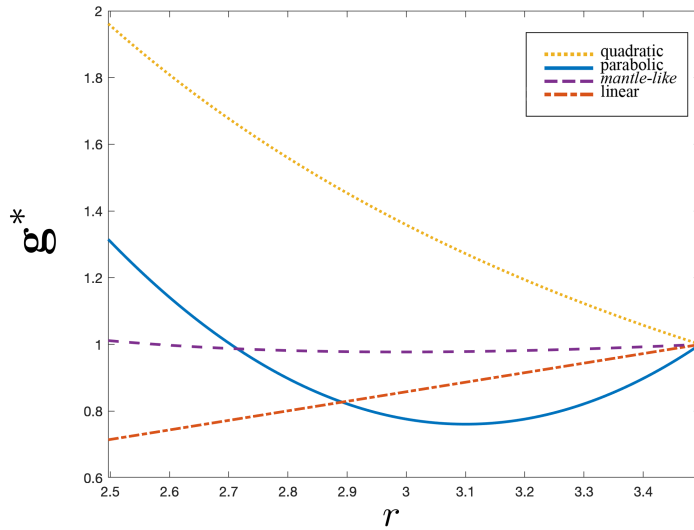


Figure 3.2: Overview of the dimensionless gravity profiles used (summarised in table 3.1) as a function of radius: ..... quadratic gravity; —— parabolic gravity; - - - mantle-like gravity; - - - linear gravity.

Name	Quadratic	Constant	Linear	Mantle-like	Parabolic
Symbol	$\mathbf{g}^q$	$\mathbf{g}^c$	$\mathbf{g}^l$	$\mathbf{g}^m$	$\mathbf{g}^p$
Equation	$\frac{1}{r^2}$	1	$r$	$\frac{R_i^3}{r^2}(\lambda - 1) + r$	$(r - R_m)^2 + \Delta R$

Table 3.1: Different gravity profiles.  $\lambda$ ,  $R_m$  and  $\Delta R$  are parameters.

outer and inner shells  $Nu = \eta \frac{\partial \overline{T^*}}{\partial r} \Big|_{R_i} = -\frac{1}{\eta} \frac{\partial \overline{T^*}}{\partial r} \Big|_{R_o}$ , with  $\overline{T^*(r)}$  being the dimensionless mean temperature as in equation (2.19). The two different definitions of  $Nu$  have been compared for all the simulations, always showing an excellent agreement.

Computing a typical diffusive time  $t_d = Re/Nu$  ensure that every simulation is run for sufficient time.

Finally, the density of the system is defined as  $\rho = \rho_o \alpha T$ , with  $\rho_o$  being the density at the outer shell. Using these quantities the problem is defined by a dimensionless Navier-Stokes equation for an incompressible viscous fluid under the Boussinesque approximation that reads as:

$$\left\{ \begin{array}{l} \frac{D\mathbf{u}^*}{Dt^*} = -\nabla p^* + T^* \mathbf{g}^*(r) + \sqrt{\frac{Pr}{Ra}} \nabla^2 \mathbf{u}^* \\ \nabla \cdot \mathbf{u}^* = 0 \\ \frac{DT^*}{Dt^*} = \frac{1}{\sqrt{RaPr}} \nabla^2 T^* \end{array} \right. \quad (3.1)$$

with  $\mathbf{u}^*$  and  $p^*$  being respectively the dimensionless velocity and pressure.

Different gravity profiles have been used for the simulations. They are schematized, together with the associated symbols, in table 3.1, while their shape is shown in figure 3.2. Two particular cases are present in the table: the first,

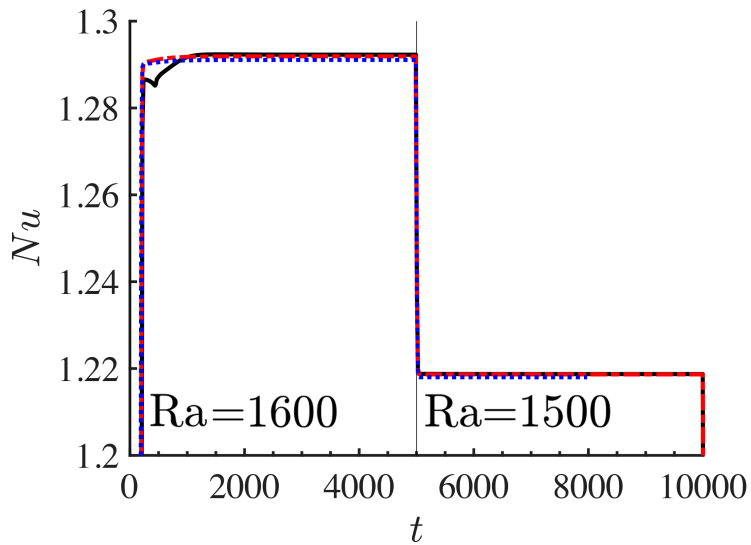


Figure 3.3: Analysis of  $Nu$  vs  $t$  at different number of grid points. — grid with ( $N_\theta = 33, N_r = 35, N_\phi = 35$ ) points; - - - (65, 69, 69); ····· (129, 121, 121). Only a small mismatch at the beginning of the simulation is present for the less refined grid, while the other two are almost coincident at every step. A vertical black line separate the two different  $Ra$  analysed:  $Ra = 1600$  for  $t < 5000$ ,  $Ra = 1500$  after.

called *Mantle-like*, aims to model a situation in which two different densities are present in the system, an inner density  $\rho_i$  that fills the inner sphere, and an outer density  $\rho_o$  for the space between the two shells. Their ratio, defined as  $\lambda = \rho_i/\rho_o$ , can be used as a parameter to analyse different situations, and it is set to  $\lambda = 2.9$  in this study. The second it is a parabolic profile artificially created to simulate a highly non-monotonic gravity, with  $R_m = 3.1$  and  $\Delta R = 0.5$  being parameters chosen to have a non-monotonic asymmetric (with respect to the middle radius) profile. In the following sections results will be shown for the case  $\mathbf{g} = \mathbf{g}^q$ , and the behaviour of other gravity profiles will be discussed alongside.

Henceforth asterisks of dimensionless quantities are dropped in order to simplify the notation.

### 3.2.2 Numerical setup

The evolution of equation (3.1) is simulated using the numerical scheme discussed in chapter 2. Being the singularity at the center of the sphere outside of our analysed domain, the parallelization of the code has been easily implemented. The appropriate space resolution has been chosen by running several simulations with varying grid spacing. In figure 3.3 is shown the behaviour of  $Nu$  as a function of time for different grid resolutions and values of Rayleigh number: the difference between the two most refined grid shown is negligible, therefore we can save computational time by running simulations on a

$Ra$	$\eta$	$n_g$	$N_\theta, N_r, N_\varphi$	$Nu$	$Nu(\text{ref})$	$Re_{rms}$	$Re_{rms}(\text{ref})$
$7 \times 10^6$	0.3	1	181,73,181	6.42	6.40	282.2	287.2
	0.3	0	181,73,181	8.19	8.15	377.5	377.8
$3 \times 10^7$	0.3	1	251,93,163	9.39	9.38	592.0	595.5
$5 \times 10^6$	0.35	1	257,55,257	6.80	6.74	274.8	274.1
$3 \times 10^8$	0.35	1	577,119,577	21.47	21.23	1815.6	1824.8
$5 \times 10^6$	0.6	0	257,71,257	11.85	11.68	437.3	442.7
$1 \times 10^6$	0.6	-2	325,71,325	9.02	8.90	255.4	259.2
$3 \times 10^4$	0.6	-2	129,49,97	3.42	3.40	44.1	44.0

Table 3.2: Parameters of the spherical RB simulations with  $Pr = 1$ , which are compared to the results ( $Nu(\text{ref})$  and  $Re_{rms}(\text{ref})$ ) of [49].  $N_{\theta,r,\varphi}$  indicates the number of grid points in the longitudinal, radial, and co-latitudinal direction, respectively.

grid  $\{N_\theta = 65, N_r = 69, N_\phi = 69\}$ . A maximum  $CFL = 0.8$  has been imposed to control the size of the time step during the convective phase, while  $\Delta t_{max} = 10^{-3}$  has been fixed for the linear evolution.

We extensively validated our code against the results presented by [49], who performed a systematic parameter study for spherical RB convection with  $Pr = 1$  covering radius ratios  $0.2 \leq \eta \leq 0.95$  for different gravity profiles  $g \propto r^{n_g}$ , with  $n_g = -5, -2, 0$  and  $1$ . Some of our tests are shown in Table 3.2, which shows that the Nusselt number  $Nu$  and the time and volume averaged Reynolds number  $Re_{rms} = \sqrt{\langle u_\theta^2 + u_r^2 + u_\phi^2 \rangle}$  agree within 2% with the results from [49] for all cases.

The initialization and evolution of the system varies according to the specific parameters that have been used for each simulation:

- Low  $Ra$ , increasing: for these simulations the flow is initialised to a rest state at  $Ra < Ra_c$ , with  $Ra_c$  being the critical Rayleigh number for the onset of convection. It is then allowed to evolve unperturbed for a sufficiently long time in order to reach and maintain an equilibrium state. At this point,  $Ra$  is increased to a new value and the equilibrium procedure is repeated. These steps are repeated until  $Ra$  reached the desired value. This long-time evolution is mostly necessary for the first steps, as the absence of perturbation and the accuracy of the code drastically increase the needed time for the onset of convection.
- Low  $Ra$ , decreasing: These simulations follow the same procedure as the increasing case, but the initialization is done at  $Ra \geq Ra_c$  and the subsequent values of  $Ra$  are in a decreasing order. Less time per  $Ra$ -step is needed, since the system stabilise faster.
- High  $Ra$ : simulations done at higher values of Rayleigh number focus on the properties of the flow at a fixed value of  $Ra$ , so, after the initialization at the chosen  $Ra$  from a pre-existing simulation, the fluid is left free to evolve

without variations in parameters for a time sufficiently long to observe the complete behaviour.

The few cases that require a different approach will be described in their relative sections. In all the simulations, the flow needed a few time steps to reach a divergence free state, thus data are only collected after this condition has been reached.

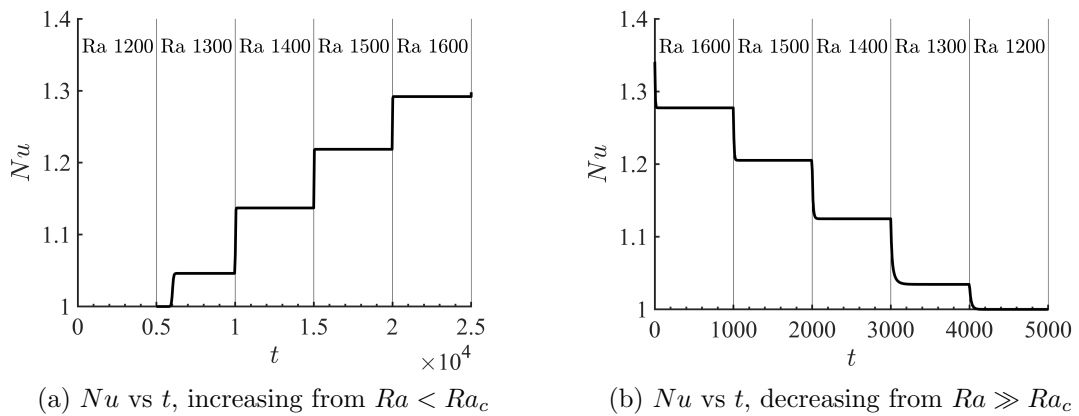


Figure 3.4: Evolution of  $Nu$  as function of  $t$ . Vertical bars of (a) and (b) separate zones with different  $Ra$ .

### 3.3 Results

#### 3.3.1 Onset of convection

The behaviour of  $Nu$  as a function of  $Ra$  and  $t$  varies accordingly to the range of  $Ra$  analysed. For  $Ra$  lower than the critical value for the onset of convection,  $Nu = 1$ . An interval of Rayleigh number around  $Ra_c$  is shown in figure 3.4 for the quadratic gravity profile  $g^q$ . As described in the previous section, in the increasing case we set initial conditions at  $Ra \leq 1200$ , then the fluid is left free to evolve for a long enough time ( $5 \times 10^3$  time units for figure 3.4a) until  $Ra$  is updated according to  $Ra_{new} = Ra_{old} + \Delta Ra$ ; the decreasing case starts from a much higher  $Ra$  and it is then update following  $Ra_{new} = Ra_{old} - \Delta Ra$ , with  $\Delta Ra$  being a parameter used to refine the precision of the analysis (for figure 3.4,  $\Delta Ra = 100$ ). For this range of values of  $Ra$ ,  $Nu$  is not time dependent at any fixed value of the Rayleigh number, so the mean value of it, shown in figure 3.5, has been computed to compare the increasing- and decreasing- evolutions: from the figure is immediate to notice that the two approaches are different. Some

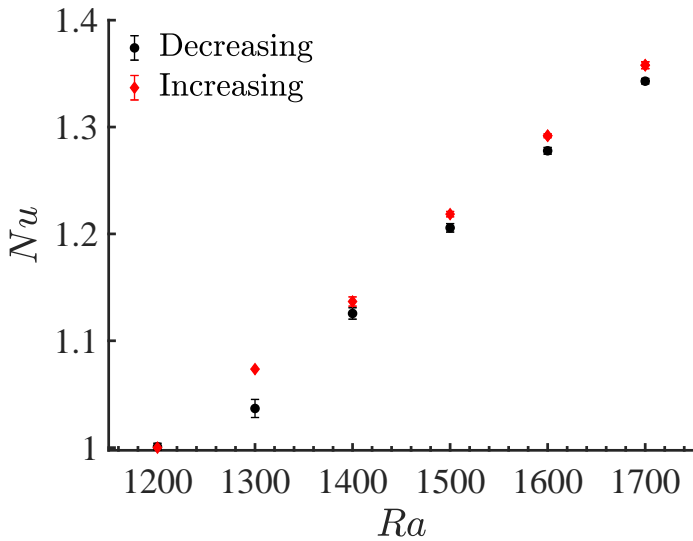


Figure 3.5: Evolution of  $Nu$  as function of  $Ra$ .  $\diamond$  red diamonds for increasing- $Ra$ ,  $\bullet$  black circles for decreasing- $Ra$ . Error bars shown when bigger than the symbols.

Gravity	Quadratic	Linear	Constant	Mantle-like	Parabolic
$Ra_c$	$1240 \pm 1\%$	$2020 \pm 1\%$	$1730 \pm 1\%$	$1610 \pm 1\%$	$2110 \pm 1\%$
$Ra_c^e$	$1737 \pm 1\%$	$1735 \pm 1\%$	$1730 \pm 1\%$	$1739 \pm 1\%$	$1907 \pm 1\%$

Table 3.3: Critical Rayleigh  $Ra_c$  and effective critical Rayleigh  $Ra_c^e$  for different gravity profiles.  $Ra_c^e$  coincides for all the profiles except the parabolic.

details on this behaviour will be given in the following sections, and a deeper analysis on the phenomenon is carried out in section 3.3.3.

The critical value for the onset of convection is identified when  $Nu(Ra)$  becomes greater than one, and it is  $Ra_c^q \approx 1240$  for quadratic gravity. The same study has been performed for the other gravity profiles: results from this analysis are showed in table 3.3 and are in good agreement with results from [7]. It should be noted that the actual Rayleigh number is not a constant, but rather a function of the gravity. The value  $Ra$  is computed at the outer sphere, but to take into account its variation along the sphere, an effective Rayleigh number  $Ra^e$  has been computed as well, by integrating over the radius the value of  $Ra(g(r))$ :

$$Ra^e = \frac{1}{d} \int_{R_i}^{R_o} dx Ra(x) \equiv \frac{1}{d} \int_{R_i}^{R_o} dx Ra \frac{g(x)}{g_o}. \quad (3.2)$$

Table 3.3 shows and enforces the importance of the effective Rayleigh number by highlighting how  $Ra_c^e$  is very similar for almost all the cases analysed, with the only exception of the parabolic case. A possible explanation of this deviation is that the parabolic case is the only non-monotonic gravity profile analysed here, and this might have an effect on the onset of convection. The Mantle-like profile

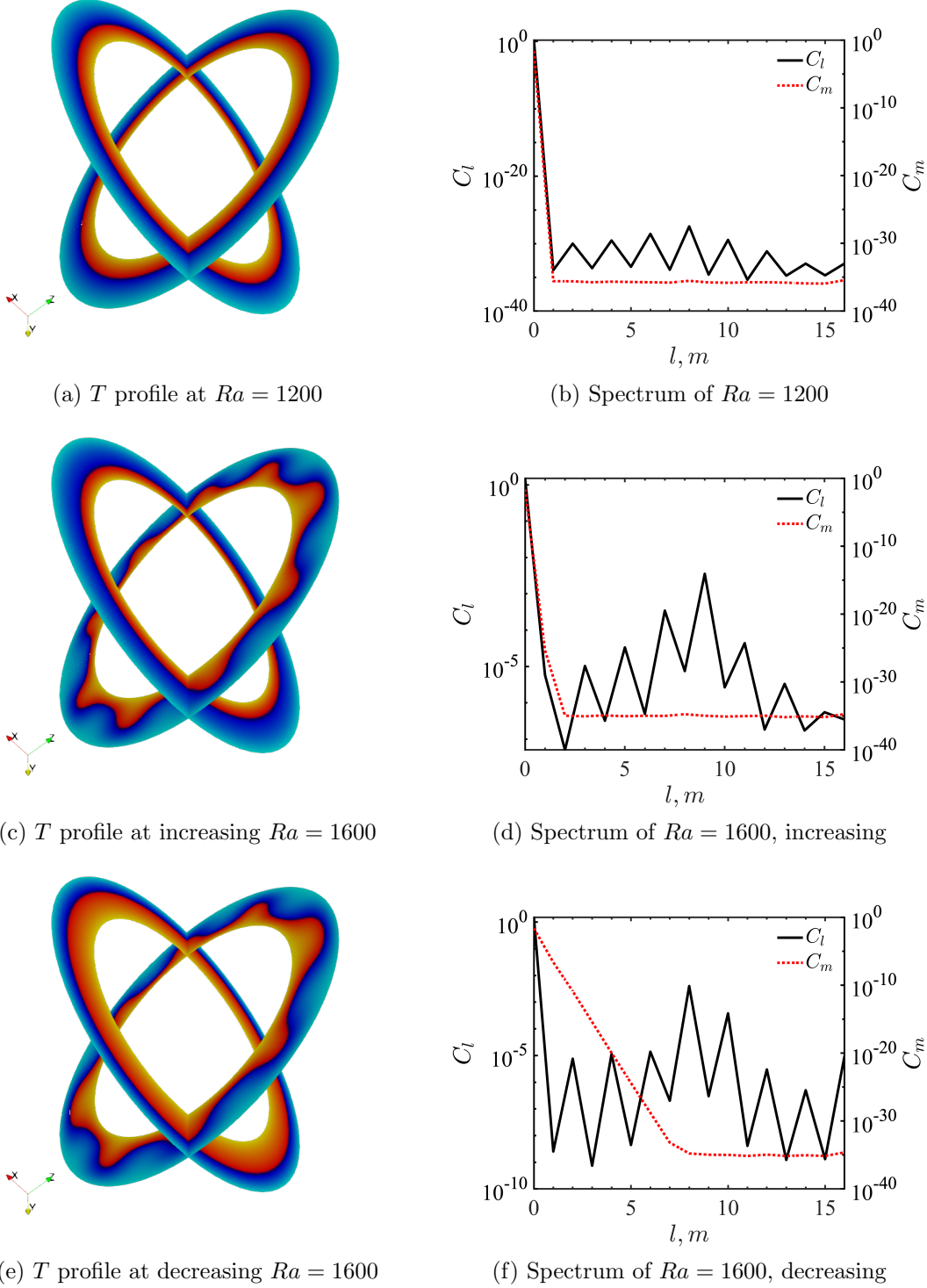


Figure 3.6: Temperature profile (a,c,e) and spherical harmonic spectrum (b,d,f) for quadratic gravity in various situations. Temperature ranges from yellow (hotter) to blue (colder). For spectra, — for  $C_l$  and reference scale on the left; ..... for  $C_m$  and reference scale on the right.

has a possibility to be non-monotonic for a different choice of  $\lambda$ , but at this value of  $\eta$  even the *most non-monotonic* case (for  $\lambda = 1.86$ ) differs from the constant gravity profile by less than 5%, so no clear effect has been observed. It might be worth to carry a deeper investigation on this subject using a different choice of  $\eta$  and  $\lambda$ . An interesting case currently under investigation is the non-monotonic mantle-like profile with parameters  $\lambda = 2.63$  and  $\eta = 0.5$ .

An important tool to understand the flow structure is represented by the analysis of the temperature profile and the corresponding spectral analysis, that for the values of  $Ra$  around the onset of convection of quadratic gravity are shown in figure 3.6 together with the relative temperature profile. Details on the spectral analysis can be found in appendix A, here we just highlight that our focus is on the non-zero value of the degree for which the relative coefficient is higher, hereby named *main-degree*. As expected, in the pure conductive case at  $Ra < Ra_c$ , the spectrum is almost zero for  $l > 0$  and  $m > 0$ . The corresponding temperature profile shows an unperturbed flow status. When convection is reached by increasing  $Ra$  over  $Ra_c$ , the system enters in a new state, hereby named state  $\mathcal{S}_9$ : the main-degree is 9 (and odd numbers dominate the  $l$  spectrum), and the temperature profile has a 9-pointed shape. Analysis of the same  $Ra$  reached from the decreasing case shows how the temperature profile has a 8-pointed shape, and the spectral analysis confirm that the main-degree is 8. This state is identified as state  $\mathcal{S}_8$ . In both cases,  $C_m$  is negligible for any  $m > 0$ .

### 3.3.2 Non-stationary convection

When  $Ra$  is further increased, a non-stationary behaviour appears. We can start by identify two different regions, characterized by increasing values in the Rayleigh number:  $Ra_1$  and  $Ra_2$ . We can define a region I for  $Ra \in [Ra_1, Ra_2)$  and a region II for  $Ra \geq Ra_2$ . In region I, the system first reaches a meta stable state  $\mathcal{S}'_9$ . Then, after a stabilising time  $t_s$  inversely proportional to  $Ra$ , it moves to a stable state  $\mathcal{S}'_8$ . In figure 3.7 we can observe the profile of Nusselt number as a function of time for a simulation with quadratic gravity at  $Ra = 1700$ , it is immediate to identify  $t_s \approx 1.2 \times 10^4$ . In figure is also shown the spectral analysis and temperature profile of this system before and after  $t_s$ . As in the previous section, we notice how state  $\mathcal{S}'_9$  has a main-degree 9, while state  $\mathcal{S}'_8$  has a main-degree 8. To verify the relationship between  $\mathcal{S}_9$ ,  $\mathcal{S}'_9$  and  $\mathcal{S}_8$ ,  $\mathcal{S}'_8$ , we analysed the evolution of a system with initial conditions in  $\mathcal{S}'_9$  (or  $\mathcal{S}'_8$ ), and we decrease  $Ra$  to  $\tilde{Ra} < Ra_1$ : the new obtained state is fully equivalent to  $\mathcal{S}_9$  (or  $\mathcal{S}_8$ ), thus we can identify  $\mathcal{S}'_9 \equiv \mathcal{S}_9$  and  $\mathcal{S}'_8 \equiv \mathcal{S}_8$ . The stability of  $\mathcal{S}_8$  has been verified by taking a system with starting condition  $\mathcal{S}_8$  and let it evolve at a different  $Ra$ : as long as  $Ra < Ra_2$ , the system will remain in state  $\mathcal{S}_8$ .

Given that  $t_s$  increases for lower values of  $Ra$ , the exact value of  $Ra_1$  is hard to identify. Currently, our simulations last at least for  $2 \times 10^5$  time units, approximately fifteen times more than the  $t_s$  identified for the current  $Ra_1$ . Our results for both  $Ra_1$  and  $Ra_2$  are schematized in table 3.4 and show the same behaviour of previous cases: results are mostly coherent once effective value has

Gravity	Quadratic	Linear	Constant	Mantle-like	Parabolic
$Ra_1$	$1650 \pm 5\%$	$2700 \pm 5\%$	$2350 \pm 5\%$	$2150 \pm 5\%$	$2900 \pm 5\%$
$Ra_1^e$	$2311 \pm 5\%$	$2313 \pm 5\%$	$2350 \pm 5\%$	$2321 \pm 5\%$	$2621 \pm 5\%$
$Ra_2$	$2100 \pm 5\%$	$3400 \pm 5\%$	$2900 \pm 5\%$	$2700 \pm 5\%$	$3600 \pm 5\%$
$Ra_2^e$	$2941 \pm 5\%$	$2914 \pm 5\%$	$2900 \pm 5\%$	$2915 \pm 5\%$	$3254 \pm 5\%$

Table 3.4:  $Ra_1$ ,  $Ra_2$  and effective value  $Ra_1^e$ ,  $Ra_2^e$  for different gravity profiles.  $Ra_{1,2}^e$  coincides for all the profiles except the parabolic.

been computed, with the parabolic case being an exception (as it was in the previous analysis).

Summarising, region I can be identified by the presence of a meta-stable flow which, after a stabilising time  $t_s$  has passed, evolves into a stable time-independent behaviour<sup>2</sup>.

When  $Ra$  is increased past  $Ra_2$  a new behaviour appears. At first, there is

<sup>2</sup>assuming it never touches region II during its evolution

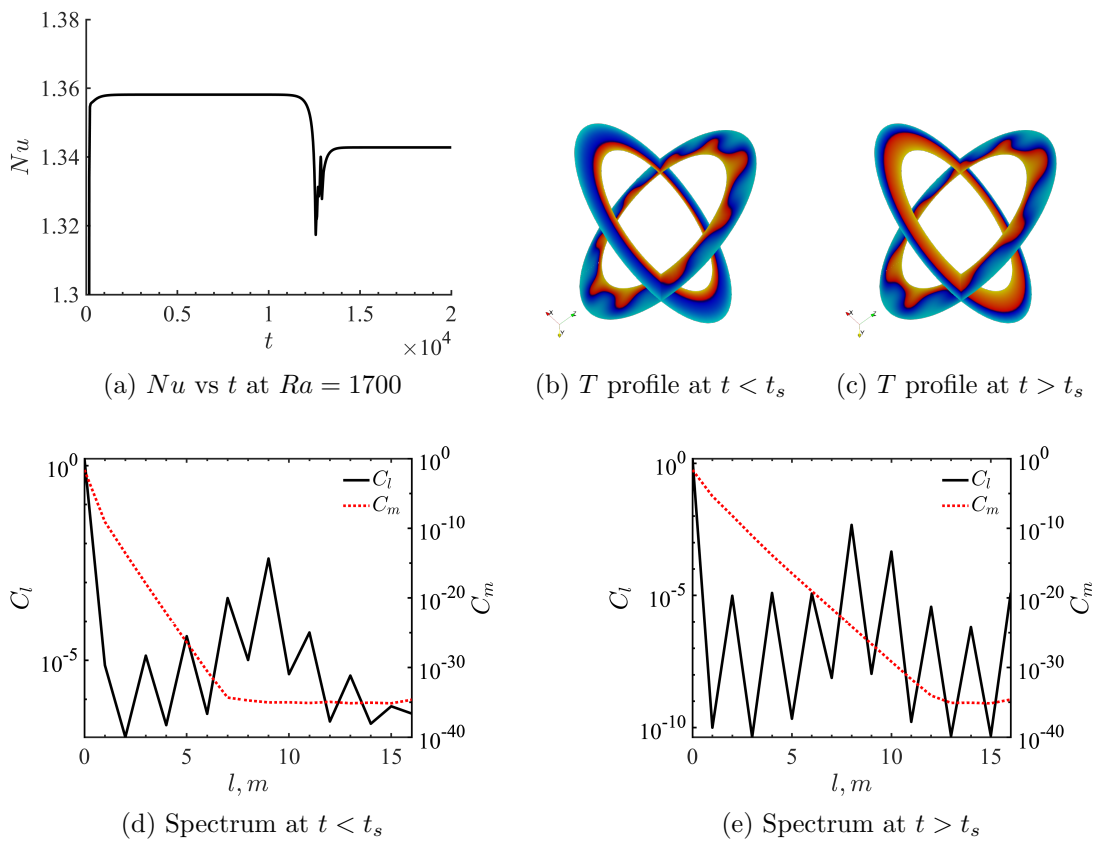


Figure 3.7: Analysis of quadratic gravity at  $Ra_1 = 1700$ . In figure (a) the time needed for stabilising is approximately  $t_s \approx 1.2 \times 10^4$ . Temperature of figures (b,c) ranges from yellow (hotter) to blue (colder). For spectra (d,e): — for  $C_l$  and reference scale on the left; ..... for  $C_m$  and reference scale on the right.

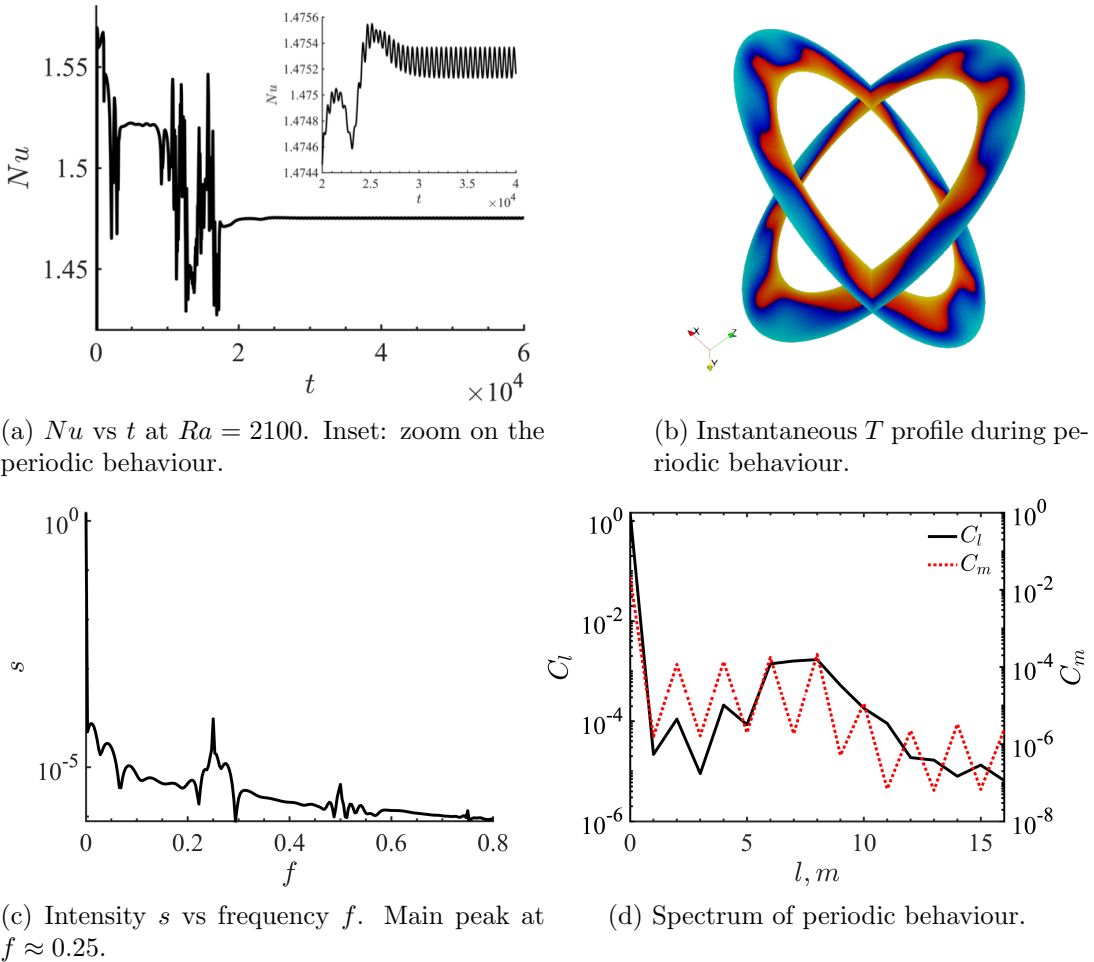


Figure 3.8: Analysis of quadratic gravity at  $Ra_2 = 2100$ . Temperature of figure (b) ranges from yellow (hotter) to blue (colder). For the harmonic spectrum (d): — for  $C_l$  and reference scale on the left; ..... for  $C_m$  and reference scale on the right.

a transitional phase where  $Nu(t)$  does not follow a predictable pattern; these oscillations are then replaced by a periodic dynamics that remains stable at any greater  $t$ . In figure 3.8 the behavior for  $Nu(t)$  at  $Ra = 2100$  for quadratic gravity is shown. In the instantaneous snapshot of the temperature profile (figure 3.8b) we can notice how plumes on the x-y plane are now significant, phenomenon also evident by looking at the spectrum profile (figure 3.8d): while  $C_l$  maintains approximately the same magnitude as lower  $Ra$  simulations (with a shift in main-degree to the range  $6 - 8$ ),  $C_m$  is now significantly greater than 0 for most of the values of  $m$  and presents the same alternating structure that characterised  $C_l$  before. In figure 3.8c the Fourier transformation of the oscillatory evolution is shown (for further details, see Appendix A): two main frequencies can be highlighted,  $f = 0.25$  and  $f = 0.5$ .

Further increases of  $Ra$  reduce the transitional period and introduce new frequencies in the spectrum; In figure 3.9, the case for  $Ra = 5000$  for quadratic gravity shows that the harmonic spectrum has magnitude closer to  $\mathcal{O}(1)$  for both  $C_l$  and  $C_m$ , with a main-degree at 5, and the frequency spectrum shows several peaks. At higher values of  $Ra$ , periodicity disappears and a chaotic behaviour is obtained: here the frequency spectrum is almost continue. Surprisingly, the main-degree remains stable around  $l = 5$  instead of following the previous behaviour of shifting towards lower numbers for higher values of  $Ra$ .  $C_m$  remains highly excited for a large range of  $m$ .

Region II is then defined as the region for which the system presents a time-dependent behaviour at any time  $t$ . This behaviour may be periodic when  $Ra$  is very close to  $Ra_2$ , or almost chaotic when  $Ra$  is much higher.

### 3.3.3 Hysteresis

As anticipated in previous sections, the behaviour of the system varies accordingly to the starting conditions. From current analysis, we identified two main time-independent states,  $\mathcal{S}_9$  and  $\mathcal{S}_8$ . In figure 3.10a, we compared the convection efficiency of heat transfer for two different simulations: an increasing case starting from the onset of convection, and a decreasing case starting in region I and with enough time to reach state  $\mathcal{S}_8$ . Results show that the second case has as a worse efficiency (in terms of a smaller value of  $Nu$ ): an explanation for this effect can be found in the temperature profile, which for the  $\mathcal{S}_8$  state has less protrusions between the two shells and thus a reduced heat transfer. At the present moment, however, it is unclear why the system prefers a configuration with a less efficient heat transfer. It is worth noticing that using increasing or decreasing simulations is just a matter of convenience: as long as the initial conditions of the system are in state  $\mathcal{S}_9$  and the system does not evolve in  $Ra > Ra_1$ , the dynamic is fully equivalent to the increasing case with initial conditions at  $Ra_c$ .

A similar result is obtained when looking at the time dependent behaviour of  $Ra \geq Ra_2$ . Figure 3.10b shows the behaviour of the simulations under three different conditions: an evolution in region II at  $Ra_2$  (we name it *region II state*), and two evolutions at  $\bar{Ra} = 2000 < Ra_2$  differentiated by their initial conditions. One simulation is done at initial conditions  $\bar{Ra}$  (*rest state*), the other starts from the periodic oscillations of the region II simulation, i.e. initial conditions  $Ra_2$  (*oscillating state*). This latter simulation keeps in its evolution the periodic pattern typical of higher values of  $Ra$ . Its spectrum is qualitatively identical to the spectrum of the *region II state*, as shown by comparing figures 3.10f and 3.8d, and the same holds true for the temperature profile, showed in figures 3.10d and 3.8b. On the other side, the spectrum and temperature profile of the *rest state* (not shown here) is qualitatively equivalent to any other fluid evolved completely in region I. The periodic oscillations remain a feature of the system even when  $Ra$  is further decreased, but their effect on  $Nu$  becomes progressively smaller and it is negligible when  $Ra \lesssim Ra_1$ , as shown by figure 3.10c: the difference between

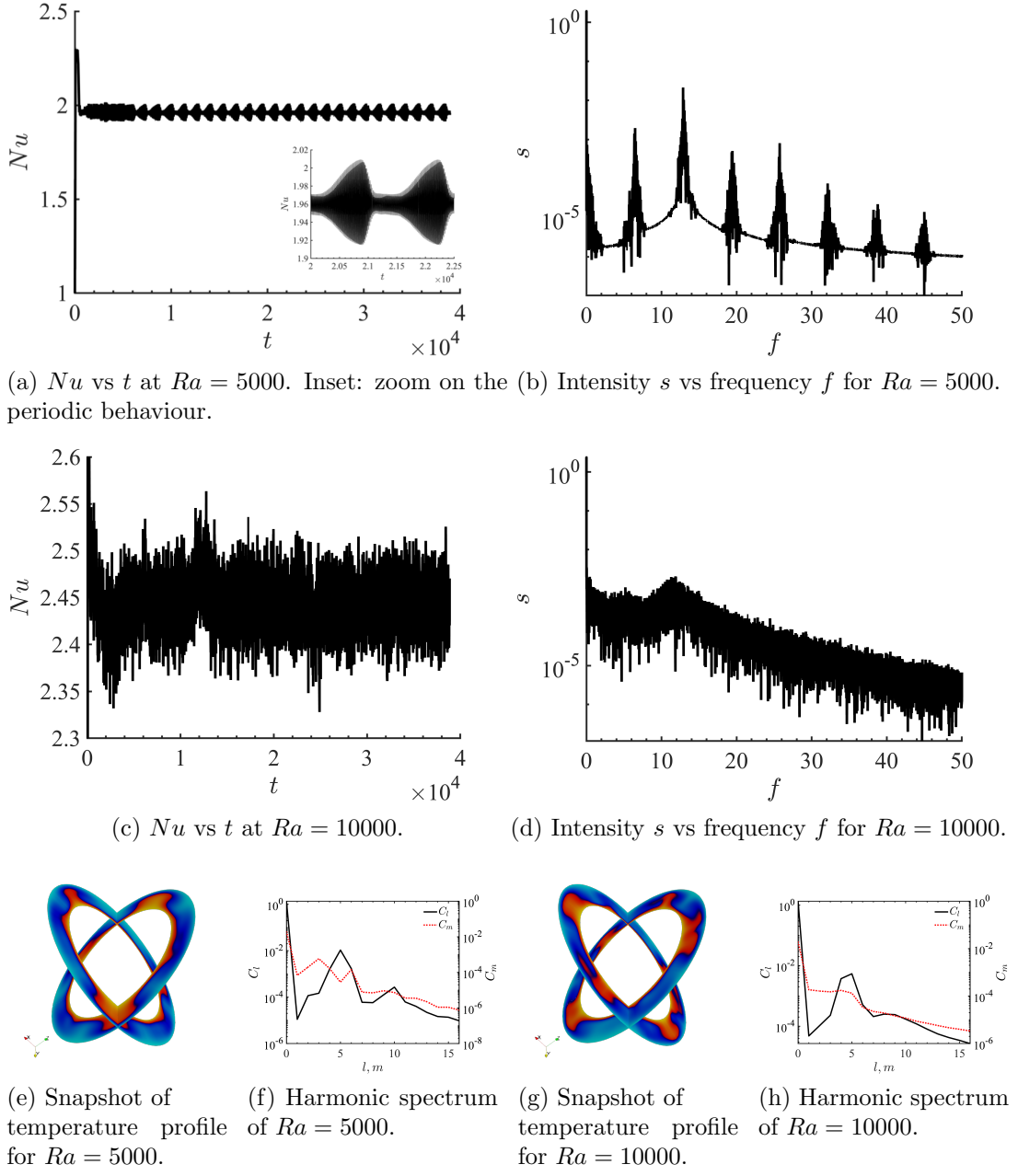


Figure 3.9: Analysis of quadratic gravity at  $Ra = 5000$  (a,b,e,f) and  $Ra = 10000$  (c,d,g,h). Temperature of figures (e,g) ranges from yellow (hotter) to blue (colder). For the harmonic spectra (f,h): — for  $C_l$  and reference scale on the left; -·- for  $C_m$  and reference scale on the right.

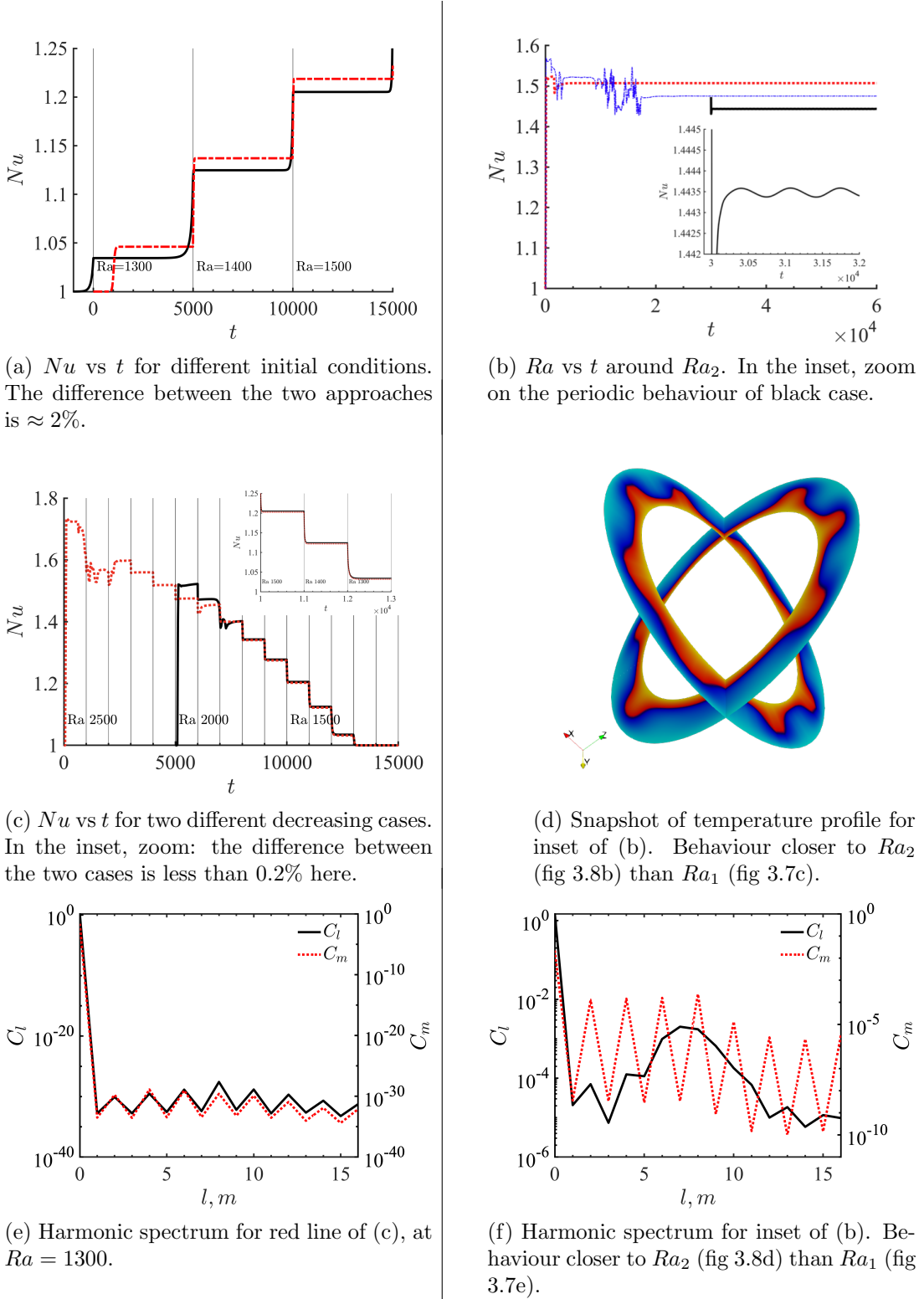


Figure 3.10: On the left, comparisons for different initial conditions (vertical black lines in (a,c) indicate changes in  $Ra$ ); on the right, behaviour around  $Ra_2$ . (a): — decreasing case (with reversed time scale) starting from  $Ra > Ra_1$ ; ..... increasing case starting from  $Ra_c$ . (b): — oscillating state; ..... rest state; — region II state. (c): — decreasing case starting at  $Ra < Ra_2$ ; ..... decreasing case starting at  $Ra > Ra_2$ . Temperature of figure (d) ranges from yellow (hotter) to blue (colder). For the harmonic spectra (e,f): — for  $C_l$  and reference scale on the left; ..... for  $C_m$  and reference scale on the right.

two evolutions with decreasing  $Ra$  is large at the beginning, but becomes almost zero when  $Ra$  approaches  $Ra_c$ . Even if the effect on heat transfer is negligible, the system keeps memory of its initial conditions in the spectrum: in a simulation with oscillating initial conditions the spectrum has a non zero value of  $C_m$  even for very low  $Ra$ , being 5 orders of magnitude bigger in figure 3.10e than the comparable simulation at  $Ra \approx Ra_c$  of figure 3.6b.

While in general we expect to see  $Nu(Ra = x) > Nu(Ra = y)$  when  $x > y$ , we can notice that in our simulations this order is not respected when comparing  $Nu(Ra = Ra_2)$  and  $Nu(Ra = \bar{Ra}_{rest})$  (figure 3.10b). As previously noted, the rise of a periodic oscillation and the change in the spectrum are correlated to a worse heat transfer, this motivates the inversion in  $Nu$ . Indeed, when comparing the two oscillating solutions, we restored the expected order:  $Nu(Ra = Ra_2) > Nu(Ra = \bar{Ra}_{oscillating})$ .

The strong dependence on the initial conditions seem to be an intrinsic property of the system that does not depend on the gravity profile chosen: tests have been run for all the other profiles and, as already shown by table 3.4, the existence of those regions is not affected by the chosen gravity.

### 3.3.4 Higher $Pr$ Number

As anticipated in the introduction of this chapter, the same configurations previously analysed have been studied also for water, characterised by  $Pr_{water} = 7.1 = 10Pr_{air}$ . Looking at equation (3.1), we notice how the main direct effect of a variation in Prandtl number is a larger coefficient in front of  $\nabla^2\mathbf{u}$ , i.e. the viscous effects are stronger for water compared to air. So, for inertial terms to overcome viscosity, an higher  $Ra$  is needed. Since  $Pr_{water}/Pr_{air} = 10$ , we expect  $Ra_{water}$  to be 10 times bigger to obtain the same time-dependent behaviours, while the critical value for the onset of convection will be unaffected by the change of  $Pr$ .

The system has been tested for different grids, and the same grid used for simulations at lower  $Pr$  has been found to be accurate:  $\{N_\theta = 65, N_r = 69, N_\phi = 69\}$ . The *increasing / decreasing* approach has been tried for this value of  $Pr$ , but it has been found rather ineffective due to the much larger time needed to reach a stable state, especially for the *increasing* case, thus the study has been done by running several simulations, each at a (different) fixed  $Ra$ . In most of the simulations the fluid is started from rest, but to analyse hysteresis and for longer simulations sometimes an old state has been used as starting condition for the new run.

Using  $\mathbf{g}^q$  as gravity profile the onset of convection, computed as before by the analysis of the Nusselt number, happens at the same value of  $Ra_c \approx 1250$ , equivalent to an effective value of  $Ra_c^e = 1750$ . This result, in line with the predictions, shows that the onset of convection has no direct dependence on the value of  $Pr$ . When  $Ra$  is much higher than  $Ra_c$ , we observe again the time dependent behaviour of region II appearing at  $Ra_{2,water} \approx 21000$ , that respects our prediction of  $Ra_{2,water} = 10Ra_{2,air}$ .

In the region I between the onset of convection and the time dependent be-

	$Ra_{S_9}$	$Ra_{S_8}$	$Ra_{S_7}$	$Ra_{S_6}$	$Ra_{S_5}$	$Ra_2$
$Ra^q$	1250	4000	6000	11000	16000	21000
$Ra^e$	1740	5550	8350	15300	22300	29000

Table 3.5: Values of  $Ra$  for the first occurrence of different states when  $Pr = 7.1$  for quadratic gravity on the first line, and effective value on the second line.  $Ra_{S_9}$  is equivalent to  $Ra_c$  and  $Ra_{S_8}$  is equivalent to  $Ra_1$ . Confidence interval at  $\pm 5\%$  for  $Ra_c$  and  $Ra_2$ ,  $\pm 10\%$  for the others.

haviour, a series of different regimes appear. Looking at the spectrum, we find the same configuration found for air, with a state  $S_9$  having a spectrum peaked at  $C_l = 9$ . This state is stable for a much larger range of  $Ra$  compared to air but eventually, as  $Ra \approx 4000 = Ra_1$ , the system jumps to a new equilibrium state  $S_8$ , with a spectrum peaked at  $C_l = 8$ . In the same fashion as air, decreasing  $Ra$  from a system in  $S_8$  does not bring it back to  $S_9$ : hysteresis is present also for water. Compared to air simulations, however, the system has a larger space to explore in  $Ra$  before reaching region II at  $Ra_2$ . This leads to the appearance of new states in the meta-stable region I, we identify them as  $S_7$ ,  $S_6$  and  $S_5$  for systems with main-degree 7,6 and 5 respectively. A summary of the first measured  $Ra$  for each state is given in table 3.5. As happened for air, when the main peak is an odd/even number then all the odd/even degrees are peaked as well.

Increasing  $Ra$  above  $Ra_2$  brings back the same periodic oscillation observed for region II of air, with the harmonic spectrum keeping its peak at  $l \approx 5$  and the rise of more and more characteristic frequencies. Surprisingly, the state  $S_5$  appears to be the most stable both for water (which reaches it after exploring all the states from 9 to 5 in region I) and for air (which reaches it only in region II). Eventually, for  $Ra$  high enough, the frequency spectrum becomes continuum and the system moves toward a turbulent state.

### 3.4 Concluding remarks

In this chapter, a characterization of Rayleigh-Bénard convection for fluids between spherical shells has been carried out using the second order finite difference scheme described in the previous chapter. By setting fixed temperature at the shells and fixed radius ratio, we can explore different configurations by varying Prandtl number, Rayleigh number, and the radial gravity profile.

The analysis for air at  $Pr_{air} = 0.71$  shows that the critical Rayleigh number for the onset of convection is heavily dependent on the gravity profile chosen. However, this dependence can be reabsorbed introducing a new quantity  $Ra^e$  which renormalises the Rayleigh number by including the radial average of the gravity. Thus, the onset of convection occurs at an effective Rayleigh number  $Ra^e \approx 1730$  independently of the gravity profile considered, allowing us to use a smaller parameter space. This renormalisation does not hold true for the artificial parabolic gravity profile created on purpose heavily asymmetrical and non-monotonic. Further studies with a non-artificial mantle-like gravity profile

with a precise choice of parameters are currently ongoing to understand if the failure in the renormalisation is due to the non-monotonicity of the profile. The same analysis has been done for water ( $Pr_{water} = 7.1$ ), and as expected the onset of convection is mostly unaffected by the higher Prandtl number, being at  $Ra^e \approx 1750$ .

The effective Rayleigh number can also be used to identify all the subsequent states the system explores. Our criterion for the characterization of different states is given by the analysis of the spherical harmonics of the system. At the onset of convection, the system has a harmonic spectrum peaked at degree  $l = 9$ , so we identify this state as  $\mathcal{S}_9$ . Increasing  $Ra$  leads to the rise of new situations. For air, we first identify a region I (for  $Ra^e \geq Ra_1^e = 2350$ ) where the state  $\mathcal{S}_9$  becomes unstable and the system, given enough time, moves to a new configuration  $\mathcal{S}_8$  where the main-degree of the harmonic spectrum is  $l = 8$  ( $C_m$  remains unexcited in this region). Region I for water starts at a higher Rayleigh number ( $Ra_1^e \approx 5550$ ) but the system remains in this region for a larger interval of  $Ra$ , so while both fluids start from state  $\mathcal{S}_9$  and reach state  $\mathcal{S}_8$ , increasing  $Ra$  for water leads to the emergence of new states  $\mathcal{S}_7$ ,  $\mathcal{S}_6$  and  $\mathcal{S}_5$  where the main-degree is, respectively, 7, 6 and 5.

When  $Ra$  is increased beyond a threshold  $Ra_2$ , the system enters region II, where a time-dependent behaviour is observed. Being this behaviour heavily influenced by  $Pr$ , we expect  $Ra_{2,water}$  to be about 10 times bigger than  $Ra_{2,air}$ ; indeed we have  $Ra_{2,air}^e = 2900$  and  $Ra_{2,water}^e = 29000$ . In this region, the harmonic spectrum has main-degree  $l = 5$  for both water and air and for any value of  $Ra$ , while the values of  $C_m$  become progressively larger. In this region the analysis of the frequency spectrum can give interesting information. For  $Ra$  close to  $Ra_2$ , only few frequencies are excited and a clearly periodic behaviour can be observed in the flow dynamic. Increasing  $Ra$  leads to new peaks in the frequency spectrum and eventually a continuum spectrum is attained at very high values of  $Ra$ , while the periodicity in the dynamic disappears.

We observed that, for both water and air, lower degree states are stable, and decreasing  $Ra$  to previously explored values does not bring back the higher-degree configurations. Moreover, we discovered that lower  $l$  is associated with a reduced heat transfer and thus a lower value of  $Nu$ . We also noted that, if the system explored region II during its evolution, time dependent features remain part of the dynamic even when  $Ra$  is lowered, and  $C_m$  remains excited even for values of  $Ra$  very close to the onset of convection. Based on these observations, we can claim that the system present hysteresis and its heat transfer is heavily dependent on its starting conditions.

Having a characterization of the fluid in a spherical geometry under Rayleigh-Bénard convection, in the next chapter we will focus on the effect that a gravity center shifted from the sphere center may cause in the dynamic. The inspiration for this study comes from the knowledge that the Earth presents a small inhomogeneity in its structure, leading to a shift of the mass center from one hemisphere to the other.

## CHAPTER 4

# Off-center gravity induces large-scale flow patterns in spherical Rayleigh-Bénard\*

### 4.1 *Introduction*

The hemispherical asymmetry is a prominent feature of the Earth's inner core [107, 6, 61]. [61] demonstrated that the mantle extracts heat from the inner core of the Earth at a spatially non-uniform rate. Such a non-uniform heat flux in the mantle is relevant to the abrupt changes in tectonic plates movement, the creation of new plate margins, and volcanic activities [128]. A possible reason for hemispherical asymmetry is mentioned by [107], where it is shown that crystallization on the denser hemisphere and melting on the opposite side can amplify the density heterogeneity, leading to the off-center of gravity towards the crystallizing side [6]. However, how the position of the center of gravity influences the flow structures and the heat fluxes in the thermal convection within the Earth's core remains an open question, and quantification on such the effect is needed.

Spherical Rayleigh-Bénard convection is a simplified system to examine the effect of the center of gravity offset in turbulent thermal convection. It consists of a fluid layer enclosed by two spherical shells, heated from the inner sphere, and cooled from the outer sphere with radial gravity pointing towards the gravity center.

Besides the idealized system, there is a large community considering additional features in the spherical system to better model geophysical and astrophysical settings, such as mobile surface plates [118, 94, 111], rapid rotation [10, 50, 97], magnetic field [166], and temperature-dependent viscosity [171]. An important finding is the existence of large-scale flows in the spherical system. For instance, with the movement of lithospheric plates to study the mantle convection, large-scale flow exists in the mantle to balance the mass flux of moving lithospheric plates [118, 94]. To consider planetary magnetic fields, dynamo models are in-

---

\*Based on G. Wang, L. Santelli, R. Verzicco, D. Lohse, R. J. A. M. Stevens, *Off-center gravity induces large-scale flow patterns in spherical Rayleigh-Bénard*, under revision from Journal of Fluid Mechanics, preprint arXiv:2105.03623 [physics.flu-dyn]

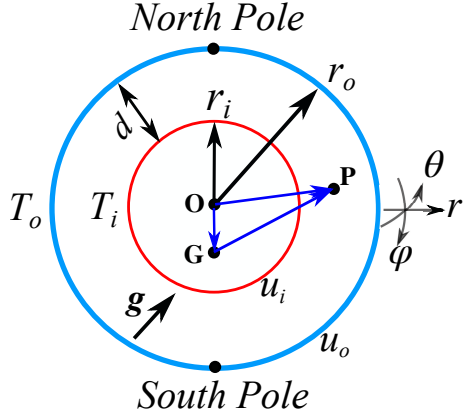


Figure 4.1: Schematic of spherical Rayleigh-Bénard convection in between two concentric spheres with radius ratio  $\eta = r_i/r_o$  between the inner and outer sphere and gap size  $d = r_o - r_i$ . A no-slip boundary condition with constant temperature is used on the inner and outer sphere. In spherical coordinates the longitudinal, co-latitudinal, and radial directions are represented by  $\hat{\theta}$ ,  $\hat{\varphi}$  and  $\hat{r}$ , respectively.  $G$  indicates the gravity center, which is offset from the geometric center  $O$ , and point  $P$  indicates an arbitrary fluid parcel.

cluded to study the convection in the Earth's core or solar convection, e.g. [25] and [108] show the presence of large-scale meridional circulation in the Earth's outer core and Sun, respectively. Besides, temperature-dependent viscosity also holds an important role. Long-wavelength structures can be produced even in the absence of surface plates [171]. Although previous studies had considered different types of complications, the hemispherical asymmetry effect on the existence of large-scale structures has so far been overlooked.

In this chapter, we investigate the effect of the gravity center location on the flow structures and heat transfer in spherical Rayleigh-Bénard convection. We present three-dimensional direct numerical simulations for  $Pr = 1$  using a fixed aspect ratio  $\eta = 0.3$ , which represents Earth's outer core.

## 4.2 Numerical method and parameters

The spherical Rayleigh-Bénard geometry is illustrated schematically in figure 4.1. Fluid fills a spherical shell between the inner sphere with radius  $r_i$  and the outer sphere with radius  $r_o$ . The radius ratio between the inner and the outer sphere is given by

$$\eta = r_i/r_o. \quad (4.1)$$

The temperature of the inner and outer spheres is kept constant at  $T_i$  and  $T_o$ , respectively, with  $T_i > T_o$ , and no-slip boundary conditions are used on both spheres. Point  $G$  indicates the gravity center, which is offset from the geometrical origin

is defined as follows:

$$\varepsilon = |\mathbf{OG}|/r_i, \quad (4.2)$$

where  $|\mathbf{OG}|$  indicates the displacement of the gravity compared to the geometrical center.

The dynamics of spherical Rayleigh-Bénard convection are controlled by the Rayleigh number and the Prandtl number

$$Ra = \frac{\alpha g_o \Delta T d^3}{\kappa \nu}, \quad Pr = \frac{\nu}{\kappa}, \quad (4.3)$$

where  $\alpha$  is the thermal expansion coefficient,  $g_o$  is the gravity on the outer sphere,  $\nu$  is the viscosity, and  $\kappa$  is the thermal diffusivity. We normalize the results by the length scale  $d = r_o - r_i$ , the temperature difference  $\Delta T$  between the inner and outer sphere, and the free-fall velocity  $U = \sqrt{\beta g_o \Delta T d}$ .

#### 4.2.1 Numerical method

Once again we solve the Navier-Stokes equations under the Boussinesq approximation in spherical coordinates, which is rewritten here for convenience:

$$\frac{\partial \mathbf{u}}{\partial t} + \mathbf{u} \cdot \nabla \mathbf{u} = -\nabla p + \sqrt{\frac{Pr}{Ra}} \nabla^2 \mathbf{u} + C_{g,i} g T \hat{e}_i, \quad \nabla \cdot \mathbf{u} = 0, \quad (4.4)$$

$$\frac{\partial T}{\partial t} + \mathbf{u} \cdot \nabla T = \frac{1}{\sqrt{RaPr}} \nabla^2 T. \quad (4.5)$$

where  $\mathbf{u}$ ,  $p$ ,  $T$ , and  $g$  denote the fluid velocity, pressure, temperature, and gravitational acceleration acting in the three directions, respectively.  $\hat{e}_i$  is the unit vector in which  $i = 1, 2, 3$  correspond to the  $\hat{\theta}$ ,  $\hat{r}$ , and  $\hat{\phi}$  directions respectively. The coefficients  $C_{g,i}$  denote the decomposition of  $g$ , which is detailed in the appendix B. We consider the following gravity profile

$$g = (L_{GP}/r_o)^{n_g}, \quad (4.6)$$

in which  $L_{GP} = |\mathbf{GP}|$  indicates the distance between a fluid point and the geometrical center, see figure 4.1, and we use  $n_g = -2, -1, 0$  and  $1$ . The value of  $n_g$  can be inferred by physical considerations on the mass ratio between the nucleus ( $r < r_i$ ) and the spherical shell ( $r_i < r < r_o$ ). The gravity is constant ( $n_g = 0$ ) when the mass of the spherical shell is negligible. This assumption is typically used to model the Earth's mantle [16]. If the mass is concentrated in the nucleus, one obtains  $n_g = -2$ . [32] showed that, only for this gravity distribution function, there is an analytical relation between the viscous dissipation rate and the Nusselt number ( $Nu$ ). If the density is constant within the fluid layer, and no mass is contained in the inner sphere, gravity is directly proportional to the radial coordinate  $r$  ( $n_g = 1$ ) [153]. For the sake of completeness,  $n_g = -1$  is also included.

$G(\theta, r, \varphi)$	$Nu$	$Re_{rms}$
$O$	3.42	44.1
$(0, r_i/2, \pi/2)$	3.197	40.8
$(\pi/2, r_i/2, \pi/2)$	3.187	40.8
$(0, r_i/2, 0)$	3.191	41.1
$(\pi/4, r_i/2, \pi/4)$	3.182	40.9
$(\pi/7, r_i/2, 3\pi/5)$	3.186	41.0

Table 4.1: Parameters of the spherical RB simulations with  $Pr = 1$ ,  $Ra = 3 \times 10^4$ ,  $n_g = -2$  and  $\eta = 0.6$ .  $G(\theta, r, \varphi)$  is the gravity center location.  $N_{\theta, r, \varphi} = (129, 49, 97)$  indicates the number of grid points in the longitudinal, radial, and co-latitudinal direction, respectively. The last five simulations are used to verify that the coefficients  $C_{g,i}$ , see Eq. (B.6), are correctly implemented by putting the gravity center  $G$  in five different locations with the same  $L_{OG}$ , see figure 4.1.

The governing equations (4.4–4.5) are discretized using the approach described in chapter 2. The code has been validated carefully by [124], and we refer to that work for details on the method. In chapter 3 additional validation results relevant to the flows considered here are reported. To ensure that the off-center gravity is implemented correctly, we verified that the flow dynamics for the same  $L_{OG}$ , see figure 4.1, are identical for five different gravity center locations. The last five lines of table 4.1 confirm that both  $Nu$  and  $Re_{rms}$  (volume averaged  $Re$ , see eq. (4.8)) obtained from these simulations are consistent.

#### 4.2.2 Considered parameter regime

To study the effect of the gravity center location on the flow dynamics in spherical Rayleigh-Bénard convection we considered different gravity distributions ( $n_g \in \{-2, -1, 0, 1\}$ ) in equation (4.4) and equation (4.6) for  $Ra = 7 \times 10^6$  and  $3 \times 10^7$ . All simulations in this study are for  $Pr = 1$ . To vary  $\varepsilon$  we move the gravity center from the geometric center to the South Pole. The considered cases are summarized in table 4.2.

To ensure that the flow is fully resolved, we place a sufficient number of computational grid points in the bulk [144]. As we will use spectral analysis to analyze the flow structures, we use a uniform grid in the longitudinal and co-latitudinal directions. In the radial direction, the grid cells are clustered towards the inner and outer sphere to ensure the boundary layers are adequately resolved [136]. We note that a strong convective jet towards the North Pole is generated when  $\varepsilon > 0$ , while the flow around the equator is less turbulent than for the case with  $\varepsilon = 0$ , see the visualizations in figure 4.2(b-f). As the computational grid cells around the equator are the largest, this allows us to use a somewhat coarser mesh for the simulations in which the gravity center is displaced from the geometrical center.

We calculate the  $Nu$  number from the normalized averaged temperature gradients at the inner and outer sphere as in equation (2.19). The difference in the  $Nu$  number obtained at the inner and outer sphere is always less than 0.2%.

Besides, we verify that the  $Nu$  number calculated at the spheres is equivalent to the value obtained from  $Nu_h(r)$

$$Nu_h(r) = \frac{\langle u_r T \rangle_s - \kappa \partial_r \langle T \rangle_s}{-\kappa \partial_r T_c}, \quad (4.7)$$

where  $T_c(r) = \eta/[(1-\eta)^2 r] - \eta/(1-\eta)$  is the conductive temperature profile for constant temperature boundary conditions and  $\langle \dots \rangle_s$  represents the average over a spherical surface. The time-averaged ( $\dots$ ) and volume-averaged ( $\langle \dots \rangle$ ) root mean square (rms) Reynolds number is given by

$$Re_{rms} = \sqrt{\left\langle \sum_{i=1}^3 u_i u_i \right\rangle}. \quad (4.8)$$

The details of the simulations considered in this study are summarized in table 4.2.

## 4.3 Results

### 4.3.1 Generation of convective jet and large-scale circulation

We first examine how the flow structures respond to the gravity center offset as shown in figure 4.2(a). When the gravity center is located in the geometrical center ( $\varepsilon = 0$ ), there are uniformly distributed long and thin sheet-like thermal structures generated at the inner sphere. With a little offset of the gravity center ( $\varepsilon = 0.1$ ), figure 4.2(b) indicates the asymmetric flow pattern where the hot plumes preferentially emit near the North Pole. With an even larger gravity center offset (increasing  $\varepsilon$  to 0.8), there is the formation of energetic jets near the North Pole, as shown in figures 4.2(c-f). The largely asymmetric flow pattern can be further confirmed by the azimuthally averaged temperature field in a meridian cut, as shown in figure 4.3(a). The convective jet is clearly shown in the upper hemisphere, and the number of plumes traveling from the inner to the outer sphere is reduced in the lower hemisphere (see also figure 4.2(f)).

To understand the generation of the convective jet, we decompose the gravity  $\mathbf{g}$  vector into  $\mathbf{g}_{PO}$  and  $\mathbf{g}_{PO,\perp}$ , i.e.

$$\mathbf{g} = \mathbf{g}_{PO} + \mathbf{g}_{PO,\perp} \quad (4.9)$$

Figure 4.3(c) shows that the buoyancy force component  $\mathbf{g}_{PO}$  points towards the geometric center  $\mathbf{O}$ , while the other component  $\mathbf{g}_{PO,\perp}$  works in the co-latitudinal direction. and it is the term inducting a flow in that direction. When  $\mathbf{g}_{PO,\perp} = 0$ , i.e. the gravity center  $\mathbf{G}$  coincides with the geometrical counterpart  $\mathbf{O}$  ( $\varepsilon = 0$ ) the flow is homogeneous in the lateral directions. However, when the gravity

Table 4.2: Details of the simulations. The columns from left to right indicate:  $Ra$ , the gravity profile exponent  $n_g$  (see equation (4.6)), the number of grid points in the longitudinal, radial, and co-latitudinal direction  $N_\theta \times N_r \times N_\phi$ , the shift of the gravity center with respect to the geometrical center  $\varepsilon$  (see equation (4.1)), the average heat transfer across the inner and outer sphere (see equation (2.19))  $Nu$ ,  $\langle Nu_h(r) \rangle_r = \int_{r_i}^{r_o} Nu_h(r) dr$  (see equation (4.7)), and  $Re_{rms}$  (see equation (4.8)).

$Ra$	$n_g$	$N_\theta \times N_r \times N_\phi$	$\varepsilon$	$Nu$	$\langle Nu_h \rangle_r$	$Re_{rms}$
$7 \times 10^6$	1	$181 \times 73 \times 181$	0	6.415	6.404	282.2
		$145 \times 73 \times 145$	0.1	6.307	6.292	283.8
			0.2	6.337	6.339	286.4
			0.4	6.429	6.421	284.9
			0.6	6.497	6.495	280.9
			0.8	6.476	6.473	250.5
$7 \times 10^6$	0	$181 \times 73 \times 181$	0	8.189	8.171	377.5
		$145 \times 73 \times 145$	0.05	8.185	8.187	369.7
			0.1	8.167	8.158	376.2
			0.2	8.133	8.129	384.3
			0.4	8.198	8.174	386.9
			0.6	8.071	8.077	363.7
			0.8	7.964	7.952	315.7
$7 \times 10^6$	-1	$181 \times 73 \times 181$	0	11.30	11.28	513.7
		$145 \times 73 \times 145$	0.4	11.09	11.08	538.7
			0.8	10.23	10.22	433.1
$7 \times 10^6$	-2	$201 \times 93 \times 201$	0	16.05	16.12	782.7
		$145 \times 93 \times 145$	0.4	16.27	16.34	808.7
			0.8	15.49	15.35	781.2
$3 \times 10^7$	1	$257 \times 93 \times 257$	0	9.394	9.413	592.0
		$251 \times 93 \times 163$	0.05	9.292	9.306	592.2
			0.1	9.349	9.297	599.9
			0.2	9.264	9.244	597.2
			0.4	9.362	9.327	587.7
			0.6	9.436	9.427	576.9
			0.8	9.242	9.238	532.3
$3 \times 10^7$	0	$257 \times 93 \times 257$	0	12.40	12.41	777.2
		$251 \times 93 \times 163$	0.05	12.33	12.35	795.2
			0.1	12.31	12.26	806.5
			0.2	12.29	12.33	795.6
			0.4	12.25	12.23	799.0
			0.6	11.90	11.93	752.3
			0.8	11.58	11.44	630.9

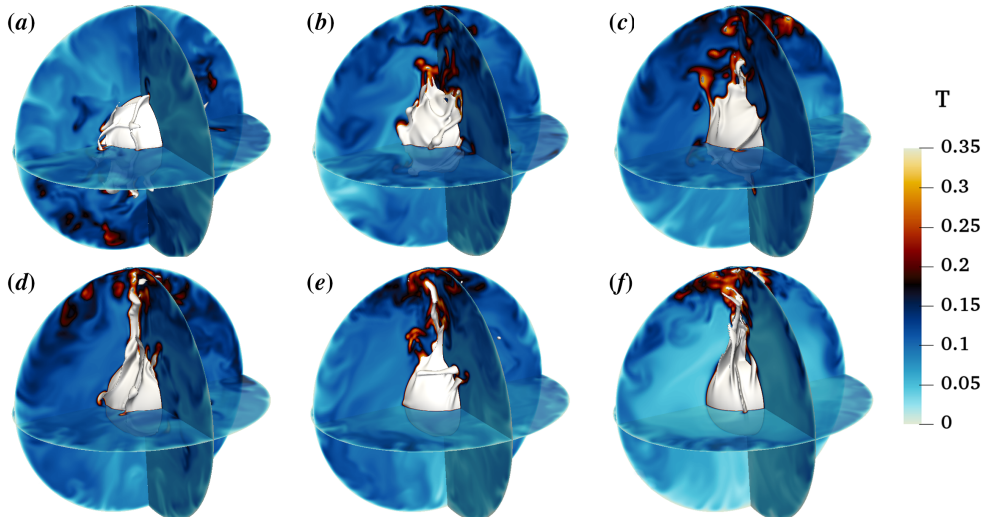


Figure 4.2: The temperature isosurface for  $T = 0.3$  is indicated in white, while the color indicates the temperature field in the equatorial plane and two meridian cuts for  $Ra = 3 \times 10^7$  and  $n_g = 0$ . (a-f) correspond to  $\epsilon = 0, 0.1, 0.2, 0.4, 0.6$  and 0.8, respectively.

center  $\mathbf{G}$  is displaced to the South ( $\epsilon > 0$ ), the buoyancy force component  $\mathbf{g}_{\text{po},\perp}$  drives ascending hot thermal plumes along the surface of the inner sphere, accumulating near the North Pole and emitting towards the outer surface, see figure 4.3(b). As a result, hot thermal plumes accumulate near the North Pole of the inner surface where the convective jet from the inner to the outer sphere is formed. Subsequently, the thermal plumes from the jet descend along the outer surface to form a strong meridional circulation, which is oriented in the zonal direction in the Northern hemisphere. A limited number of plumes continue to travel along the outer sphere. When these plumes reach the South Pole on the cold outer surface, they form a jet towards the hot inner surface to generate a weak meridional circulation in the Southern hemisphere.

#### 4.3.2 Modal analysis to identify large-scale structures

With shifting of the gravity center, the intensity of the turbulent kinetic energy (TKE) slightly increases ( $\epsilon \leq 0.4$ ) then considerably decreases ( $\epsilon \geq 0.6$ ) as shown in figure 4.4(a). To identify the TKE in the large-scale structures due to off-center of gravity, we perform the modal analysis of the flow field. In spherical coordinates, a surface spherical harmonic function in equation (A.4) is the expansion of plane waves, where the order  $m$  represents the wavenumber on the longitudinal directions. The radial integrated and temporal averaged power spectrum  $C_m$  is calculated based on equation (A.7).

When the gravity center is at the geometric counterpart ( $\epsilon = 0$ ), the flow is homogeneous in the co-latitudinal direction. The TKE transfers from large to small scales, as shown in figure 4.4(b). Once the gravity center is not at the

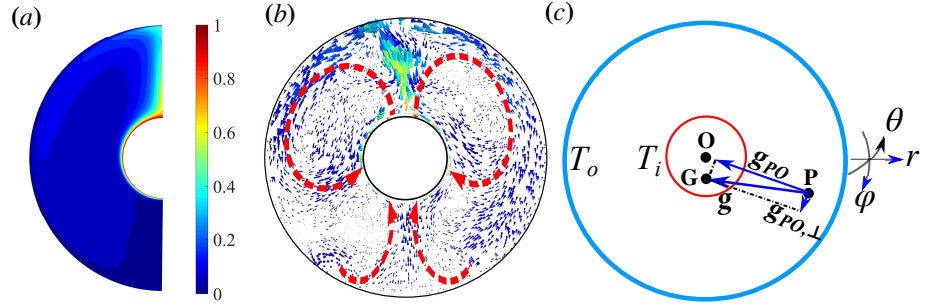


Figure 4.3: (a) Mean temperature  $\langle T \rangle(r, \varphi)$  in the meridian plane for  $Ra = 3 \times 10^7$ ,  $n_g = 0$ , and  $\varepsilon = 0.8$ . (b) Instantaneous velocity in the meridian plane for  $Ra = 3 \times 10^7$ ,  $n_g = 0$ , and  $\varepsilon = 0.8$  colored by temperature; (c) Schematic illustration of gravity decomposition  $\mathbf{g} = \mathbf{g}_{PO} + \mathbf{g}_{PO,\perp}$  when the gravity center  $G$  does not coincide with the geometrical center  $O$ .

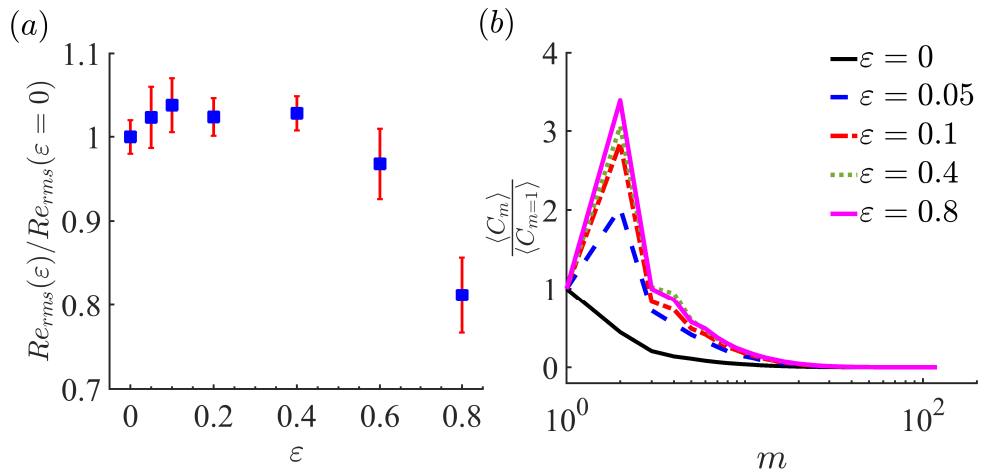


Figure 4.4: (a) Volume averaged  $Re_{rms}(\varepsilon)/Re_{rms}(\varepsilon = 0)$  as a function of  $\varepsilon$  for  $Ra = 3 \times 10^7$  and  $n_g = 0$ . The error bars indicate the corresponding standard deviations. We note the standard error is smaller than the symbol size. (b) TKE Spectrum of  $\langle C_m \rangle$ , normalized by  $\langle C_{m=1} \rangle$ , as a function of the spherical harmonic order  $m$  for different  $\varepsilon$ .

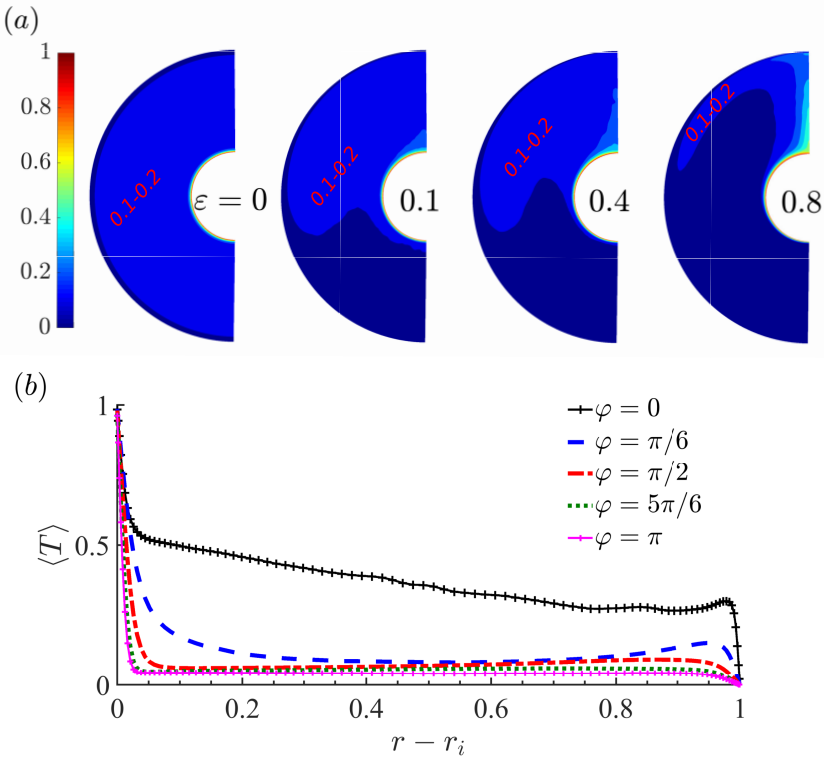


Figure 4.5: (a) Mean temperature  $\langle T \rangle(r, \varphi)$  in the meridian plane for  $Ra = 3 \times 10^7$ ,  $n_g = 0$ , and  $\varepsilon = 0, 0.1, 0.4$ , and  $0.8$ . Panel (b) shows mean temperature profiles at different co-latitudinal locations for  $\varepsilon = 0.8$ .

geometric counterpart  $\varepsilon > 0$ , the buoyancy force component induces the long-wavelength structures of order  $m = 2$  in the system. Although the mean intensity of the TKE changes non-monotonically with varying  $\varepsilon$ , the ratio between  $\langle C_{m=2} \rangle$  and  $\langle C_{m=1} \rangle$  increases monotonically with  $\varepsilon$ . The  $m = 2$  mode, which captures the strength of the large-scale flow features, is already dominant for small  $\varepsilon$  as only a small offset in the gravity center location is required to form the jet and the corresponding meridional circulation. The subsequent increase in the ratio  $\langle C_{m=2} \rangle / \langle C_{m=1} \rangle$  is slow.

#### 4.3.3 Modulation of temperature distribution and heat-transfer rate

As we have shown, the gravity center offset largely influences the flow structures. This naturally raises a question on how the mean temperature profiles and thus the heat fluxes are influenced. Figure 4.5(a) shows the mean temperature contour in the meridian plane with increasing  $\varepsilon$ . In the bulk region, a low-temperature region firstly appears in the Southern Hemisphere for  $\varepsilon \leq 0.4$ , which can extend to the Northern Hemisphere for  $\varepsilon = 0.8$ . Near the North Pole, the hot plumes emit from the inner sphere to form a high-temperature flow, as shown in figure 4.2.

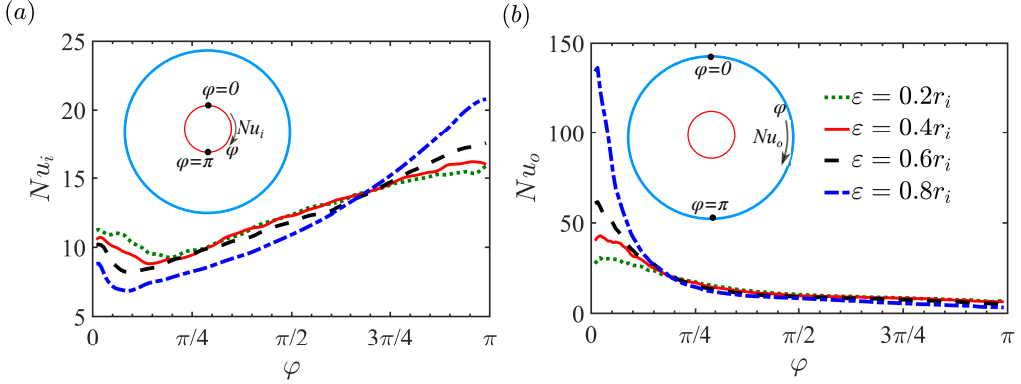


Figure 4.6: (a)  $Nu$  number on the inner and (b) outer sphere as a function of the co-latitudinal direction for  $Ra = 3 \times 10^7$  and  $n_g = 0$ .

Furthermore, we plot temperature profiles at selected angular positions in the co-latitude of  $\varepsilon = 0.8$ . The temperature profiles show a strong dependence on  $\varphi$ . The temperature inversions are the most pronounced in the low-latitude region (upper hemisphere) near the outer sphere ( $0 \leq \varphi \leq \pi/2$  within  $0.6 < r - r_i < 0.95$ ). As shown in the last panel of figure 4.5(a), the convective jet near the North Pole ejects high-temperature fluid from the inner boundary layer to the outer sphere, where it subsequently spreads out and descends along the cold outer sphere, forming a ‘crescent’ structure when  $\varepsilon = 0.8$ . The relatively high-temperature ‘crescent’ structure spreads into the low-temperature bulk region resulting in the temperature inversions.

Next, we examine how the local heat fluxes depend on  $\varepsilon$ . Figure 4.6 shows profiles of the Nusselt number on the inner sphere ( $Nu_i$ ) and the outer sphere ( $Nu_o$ ) along the latitude  $\varphi$ . It is observed that the local heat fluxes on the outer sphere decrease from  $\varphi = 0$  (North Pole) to  $\pi$  (South Pole), whereas the opposite trend, is observed on the inner sphere. This happens because the hot convective jet impinges on the outer boundary layer, resulting in the thinner thermal boundary layer and larger heat flux compared to the situation without a convective jet.

Despite the highly non-uniform heat flux distribution over the inner and outer spheres and markedly different flow structures caused by the gravity center offset, interestingly, the global heat transfer is insensitive to  $\varepsilon$  as shown in figure 4.7. For  $\varepsilon \leq 0.6$  the difference between  $Nu(\varepsilon > 0)$  and  $Nu(\varepsilon = 0)$  is less than 5%. Only for  $\varepsilon = 0.8$ , depending on the gravity profiles, the reduction of global heat fluxes can be almost 10%. The details of the effect of gravity profiles will be discussed in the next section.

#### 4.3.4 Additional parameters: $n_g$ and $Ra$

So far we focused on the effect of the gravity center location for  $Ra = 3 \times 10^7$  and  $n_g = 0$ . This section demonstrates that the formation of the large-scale flow structures described above is similar for different  $n_g$  and  $Ra$ , while the intensity

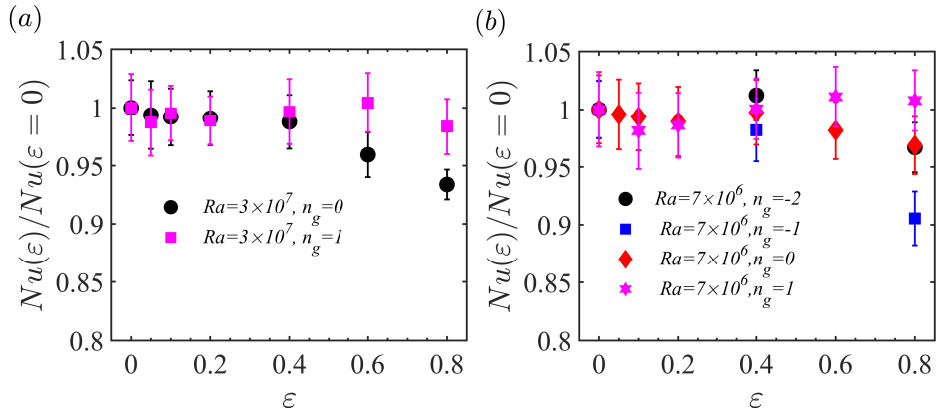


Figure 4.7: (a)  $Nu(\varepsilon)/Nu(\varepsilon = 0)$  as a function of  $\varepsilon$  for (a)  $Ra = 3 \times 10^7$  and (b)  $Ra = 7 \times 10^6$  and different gravity profiles. The error bars indicate the standard deviations of the  $Nu$  values averaged over the inner and outer sphere. We note the standard error and the  $Nu$  difference between the inner and outer sphere are both smaller than the symbol size so that they are not visible.

of the long-wavelength structures is significantly modified.

The left panel of figure 4.8 shows visualizations of the convective jet for different gravity profiles. The corresponding spectral analysis presented in figure 4.9(a) shows that the large-scale flow structure is dominated by the  $m = 2$  mode for all cases. However, a comparison of the TKE spectra  $\langle C_m \rangle$  for different  $n_g$  in figure 4.9(b) reveals that the flow becomes much more turbulent when  $n_g$  is decreased. The increase is more pronounced for the small scales (high wavenumbers, i.e.,  $m > 10$ ) than large scales ( $m < 10$ ). The reason for the increased turbulence with decreasing  $n_g$  (see equation 4.6) is that the buoyancy near the inner sphere becomes stronger. Furthermore, the spectral analysis for a constant  $n_g = 0$  and varying  $Ra$  in figure 4.10(a) confirms that the flow remains dominated by structures of the same size. Panel (b) shows the spectrum for  $Ra = 3 \times 10^7$  normalized by the spectrum for  $Ra = 7 \times 10^6$ . This figure confirms that the flow becomes more turbulent with increasing  $Ra$  and shows that the TKE contained in large-scales (with low wavenumber  $m < 10$ ) slightly decreases while the energy in the small scales ( $m > 10$ ) increases rapidly.

#### 4.4 Concluding remarks

To get a better understanding of the effects the hemispherical asymmetric of Earth's inner core may have, we use direct numerical simulations of spherical Rayleigh-Bénard convection to study the effect of off-centered gravity. When the gravity center is located at the geometrical center, the system has spherical symmetry, which is shown by evenly distributed plume emission over the spheres. However, when an off-center buoyancy component is introduced by shifting the gravity center away from the geometrical one, we observe significant changes in the flow structure. When the gravity center is moved to the South, a strong convective jet on the Northern side of the inner sphere is formed, which leads to

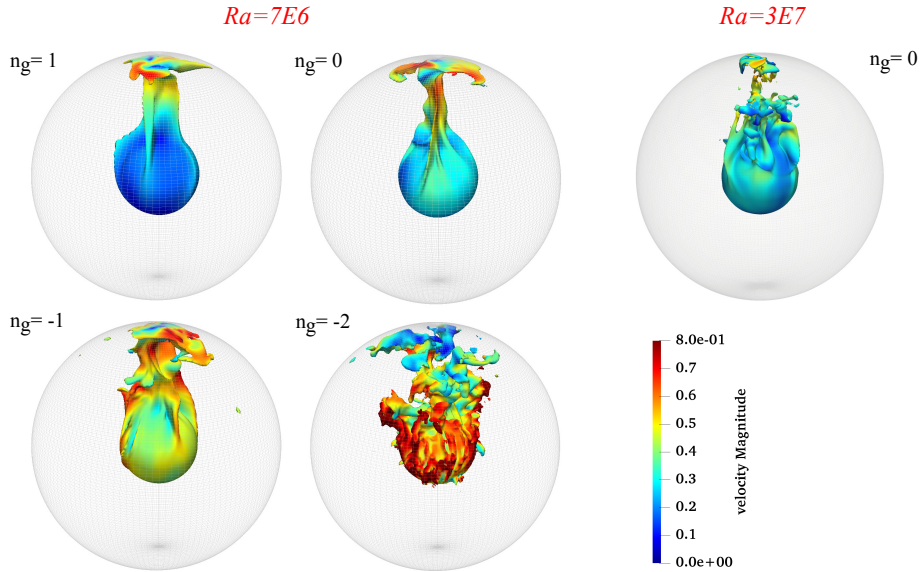


Figure 4.8: Instantaneous isosurface of  $T = 0.3$  for different gravity distributions from  $n_g = 1$  to  $n_g = -2$  (see equation 4.6) for  $Ra = 7 \times 10^6$  and  $\varepsilon = 0.8$ . The rightmost panel shows  $Ra = 3 \times 10^7$ ,  $n_g = 0$ , and  $\varepsilon = 0.8$  for comparison. The color represents for velocity magnitude at the isosurface.

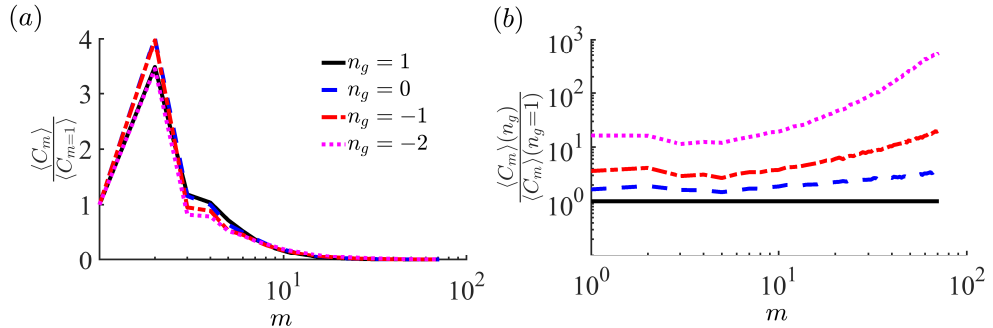


Figure 4.9: TKE spectrum for different gravity profiles when  $\varepsilon = 0.8$ : (a) normalized by  $\langle C_{m=1} \rangle$ ; (b) normalized by  $\langle C_m \rangle(n_g = 1)$ .

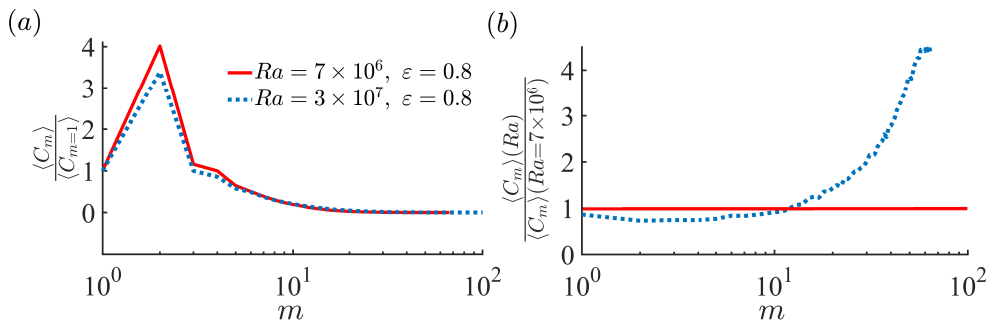


Figure 4.10: TKE spectrum for different  $Ra$  when  $\varepsilon = 0.8$ : (a) normalized by  $\langle C_{m=1} \rangle$ ; (b) normalized by  $\langle C_m \rangle(Ra = 7 \times 10^6)$ .

a large-scale flow organization with hot ascending fluid close to the inner sphere and cold descending fluid close to the outer sphere. The formation of these large-scale flow structures has been confirmed by modal analysis, revealing that the dominant flow structures have a wavenumber ( $m = 2$ ). Due to the large-scale flow organization, the heat transfer at the inner and outer sphere is highly non-uniform in the co-latitudinal direction. In particular, around the North Pole, the heat flux is enhanced on the outer sphere due to the impingement of the convective jet. However, a surprising finding is that, even though the flow structure and local heat fluxes change significantly, the global heat flux is relatively insensitive to the gravity center's shift. These results do not seem to depend much on  $Ra$  (over our explored range) or the employed gravity profile.

Using idealized spherical Rayleigh-Bénard convection, we have demonstrated that even a small shift of the gravity center introduces pronounced changes in the flow organization and local heat fluxes. In the geophysical context, we note that the Earth's core exhibits an East-West asymmetry resulting from a crystallizing (heavier) Western hemisphere and a melting (lighter) Eastern hemisphere. It means that the mass center gradually translates to the West (heavier hemisphere) [6, 107]. Our study indicates that this mass center shift can form a high-temperature region in the Eastern hemisphere and a low-temperature region in the Western hemisphere. Therefore, the introduced flow pattern can further encourage the mass center to drift towards the West. Although spherical Rayleigh-Bénard convection is a simplified representation of what may happen in the Earth, the present results show that it is essential to consider small hemispherical asymmetries. This study should be considered a first step towards realizing a numerical model aimed at capturing the dynamics in the Earth's outer core and mantle, even though many additional features, such as rapid rotation [77], Earth's dynamo [9], and temperature-dependent fluid properties are not yet included.



## CHAPTER 5

# Diffusion-free scaling in rotating spherical Rayleigh-Bénard convection\*

### 5.1 *Introduction*

Rapidly rotating convection is relevant for many geophysical and astrophysical flows, e.g. the solar interior [129], the liquid metal core of terrestrial planets [166, 110, 74, 10], and Earth’s oceans and atmosphere [103, 45]. In these instances of convection with strong thermal driving, the flow dynamics is nevertheless dominated by the strong background rotation [140, 10, 91, ]. The effect of rotation has been extensively studied in Rayleigh-Bénard (RB) convection experiments [122, 96, 146, 86, 84, 169, 40, 141, 27, 161] and simulations [86, 84, 85, 127, 146, 141, 69, 92]. In the canonical RB system, the flow is confined between two parallel plates, and this system is studied in 3D periodic, rectangular, or cylindrical domains. In the remainder of this paper, we refer to this as planar RB convection to distinguish it from the spherical RB system considered in here (see figure 5.1(a)). We refer the reader to the reviews [10, 114, 91] for an extensive explanation of rotating RB convection. Even though there are great community efforts on rotating RB the diffusion-free scaling regime, geostrophic dominated which will be defined explicitly below, predicted for strongly thermally driven rotation dominated flow has not been observed yet for rotating RB with no-slip boundaries. This study will show that in a spherical RB convection, the geometry allows for the formation of a geostrophic dominated flow region that exhibits diffusion-free scaling in the mid-latitude region.

The control parameters of rotating RB flow are the Rayleigh ( $Ra$ ), Ekman ( $Ek$ ), and Prandtl ( $Pr$ ) numbers, to be defined explicitly below. Derived from these, the convective Rossby number  $Ro \equiv \sqrt{Ra/PrEk}/2$  characterizes the importance of the thermal forcing relative to rotation [53]. With increasing Rayleigh number  $Ra$  and for strong rotation  $Ro \ll 1$ , two regimes can be identi-

---

\*Based on G. Wang, L. Santelli, R. Verzicco, D. Lohse, R. J. A. M. Stevens, *Diffusion-free scaling in rotating spherical Rayleigh-Bénard convection*, Geophysical Research Letter, 48 (2021), <https://doi.org/10.1029/2021GL095017>

fied, namely: (1) the *weakly nonlinear regime* for  $Ra$  near the onset of convection, (2) the *quasi-geostrophic regime* for  $Ra/Ra_c \leq 3$  [40], where  $Ra_c \sim Ek^{-4/3}$  is the critical Rayleigh number for the onset of convection [26]. In a third regime (3), for  $Ro \gg 1$  and high enough  $Ra$ , the flow approaches the non-rotating RB convection case [58, 3, 29].

For the quasi-geostrophic regime, when  $Ek \rightarrow 0$ , the Nusselt number  $Nu$  (i.e. the non-dimensional heat transfer) is found to depend on the supercriticality  $Nu \sim Pr^\gamma (Ra/Ra_c)^\alpha$  [84, 77, 141, 28]. When the heat transport is independent of molecular diffusion in the asymptotic limit, this results in  $\alpha = 3/2$  and  $\gamma = -1/2$ . This scaling  $Nu \sim Pr^{-1/2} (Ra/Ra_c)^{3/2}$  is known as *diffusion-free scaling*. The physics of the diffusion-free scaling, similar to the ultimate regime in RB convection [89, 139, 137, 60], is that the thermal and kinetic boundary layers, and thus the kinematic viscosity and thermal diffusivity, do not play an explicit role anymore for the heat flux scaling. This is known as bulk dominated convection.

So far, the diffusion-free scaling has only been obtained in planar convection by considering an asymptotically reduced model in which Ekman pumping effects are not represented [77] and numerical simulation with free-stress boundaries and  $Ek \leq 10^{-6}$  [141, 92]. For planar convection with no-slip boundaries, [84, 85] theoretically predict  $\alpha = 3$  for  $Ra \lesssim Ek^{-3/2}$ . This finding follows from an analysis of the boundary layer stability and is supported by experimental and simulation data for  $10^{-6} \leq Ek \leq \infty$ . The difference between  $\alpha = 3$  for no-slip boundaries and  $\alpha = 3/2$  for free-stress boundaries is attributed to the active role of the Ekman pumping in the boundary layers near the plates [115, 76]. However, the asymptotic diffusion-free scaling exponent  $\alpha = 3/2$  has not been reported for no-slip boundaries in planar convection.

However, [50] find the diffusion-free scaling for  $Ek \leq 10^{-5}$  for  $6Ra_c \leq Ra \leq 0.4Ek^{-8/5}$  in spherical RB convection with inner-to-outer radius ratio  $\eta = 0.6$  and no-slip boundaries. The  $Ek^{-8/5}$  scaling is proposed by [77, 78]. We note that previous theories of [53] (giving the transitional Rayleigh number  $Ra_t \sim Ek^{-2}$  where  $Ra_t$  represents for the upper bound of the diffusion-free scaling region) and of [86] (giving  $Ra_t \sim Ek^{-7/4}$ ) do not appropriately capture the upper bound of the diffusion-free scaling region, which scales as  $Ek^{-8/5}$ .

The objective of this work is to elucidate the observation of diffusion-free scaling in spherical RB convection at relatively weak rotation ( $Ek \sim 10^{-5}$ ), while this scaling is not observed in planar convection. For strong rotation  $Ro \ll 1$ , the Taylor Proudman effect [152] favors invariance along the rotation axis. In planar convection, see figure 5.1(a), the rotation axis is orthogonal to the plates, and the convective columns are homogeneously distributed in the horizontal direction and always stretch between the hot and cold plates. However, in spherical geometry, the rotation effect is latitude dependent, see figure 5.1(b), due to which three distinctly different flow regions are formed. Inside the inner sphere's tangent cylinder, the convective columns touch the inner and outer spherical boundaries. In the mid-latitude region the convective columns are stretched between the Northern and Southern hemispheres of the outer sphere. Near the equator, the convective columns adjust themselves to the curved boundary. This work will show that the diffusion-free scaling originates from this mid-latitude region. The

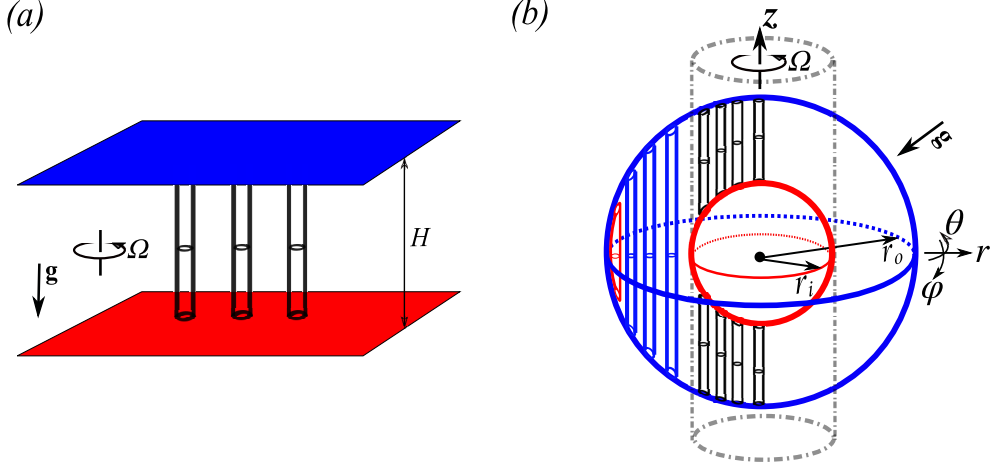


Figure 5.1: Schematics showing the alignment of the axial convective columns in (a) canonical framework heated from bottom and cooled from above and (b) spherical rotating RB convection heated from inner and cooled from outer, in which the gravity points towards the geometrical centre. The longitudinal (azimuthal), co-latitudinal (polar), and radial directions are represented by  $\hat{\theta}$ ,  $\hat{\varphi}$  and  $\hat{r}$ , respectively. The rotation axis aligns with the  $z$ -direction. The angle between gravity and rotation axis is  $\varphi$ . The tangent cylinder is shown with dashed-dotted grey line. Panel (b) is adapted from [22, 23, 10].

paper is organized as follows: In Section 5.2, we introduce the spherical RB system with its control parameters. Section 5.3 is an overview of our simulation results compared and validated to literature, subsequent analysis is performed in Sections 5.4 and 5.5. Finally, we conclude our findings in Section 5.6. In appendix C some additional information about the simulations performed for this study are given.

## 5.2 Numerical method, control and response parameters

A sketch of the rotating spherical RB geometry is shown in figure 5.1(b). A fluid fills a spherical shell between the inner sphere of radius  $r_i$  and outer sphere of radius  $r_o$  with distance  $d = r_o - r_i$  from the inner one. The whole system rotates about the vertical  $z$  axis at angular velocity  $\Omega$ . The surface temperature of the inner and outer spheres is kept constant at  $T_i$ , and  $T_o$ , respectively, with  $T_i > T_o$ . No-slip boundary conditions are imposed at both spheres. We solve the Navier-Stokes equations in spherical coordinates within the Boussinesq approximation, which in dimensionless form read:

$$\frac{\partial \mathbf{u}}{\partial t} + \mathbf{u} \cdot \nabla \mathbf{u} = -\nabla p + \sqrt{\frac{Pr}{Ra}} \nabla^2 \mathbf{u} + g T \vec{\mathbf{e}}_r - \frac{1}{Ro} \vec{\mathbf{e}}_z \times \mathbf{u} , \quad \nabla \cdot \mathbf{u} = 0, \quad (5.1)$$

$$\frac{\partial T}{\partial t} + \mathbf{u} \cdot \nabla T = \frac{1}{\sqrt{RaPr}} \nabla^2 T. \quad (5.2)$$

where  $\mathbf{u}(\vec{x}, t)$ ,  $p(\vec{x}, t)$ ,  $T(\vec{x}, t)$ , and  $g(r)$  denote the fluid velocity, pressure, temperature and radially dependent gravitational acceleration.

In this study we focus on a radius ratio  $\eta = r_i/r_o = 0.6$  and the gravity profile  $g(r) \sim (r_o/r)^2$  valid for homogeneous mass distribution to allow comparisons with non-rotating [49] and rotating [50] convection in spherical RB. This system configuration is considered representative for studying convection in gas giants [97]. Additionally, we perform simulations for  $\eta = 0.35$  and  $g(r) \sim (r_o/r)^{-1}$ , which is considered an Earth-like configuration used by [163] and [97]. The equations are discretized by a staggered central second-order finite-difference scheme in spherical coordinates [125]. We use a uniform grid in the longitudinal and co-latitudinal directions and ensure that the bulk and boundary layers are appropriately resolved [145]. The grid cells are clustered towards the inner and outer sphere to ensure the boundary layers are adequately resolved [136].

The dynamics of rotating spherical RB convection are determined by the Rayleigh, Prandtl, and Ekman numbers

$$Ra = \frac{\beta g_o d^3 \Delta T}{\kappa \nu}, \quad Pr = \frac{\nu}{\kappa}, \quad Ek = \frac{\nu}{\Omega d^2}, \quad (5.3)$$

where  $\beta$  is the thermal expansion coefficient,  $g_o$  is the gravity at the outer sphere,  $\nu$  is the kinematic viscosity, and  $\kappa$  is the thermal diffusivity of the fluid.  $Ra$  is a measure of the thermal driving of the system,  $Ek$  characterizes the ratio of viscous to Coriolis forces, and  $Pr$  indicates the ratio of the viscous to thermal diffusivities. In this study we consider  $Pr = 1$ . We use the Rossby number  $Ro \equiv \sqrt{Ra/PrEk}/2$  to evaluate the relative importance of rotation and buoyancy [53]. We normalize the results using the length scale  $d = r_o - r_i$ , the temperature difference  $\Delta T$  between inner and outer sphere, and the free-fall velocity  $U = \sqrt{\beta g_o \Delta T d}$ .

The Nusselt number quantifies the non-dimensional heat transport

$$Nu = \frac{\overline{\langle u_r T \rangle_s} - \kappa \partial_r \overline{\langle T \rangle_s}}{-\kappa \partial_r T_c}, \quad (5.4)$$

where  $T_c(r) = \eta/[(1-\eta)^2 r] - \eta/(1-\eta)$  is the conductive temperature profile in spherical shells with constant temperature boundary conditions  $T_c(r_i) = 1$  and  $T_c(r_o) = 0$ . The notations  $\langle \dots \rangle_s$  represents the average over a spherical surface with constant distance from the center, e.g.  $\langle T \rangle_s = \frac{1}{4\pi} \int_0^{2\pi} \int_0^\pi T(\theta, r, \varphi) \sin \varphi d\varphi d\theta$ . Overbar  $\overline{\dots}$  corresponds to time averaging. In the following discussion, we will use  $Nu$  on the outer sphere as a function of the co-latitude

$$Nu(\varphi) = -\frac{1}{\eta} \left. \frac{d \overline{\langle T \rangle_\theta}}{dr} \right|_{r_o} \quad (5.5)$$

where  $\langle \dots \rangle_\theta$  represents the average over the azimuthal direction, e.g.  $\langle T \rangle_\theta = \frac{1}{2\pi} \int_0^{2\pi} T(\theta, r, \varphi) d\theta$ .

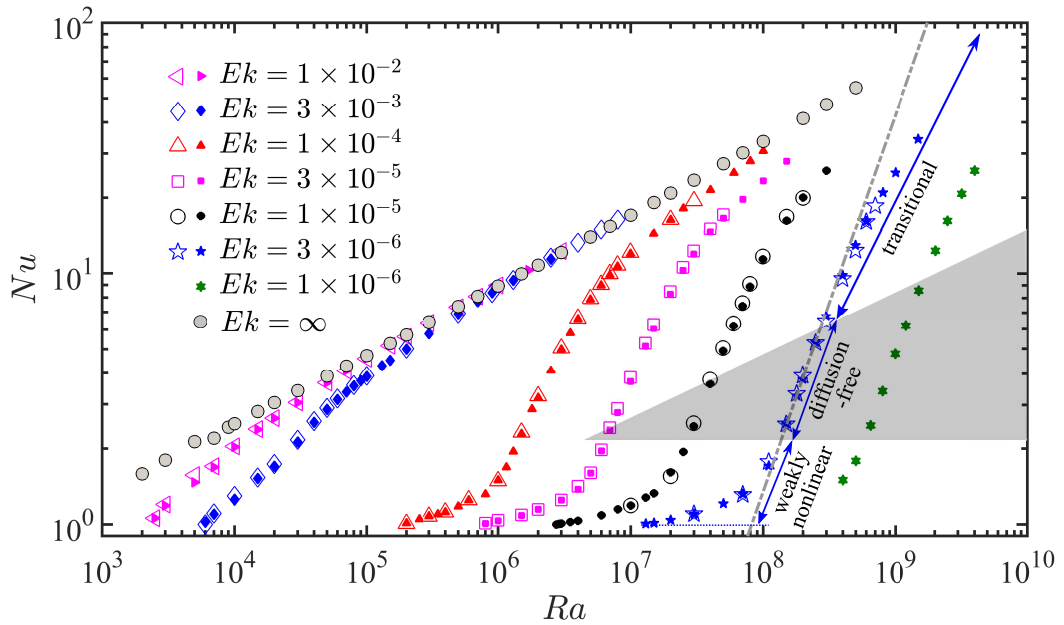


Figure 5.2:  $Nu$  as function of  $Ra$  for different  $Ek$ . Rotating cases: open symbols indicate the present results, filled-in symbols are those from [50]. Non-rotating cases from [49] are indicated by  $Ek = \infty$ . The shaded wedge-shaped region indicates the diffusion-free scaling regime ( $6Ek^{4/3} \leq Ra \leq 0.4Ek^{-8/5}$ ), which corresponds to the quasi-geostrophic regime identified by [50]. The dot-dashed grey line gives the diffusion-free scaling  $Nu = 0.149R^{3/2}$  for  $Ek = 3 \times 10^{-6}$ . The error bars are smaller than the symbol sizes.

### 5.3 Heat transfer in rotating spherical RB convection

Figure 5.2 shows  $Nu$  as function of  $Ra$  for various  $Ek$ . The results from our simulations agree excellently with those from [50]. For strong enough rotation (e.g.  $Ek \leq 3 \times 10^{-5}$ ), with increasing  $Ra$  three regimes can be identified [50, 97]. For low  $Ra$ , in the weakly nonlinear regime, rotational effects are dominant ( $Ro \ll 1$ ) and  $Nu \sim R^\alpha$  with  $R \equiv RaEk^{4/3}$  and  $\alpha = 1$ . In the quasi-geostrophic regime with diffusion-free scaling  $\alpha = 3/2$ , the Taylor-Proudman effect favours invariance along the rotation axis, thereby suppressing global heat transport relative to non-rotating case [77]. This regime is observed for  $6Ek^{4/3} \leq Ra \leq 0.4Ek^{-8/5}$  [50]. The lower bound is related to  $Ra_c$ , while the upper bound corresponds to the asymptotic prediction for bulk-limited heat transfer in geostrophic turbulence by [77]. In the transitional regime between strong and weak rotation ( $Ro \sim 1$ ) the buoyancy force gradually becomes dominant over rotational effects with increasing  $Ra$  and the flow eventually approaches the non-rotating case for  $Ro \gg 1$ .

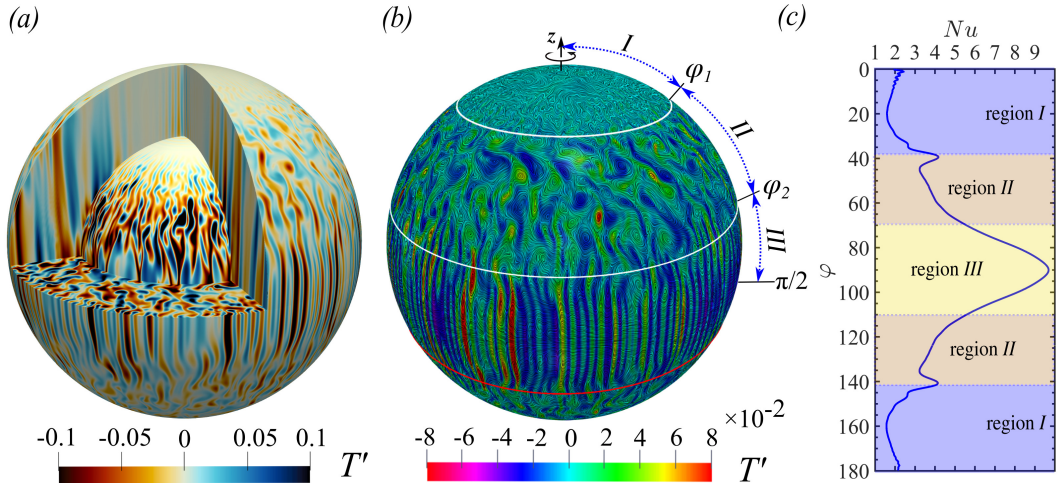


Figure 5.3: (a) Contour of the temperature fluctuation  $T'$  on two meridional cuts, equatorial section, and two spherical surfaces (corresponding to the surface located at the inner ( $r = r_i + \lambda_{T,i}$ ) and outer ( $r = r_o - \lambda_{T,o}$ ) thermal boundary layers. (b) Contour of  $T'$  with streamlines illustrated by using line integral convolution on the outer radial surface. The definition of the three regimes I, II, III is given in the text and figure 5.4. (c)  $Nu$  as function of the co-latitude  $\varphi$  on the outer sphere. In all cases (a)-(c),  $Ek = 1 \times 10^{-5}$  and  $Ra = 5 \times 10^7$

## 5.4 Identification of three flow regimes

Figure 5.3(a) visualizes the columnar structures by  $T' > 0$  and  $T' < 0$ , here  $T'(\theta, r, \varphi) = T(\theta, r, \varphi) - \langle T \rangle_s$ ,  $\langle T \rangle_s$  is defined in Section 2. The inner and outer thermal boundary layer thickness  $\lambda_{T,i}$  and  $\lambda_{T,o}$  is defined by the intersection of the linear fit to  $\langle T \rangle_s$  near the boundaries and the profile at mid-depth [50, 97]. Figure 5.3(b) clearly shows that there are three distinct flow regions. Region I spans from the rotation axis to  $\varphi_1$ , where  $\varphi_1$  can be determined by the intersection between the cylinder tangent to the inner sphere with the outer sphere. In this region, the columnar structures connect the boundary layers around the inner and outer spheres. Region II is found between  $\varphi_1$  and  $\varphi_2$  (see figure 5.3(b)),  $\varphi_2$  being the maximum zonal flow location (see below). In this mid-latitude region, the structures are the strongest, and tall thin columns stretch from the Northern to the Southern parts of the cold outer sphere. Region III is the region around the equator, see figure 5.3(b). In this region, the structures aligned with the rotation axis are much shorter than in the mid-latitude region II, while they conform themselves to the outer spherical boundary. Figure 5.3(c) shows that the heat transport strongly depends on the latitude [163], which means that the heat transfer in the different flow regions identified above is different.

[11] and [31] found that the zonal flow is prograde at low latitude near the outer boundary and retrogrades near the tangent cylinder that encloses the central core. Therefore, the zonal flow is suitable to identify the boundary between region II and III. Figure 5.4 (a,b) show how we use the local maximum prograde zonal

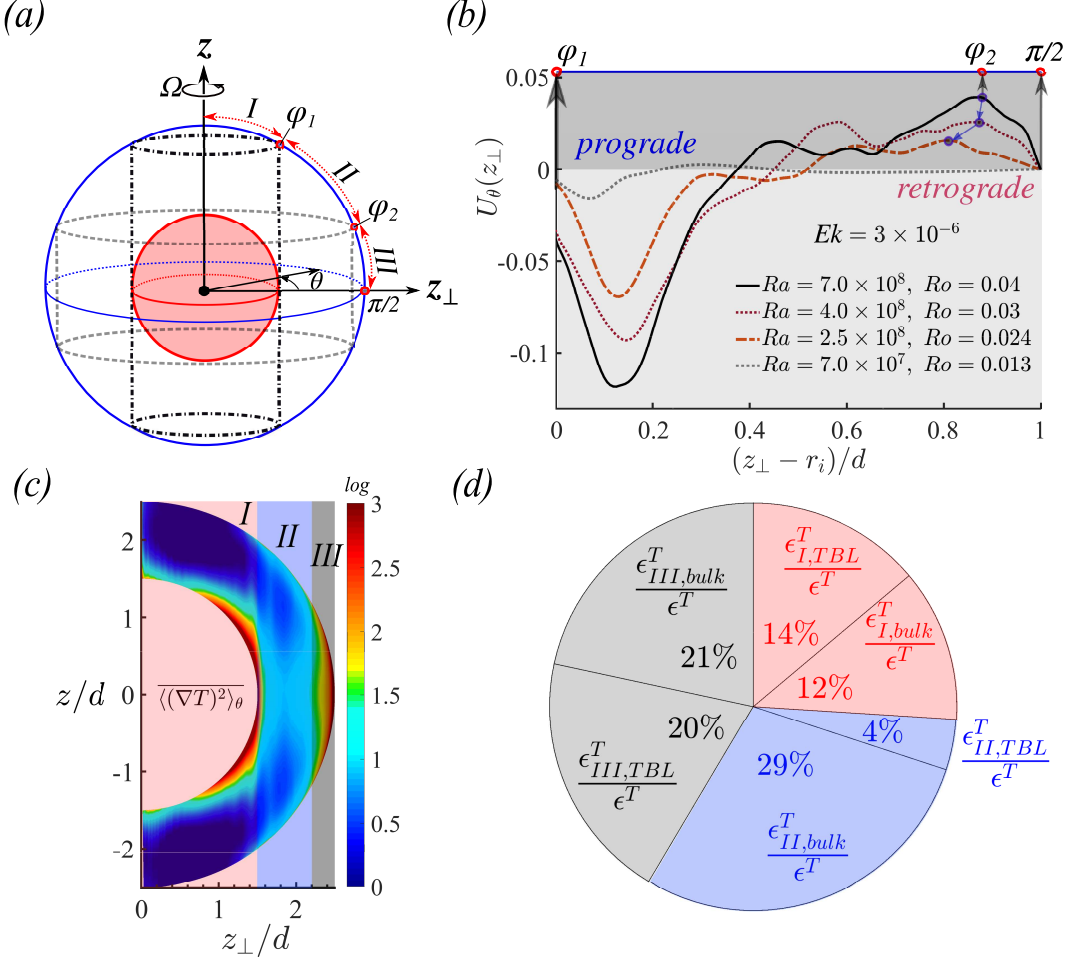


Figure 5.4: (a) Cylindrical polar coordinates \$(z, z\_\perp, \theta)\$, \$z\$ is the rotation axis, \$z\_\perp\$ is the cylindrical radius and \$\theta\$ is the azimuthal angle and of which the regimes I, II, III can be defined as shown. (b) Ensemble averaged azimuthal velocities \$U\_\theta(z\_\perp)\$ as a function of \$z\_\perp\$ in equation (5.6). \$(z\_\perp - r\_i)/d = 0\$ and 1 correspond to the tangent cylinders of the inner and outer spheres, respectively. \$\varphi\_2\$ is determined by the \$z\_\perp\$ location close to the outer sphere (\$z\_\perp - r\_i)/d = 1\$) where the zonal flow is strongest. (c) Time and Azimuthal averaged thermal dissipation \$\overline{\langle (\nabla T)^2 \rangle}\_\theta\$ in the meridional plane for case No.76 of \$Ek = 1 \times 10^{-5}\$ and \$Ra = 5 \times 10^7\$. (d) Pie chart for (c) showing the distribution of the thermal dissipation rate over the different regions in the boundary layer and bulk, see equation (5.8).

velocity close to the equator to set  $\varphi_2$ . Figure 5.4(a) illustrates the cylindrical coordinate system  $(z, z_\perp, \theta)$  that is used to represent the zonal flow in figure 5.4(b). The zonal flow is the ensemble average of the azimuthal velocity in cylindrical coordinate

$$U_\theta(z_\perp) = \overline{\langle u_\theta(z, z_\perp, \theta) \rangle_{\theta,z}} \quad (5.6)$$

where  $u_\theta(z, z_\perp, \theta)$  is the longitudinal velocity  $u_\theta(\theta, r, \phi)$  in spherical coordinate projected to cylindrical coordinate,  $\langle \dots \rangle_{\theta,z}$  indicates spatial average over a cylindrical surface (in the azimuthal and vertical direction), and  $\overline{\dots}$  indicates time-averaging.

We analyze the thermal dissipation in the different flow regions to determine whether the different regions are dominated by the boundary layer or the bulk dynamics. For spherical shells with radius ratio  $\eta$ , the thermal dissipation rate

$$\epsilon^T \equiv \overline{\langle (\nabla T)^2 \rangle} = \frac{3\eta}{1 + \eta + \eta^2} Nu \quad (5.7)$$

by volume integral of  $T \times (5.2)$ . Figure 5.4(c) shows the time-averaged thermal dissipation rate in the meridional plane. The figure shows that the thermal dissipation intensity is highest in the boundary layers along the inner sphere (region I) and close to the equator region along the outer sphere (region III). We determine the distribution of the thermal dissipation rate over the different regions as follows

$$\epsilon^T = \epsilon_{I,bulk}^T + \epsilon_{I,TBL}^T + \epsilon_{II,bulk}^T + \epsilon_{II,TBL}^T + \epsilon_{III,bulk}^T + \epsilon_{III,TBL}^T, \quad (5.8)$$

where bulk indicates the bulk regions and TBL indicates the thermal boundary layer regions, i.e. for the radial locations  $r$ ;  $r_i \leq r \leq r_i + \lambda_{T,i}$  along the inner sphere and  $r_o - \lambda_{T,o} \leq r \leq r_o$  along the outer sphere. Figure 5.4(d) confirms that regions I and III are both strongly affected by the boundary layer dynamics. However, region II turns out to be bulk-dominated. We note that the boundary between region II and III is not determined based on the thermal dissipation profiles as there is not a clear peak in the direction separating the regimes. Therefore, as discussed above, we use the maximum in the zonal flow profile to determine this transition.

In the following section, we will show that, in agreement with theoretical expectations discussed above, the scaling of the heat transfer in the region II follows the diffusion-free scaling for rotation dominated strongly thermally driven flows.

## 5.5 Diffusion-free scaling in region II

Figure 5.5 shows  $Nu$  on the outer sphere compensated with the diffusion-free scaling law. Panel 5.5(a) shows that for the global heat transfer and  $Ek \leq 5 \times 10^{-5}$  the diffusion-free scaling is observed for  $R \geq 6$ . The crossover from the quasi-geostrophic region to the transitional region is observed at  $Ra_t = 0.4Ek^{-8/5}$

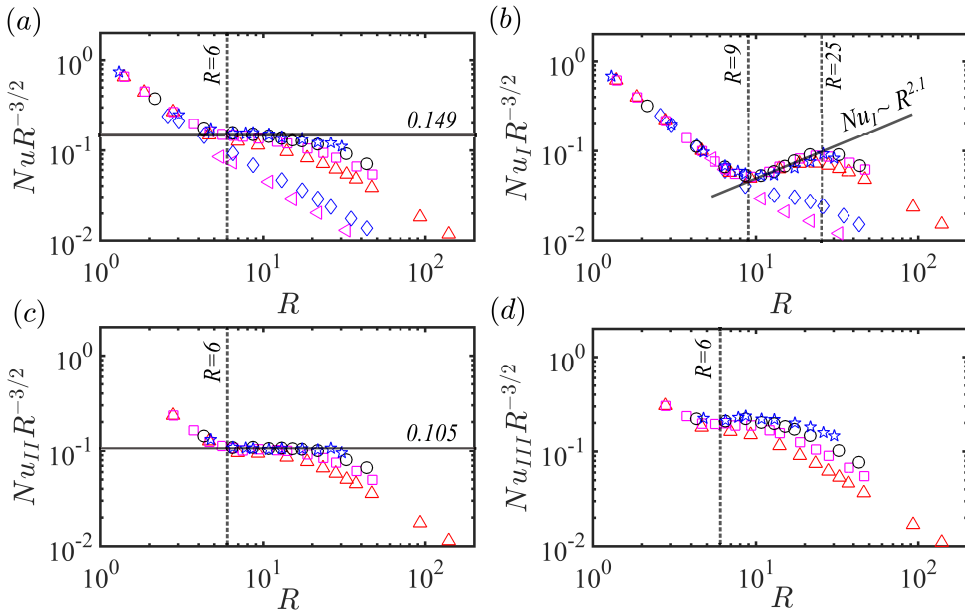


Figure 5.5:  $Nu$  on the outer sphere compensated by  $R^{-3/2}$  and as a function of  $R \equiv RaEk^{4/3}$ . (a) Integration over the whole sphere; (b-d)  $Nu$  in regions (I – III), see figure 5.3(b). The symbols have the same meaning as in figure 5.2.

[50]. Figures 5.5(b-d) show the heat transfer scaling in the different flow regions identified above. Panel 5.5(b) evidences that, due to Ekman pumping [141, 169, 142, 143], the heat transport scaling in region I is  $Nu_I \sim R^{2.1}$ . This is steeper than the  $\alpha = 3/2$  scaling for diffusion-free convection, but shallower than the  $\alpha = 3$  value observed in planar convection [85]. Most importantly, panel 5.5(c) shows that the diffusion-free scaling is much more pronounced in region II than in region I. Although the diffusion-free scaling still starts at  $R = 6$ , it continues for much higher  $R$  than the global heat transfer, see figure 5.5(a). Panel 5.5(d) shows that no diffusion-free scaling regime is observed in region III.

The diffusion-free scaling regime is observed from  $6R$  up to  $Ra_t$ , where  $Ra_t$  indicates the  $Ra$  number at which the regime for bulk-limited heat transfer in geostrophic turbulence ends [77, 78]. It was demonstrated [50] that for the global heat transfer the diffusion-free scaling regime is observed up to  $Ra_t = 0.4Ek^{-8/5}$ , see also figure 5.6(a). For region II, figure 5.6(b) shows that the diffusion-free scaling is observed up to  $Ra_t = Ek^{-8/5}$ , which is considerably higher  $Ra$  than for the global heat transport.

The same conclusion is obtained by analyzing  $\eta = 0.35$ ,  $g(r) \sim (r_o/r)^{-1}$  and  $Ek = 1 \times 10^{-5}$ .

## 5.6 Conclusions

In conclusion, we have shown that rotating spherical RB convection has three distinctly different flow regions; see figure 5.3(b). In region I, convective columns are formed between the hot inner and cold outer spheres. The mid-latitude region

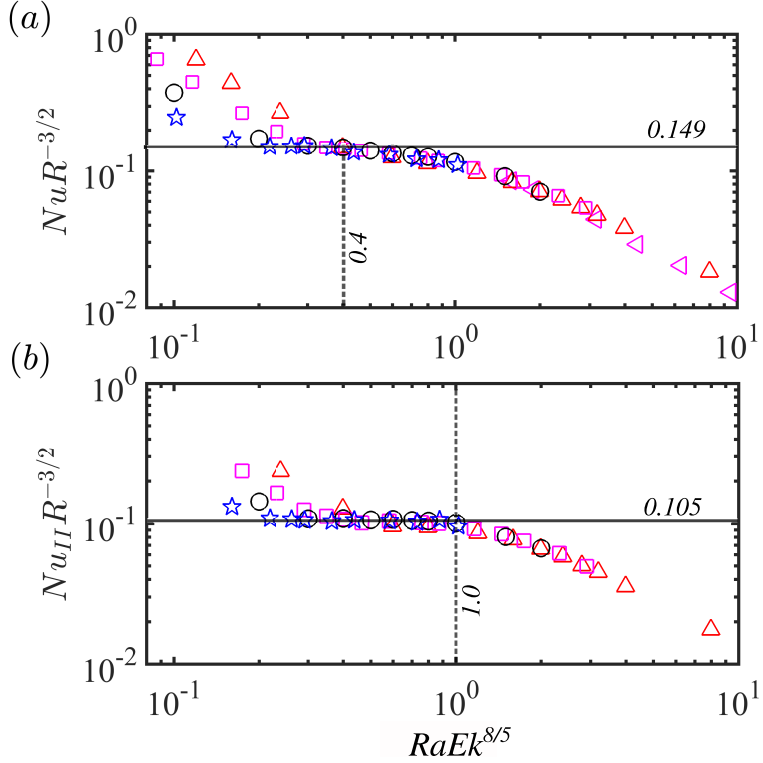


Figure 5.6:  $Nu$  compensated by  $R^{-3/2}$  as a function of  $RaEk^{8/5}$ . (a) Integration over the whole sphere. The horizontal line is  $NuR^{-3/2} = 0.149$  and the vertical line is  $RaEk^{8/5} = 0.4$ ; (b) Region II. The horizontal line is  $NuR^{-3/2} = 0.105$  and the vertical line is  $RaEk^{8/5} = 1$ . The symbols have the same meaning as in figure 5.2.

II is the region where the vertically aligned vortices are strongest, and the flow is bulk dominated. Region III is formed around the equator, and here the vortices are shorter and are affected by the outer spherical boundary.

The diffusion-free scaling  $Nu \sim (RaEk^{4/3})^\alpha$  with  $\alpha = 3/2$  originates from the mid-latitude flow region in which the flow dynamics are bulk dominated. In this region, thin and long convective columns are formed between the Northern and Southern parts of the cold outer sphere. This geostrophically dominated flow region can be formed due to the system geometry. Due to the curvature effects in spherical geometries, the latitude-dependent Coriolis force results in inhomogeneous convective columns in the co-latitudinal direction and more convective columns on the outer sphere than the inner sphere. These results show that the flow physics in rotating convection are qualitatively different in planar and spherical geometries.

# CHAPTER 6

## Conclusions

In this manuscript we have described and tested a novel second order numerical scheme for solving the Navier-Stokes equation in spherical coordinates under incompressibility hypothesis [124], and then we applied it to some open problems in natural convection between spherical shells.

In chapter 2, the second order accuracy in space is obtained through a finite-difference approximation on a staggered mesh. The (nonphysical) singularities appearing on the polar axis and at the center due to the change of coordinates are cured by introducing a new set of variables and utilising a special treatment for some terms. This technique allows us to use the scheme for the whole sphere up to  $r = 0$ .

Moreover, being the scheme based on finite-difference methods, the structure of the grid is very flexible, allowing non-uniform refinements on two of the three directions: azimuthal and latitudinal (poloidal). We have exploited this flexibility in a qualitative analysis of a space developing round jet with complex inflow/outflow boundary conditions. The longitudinal grid conserves stronger limitations related to the method used for the solution of the elliptic equation.

The scheme has been tested in several ways showing always an excellent agreement with literature [68, 49, 82, 12]. A Hill vortex, which is an exact solution of the Euler equation, has been used to simulate the most unfavorable conditions, such as large velocities through the sphere center or unnecessary refinements of the grid around singular points. By using the same setup we proved the scheme to be second order and fully comparable with simulations on Cartesian coordinates. Another important benchmark has been performed for thermally driven flows; for these tests the singularity at the origin has not been included allowing us to considerably increase the time step size. The heat transfer shows perfect agreement with literature, and the exact relations between dissipation rates and heat transfer are perfectly satisfied. We also analysed and compared the dynamics of fluids in a spinning and precessing sphere, once again obtaining perfect agreement with spectral methods from literature.

The structure of the code allows an easy parallelization, which has been implemented in order to run complex and deep simulations on thermally driven flows, some of which are further detailed in the manuscript.

In chapter 3, The dynamic of a Rayleigh-Bénard flow between two concentric spherical shells has been analysed using different radial gravity profiles: inverse

quadratic (comparable to atmosphere gravity), linear (inside of spherical bodies), a combination of the two to model the effect of different densities inside the Earth, a constant profile and an artificial parabolic profile for comparison. We also used two different Prandtl numbers for air, with  $Pr = 0.71$ , and water, with  $Pr = 7.1$ . The objectives were the characterization of the onset of convection, the fluid behaviour, and their dependence on the parameters chosen for the simulation. Results have shown that different gravity profiles apparently induce variations in the critical Rayleigh number needed for the onset of convection. Nevertheless the introduction of an effective Rayleigh number, computed by averaging the gravity profile over the radius, in most cases absorbed these differences and produced an universal value for the onset of convection. This allows us to reduce the parameter space needed for describing the system.

In this configuration, hysteresis has been observed: by reaching some critical values  $Ra_1$  and  $Ra_2$ , some features are introduced in the dynamic of the system. From that point onward, these features remain part of the evolution at any value of  $Ra$ . Variations in Prandtl number behave as expected: the onset of convection is not affected, while the value of  $Ra$  related to the emergence of time-dependent dynamic scales linearly with the Prandtl number. In fact, while  $R_c$  and  $R_1$  are comparable between fluids,  $Ra_{2,water} \approx 10Ra_{2,air}$ . This difference is attributable to the dependence on  $Pr$  in the viscous term.

Hysteresis occurs for both air and water. Between  $Ra_1$  and  $Ra_2$  we identified a meta-stable region (named region I), where the system jumps to a stabler configuration after some time has passed. For air we only identified a single transition to a stabler state, while for water region I is much larger, thus the system has several more states to explore. These states are characterised by a different harmonic spectrum and temperature profile (with less plumes), and their convective heat transfer decreases. Once one of these states is reached, the dynamic will not return back to the previous state, even when different values of  $Ra$  are explored. Increasing  $Ra$  past  $Ra_2$  leads the system to region II, where we observe the rise of a time-dependent behaviour during which additional components of the harmonic spectrum are excited. Reaching even higher  $Ra$  turns the periodic behaviour into a chaotic one, while reducing  $Ra$  from a system which explored region II does not cause the typical time-dependent features of the system to disappear, even for much lower values of  $Ra$ .

Using the same general configuration, in chapter 4 the effect of a shift in the position of the gravity center for thermally driven turbulent flows has been investigated. For the study a radius ratio of 0.6 and  $Pr = 1$  have been used, coupled with different values of  $Ra$  and gravity profiles. Any small difference between the sphere center and the gravity center breaks the spherical symmetry of the system. This leads to the formation of a jet in the opposite direction and a change in the large-scale flow structure, with hot ascending fluid close to the inner shell and cold, descending flow on the outer surface. However, while the local heat transfer is heavily influenced by these changes, maybe surprisingly the global heat flux seem to be not influenced by local variations of heat flux and flow structure. This simulation can be seen as a very simplified model for the analysis of Earth's outer core or mantle. Thus, when performing more complex

and precise analysis related to geophysical problems, it may be important to consider the presence of asymmetries in the mass distribution alongside already known behaviour like the dynamo effect and the rotation.

Finally, in chapter 5, we investigated the diffusion-free scaling regime for rotating Rayleigh–Bénard convection between spherical shells. This regime is characterised by a bulk-dominated flow. While in planar geometry we have vertical columns forming between the hot and the cold surfaces, different configurations are obtained in spherical geometry. We identified three regions: I where the columns connect the hot and the cold surfaces, II where they are touching only the cold sphere, and III where they are so close to the sphere that they get almost disrupted. Possibly, the existence of configurations II and III (impossible in planar geometry), combined with the latitude-dependent Coriolis force, lead to the rise of diffusion free scaling even for parameters for which this scaling does not arise in planar geometry.

In this manuscript we showed some of the possible applications of this numerical scheme; we acknowledge that several other applications are available and many of them are currently subjects of investigation. For example, we are analysing how the radius ratio and the non-monotonicity of gravity profiles affect the onset of convection for systems such as the one described in chapter 3.



## APPENDIX A

# Harmonic analysis and spectrum

This appendix describes the spectral analysis procedure used in this study. For further reading on this topic, we refer to p.122-p.145 of [100].

### A.1 Fourier decomposition

Fourier transforms are a fundamental tool in mathematics and physics. A Fourier transform of a function of time is a (in general complex valued) function of frequency, and its magnitude or intensity gives information to the most *common* frequencies of the original function. Let  $f$  a periodic square-integrable function  $\hat{s} \in L^2(T)$ , with  $T$  being the unitary circumference. Then its Fourier series is

$$\sum_{n=-\infty}^{n=\infty} s(n)e^{int} \quad (\text{A.1})$$

where  $i$  is the imaginary unit and the Fourier coefficients  $s(n)$  are defined as

$$s(n) = \frac{1}{2\pi} \int_{-\pi}^{\pi} \hat{s}(t)e^{-int} dt = \frac{1}{2\pi} \int_{-T/2}^{T/2} \hat{s}(t)e^{-i2\pi nt/T} dt. \quad (\text{A.2})$$

The coefficients can be seen as discretized samplings of the Fourier transform at intervals  $1/T$ , so we can define the Fourier transform  $s(f)$  as

$$s(f) = \frac{1}{2\pi} \int_{\mathbb{R}} \hat{s}(t)e^{-ift} dt. \quad (\text{A.3})$$

### A.2 Spherical harmonic decomposition

Given a square-integrable function  $f : S^2 \rightarrow \mathbb{C}$  on the unit sphere  $S^2$  its spherical harmonic decomposition can be written as

$$f(\phi, \theta) = \sum_{l=0}^{\infty} \sum_{m=-l}^l C_l^m Y_l^m(\phi, \theta) \quad (\text{A.4})$$

where  $Y_l^m(\phi, \theta)$  is the spherical harmonic of degree  $l$  and order  $m$  (which represent the wavenumber along a meridian and the equatorial plane), and  $C_l^m$  its

coefficient, and the expansion holds in the sense of convergence in  $L^2$  of the sphere.  $Y_l^m(\phi, \theta)$  can be defined in terms of associated Legendre polynomials  $P_l^m$  by

$$Y_l^m(\phi, \theta) = \sqrt{\frac{(2l+1)(l-m)!}{4\pi(l+m)!}} P_l^m(\cos\phi) e^{im\theta}, \quad (\text{A.5})$$

where  $P_l^m(x)$  satisfies the general Legendre equation

$$\frac{d}{dx} \left[ (1-x^2) \frac{d}{dx} P_l^m(x) \right] + \left[ l(l+1) - \frac{m^2}{1-x^2} \right] P_l^m(x) = 0. \quad (\text{A.6})$$

For orthonormalised harmonics, as the one defined in equation (A.5), the coefficients can be computed by

$$C_l^m = \int_{\Omega} f(\phi, \theta) Y_l^{m*}(\phi, \theta) d\Omega \quad (\text{A.7})$$

where  $\Omega$  is the solid angle.

This tool has been used in this study to perform a spectral analysis of the averaged square temperature  $T^2(\phi, \theta)$  to better characterize the fluid behaviour for the various simulations. Coefficients of equation (A.7) are obtained by using the SPHEREPACK library [1]. In the analysis, the averaged value of coefficients has been used, i.e.  $C_l = c_0 \langle \sum_{m=-l}^l C_l^m \rangle$  (with  $c_0$  normalization factor) and

$$C_m = \frac{1}{n-m+1} \langle \sum_{l=m}^n C_{l,m} \rangle, \quad n = \min(N_\varphi - 1, (N_\theta + 1)/2) \quad (\text{A.8})$$

(the angular parenthesis indicate time and radial average).

In the manuscript we use the terminology *main-degree* when referring to  $l_m = \arg \max_{l \neq 0} (C_l)$ , and *main-order* for  $m_m = \arg \max_{m \neq 0} (C_m)$ .

## APPENDIX B

# Transformation of gravity center to any random point

The two-step transformation of a vector **GP** in Cartesian coordinate  $xyz$  to spherical coordinate  $\varphi\theta r$  ( $x''y''z''$ ) is shown in figure B.1. A random fixed point  $G(x_G, y_G, z_G)$  is representing the gravity center location. The other random point  $P$  with  $P(r \sin \varphi \cos \theta, r \sin \varphi \sin \theta, r \cos \varphi)$  is a moving point representing a fluid parcel. Initially, both  $P$  and  $G$  are in Cartesian coordinates  $xyz$ . Using two steps we will transfer **GP** to spherical coordinates  $\varphi\theta r$  ( $x''y''z''$ ).

(1) Rotating  $xyz$  to  $x'y'z'$  about  $z$  by an angle  $\theta$  using the right-hand side rule. The corresponding rotation matrix is

$$R_z(\theta) = \begin{bmatrix} \cos \theta & -\sin \theta & 0 \\ \sin \theta & \cos \theta & 0 \\ 0 & 0 & 1 \end{bmatrix} \quad (\text{B.1})$$

(2) Rotating  $x'y'z'$  to  $x''y''z''$  about  $y'$  by an angle  $\varphi$  using the right-hand side

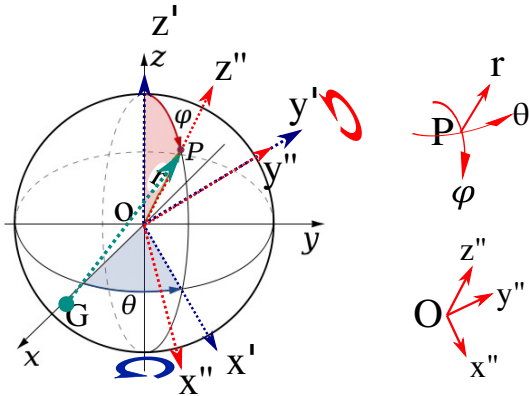


Figure B.1: Schematic figure of the two-step transformation of a vector **GP** in Cartesian coordinate  $xyz$  to spherical coordinate  $\varphi\theta r$  ( $x''y''z''$ ) frame. Circular arrows about  $z'$  – axis and  $y'$  – axis show rotating axis.

rule. The corresponding rotation matrix is

$$R_y(\varphi) = \begin{bmatrix} \cos \varphi & 0 & \sin \varphi \\ 0 & 1 & 0 \\ -\sin \varphi & 0 & \cos \varphi \end{bmatrix} \quad (\text{B.2})$$

After the above two steps we obtain that  $x''y''z''$  overlaps with  $\varphi\theta r$ . The transformation matrix  $\mathcal{M}_{\theta\varphi}$  from  $\mathbf{GP}_{xyz}$  to  $\mathbf{GP}_{x''y''z''}$  is defined by

$$\begin{aligned} \mathcal{M}_{\theta\varphi} &= R_z(\theta) \times R_y(\varphi) = \begin{bmatrix} \cos \theta & -\sin \theta & 0 \\ \sin \theta & \cos \theta & 0 \\ 0 & 0 & 1 \end{bmatrix} \begin{bmatrix} \cos \varphi & 0 & \sin \varphi \\ 0 & 1 & 0 \\ -\sin \varphi & 0 & \cos \varphi \end{bmatrix} \\ &= \begin{bmatrix} \cos \varphi \cos \theta & -\sin \theta & \sin \varphi \cos \theta \\ \cos \varphi \sin \theta & \cos \theta & \sin \varphi \sin \theta \\ -\sin \varphi & 0 & \cos \varphi \end{bmatrix} \end{aligned} \quad (\text{B.3})$$

In the Cartesian coordinate frame  $\mathbf{GP}_{xyz} = (r \sin \varphi \cos \theta - x_G, r \sin \varphi \sin \theta - y_G, r \cos \varphi - z_G)$ . Using the above transformations we find that  $\mathbf{GP}$  in spherical coordinate  $x''y''z''$  is:

$$\begin{aligned} \mathbf{GP}_{x''y''z''} &= \mathbf{GP}_{xyz} \times \mathcal{M}_{\theta\varphi} = (-x_G \cos \varphi \cos \theta - y_G \cos \varphi \sin \theta + z_G \sin \varphi, \\ &\quad x_G \sin \theta - y_G \cos \theta, \\ &\quad r - x_G \sin \varphi \cos \theta - y_G \sin \varphi \sin \theta - z_G \cos \varphi) \end{aligned} \quad (\text{B.4})$$

In the dimensionless equations for the velocity  $\mathbf{u}$ , the buoyancy term is given by  $gT\mathbf{GP}/L_{GP}$ , where

$$L_{GP} = |\mathbf{GP}| = \sqrt{(r \sin \varphi \cos \theta - x_G)^2 + (r \sin \varphi \sin \theta - y_G)^2 + (r \cos \varphi - z_G)^2} \quad (\text{B.5})$$

Three components in  $\hat{\varphi}$ ,  $\hat{\theta}$  and  $\hat{r}$  directions can be decomposed as follows

$$\begin{aligned} C_{g,\theta} &= (x_G \sin \theta - y_G \cos \theta)/L_{GP} \\ C_{g,r} &= (r - x_G \sin \varphi \cos \theta - y_G \sin \varphi \sin \theta - z_G \cos \varphi)/L_{GP} \\ C_{g,\varphi} &= (-x_G \cos \varphi \cos \theta - y_G \cos \varphi \sin \theta + z_G \sin \varphi)/L_{GP} \end{aligned} \quad (\text{B.6})$$

Specifically for natural convection in  $-\hat{z}$  direction in Cartesian coordinates, the gravity center is  $G(x_G = 0, y_G = 0, z_G = -\infty)$  so that we can get the three components  $C_{g,i} = (0, -\cos \varphi, \sin \varphi)$ ,  $i=1, 2$  and  $3$ . The same expression is used in [95].

## APPENDIX C

# Supporting Information for Chapter 5

### C.1 *Simulation details*

Table C.1: Simulation details. We use the conduction state  $T(\theta, r, \varphi) = T_c(r)$  and  $\mathbf{u} = 0$  as the initial conditions for the simulations. Simulations of 1 – 94 are run at  $Pr = 1$ ,  $\eta = 0.6$  and  $g \sim (r_o/r)^{n_g}$  with  $n_g = 2$ . Simulations of 95 – 111 are run at  $Pr = 1$ ,  $\eta = 0.35$  and  $n_g = -1$ . The columns from left to right indicate: case number, Rayleigh number  $Ra$ , Rossby number  $Ro$ , the number of grid points in the longitudinal, radial, and co-latitudinal direction  $N_\theta \times N_r \times N_\varphi$ . A rotational symmetry order  $n_s$  is applied to reduce computational costs, indicating the longitude of the computational domain as  $2\pi/n_s$ . The average heat transfer  $Nu$  across the inner and the outer sphere, and the regional heat transfer across the outer sphere  $Nu_{I,II,III}$  (see figure 3(b) of the paper). Note that region II and III are only defined when a maximum prograde velocity is identified.

	$Ra$	$Ro$	$N_\theta \times N_r \times N_\varphi$	$n_s$	$Nu$	$Nu_I$	$Nu_{II}$	$Nu_{III}$	$\varphi_2$
$Ek = 1 \times 10^{-2}$ , $\eta = 0.6$ , $n_g = 2$									
1	$2.5 \times 10^3$	0.25	$257 \times 71 \times 161$	1	1.058	1.029	–	–	–
2	$3 \times 10^3$	0.27	$257 \times 71 \times 161$	1	1.200	1.026	–	–	–
3	$5 \times 10^3$	0.35	$257 \times 71 \times 161$	1	1.566	1.050	–	–	–
4	$7 \times 10^3$	0.42	$257 \times 71 \times 161$	1	1.703	1.242	–	–	–
5	$1 \times 10^4$	0.50	$257 \times 71 \times 161$	1	2.036	1.662	–	–	–
6	$1.5 \times 10^4$	0.61	$257 \times 71 \times 161$	1	2.390	2.205	–	–	–
7	$2 \times 10^4$	0.71	$257 \times 71 \times 161$	1	2.637	2.521	–	–	–
8	$3 \times 10^4$	0.87	$257 \times 71 \times 161$	1	3.050	2.952	–	–	–
9	$5 \times 10^4$	1.12	$257 \times 71 \times 161$	1	3.661	3.443	–	–	–
10	$7 \times 10^4$	1.32	$257 \times 71 \times 161$	1	4.080	3.710	–	–	–
11	$1 \times 10^5$	1.58	$401 \times 81 \times 257$	1	4.566	4.055	–	–	–
12	$1.5 \times 10^5$	1.94	$401 \times 81 \times 257$	1	5.155	4.504	–	–	–
13	$2 \times 10^5$	2.24	$401 \times 81 \times 257$	1	5.608	4.749	–	–	–
14	$3 \times 10^5$	2.74	$401 \times 81 \times 257$	1	6.335	5.378	–	–	–

15	$5 \times 10^5$	3.54	$401 \times 81 \times 257$	1	7.322	6.098	—	—	—
16	$7 \times 10^5$	4.18	$401 \times 81 \times 257$	1	8.074	6.745	—	—	—
17	$1 \times 10^6$	5.00	$401 \times 81 \times 257$	1	8.952	7.490	—	—	—
18	$3 \times 10^6$	8.66	$601 \times 101 \times 401$	1	12.251	10.685	—	—	—
$Ek = 3 \times 10^{-3}, \eta = 0.6, n_g = 2$									
19	$6 \times 10^3$	0.12	$257 \times 71 \times 161$	1	1.000	1.030	—	—	—
20	$7 \times 10^3$	0.13	$257 \times 71 \times 161$	1	1.105	1.020	—	—	—
21	$1 \times 10^4$	0.15	$257 \times 71 \times 161$	1	1.297	1.007	—	—	—
22	$1.5 \times 10^4$	0.18	$257 \times 71 \times 161$	1	1.534	1.004	—	—	—
23	$2 \times 10^4$	0.21	$257 \times 71 \times 161$	1	1.734	1.049	—	—	—
24	$3 \times 10^4$	0.26	$257 \times 71 \times 161$	1	2.164	1.517	—	—	—
25	$4 \times 10^4$	0.30	$257 \times 71 \times 161$	1	2.571	2.211	—	—	—
26	$5 \times 10^4$	0.34	$257 \times 71 \times 161$	1	2.895	2.781	—	—	—
27	$6 \times 10^4$	0.37	$257 \times 71 \times 161$	1	3.157	3.223	—	—	—
28	$8 \times 10^4$	0.42	$257 \times 71 \times 161$	1	3.577	3.884	—	—	—
29	$1 \times 10^5$	0.47	$321 \times 91 \times 201$	1	3.895	4.334	—	—	—
30	$2 \times 10^5$	0.67	$321 \times 91 \times 201$	1	5.021	5.634	—	—	—
31	$5 \times 10^5$	1.06	$321 \times 91 \times 201$	1	6.916	7.127	—	—	—
32	$9 \times 10^5$	1.42	$451 \times 101 \times 301$	1	8.347	8.226	—	—	—
33	$1.3 \times 10^6$	1.71	$451 \times 101 \times 301$	1	9.421	8.973	—	—	—
34	$2.5 \times 10^6$	2.37	$451 \times 101 \times 301$	1	11.549	10.267	—	—	—
35	$4 \times 10^6$	3.00	$301 \times 121 \times 401$	2	13.238	11.788	—	—	—
36	$6 \times 10^6$	3.67	$301 \times 121 \times 401$	2	14.960	13.580	—	—	—
37	$8 \times 10^6$	4.24	$301 \times 121 \times 401$	2	16.369	15.571	—	—	—
$Ek = 1 \times 10^{-4}, \eta = 0.6, n_g = 2$									
38	$2 \times 10^5$	0.02	$145 \times 73 \times 217$	4	1.008	1.021	—	—	—
39	$3 \times 10^5$	0.03	$145 \times 73 \times 217$	4	1.077	1.018	—	—	—
40	$4 \times 10^5$	0.03	$145 \times 73 \times 217$	4	1.119	1.012	—	—	—
41	$6 \times 10^5$	0.04	$145 \times 73 \times 217$	4	1.250	1.008	1.096	1.426	0.92
42	$1 \times 10^6$	0.05	$257 \times 81 \times 401$	4	1.488	1.009	1.269	1.807	1.00
43	$1.5 \times 10^6$	0.06	$257 \times 81 \times 401$	4	2.317	1.070	1.770	2.999	0.97
44	$2 \times 10^6$	0.07	$257 \times 81 \times 401$	4	3.233	1.420	2.680	4.261	1.01
45	$3 \times 10^6$	0.09	$257 \times 81 \times 401$	4	5.038	3.318	4.472	5.992	0.98
46	$4 \times 10^6$	0.10	$257 \times 81 \times 401$	4	6.613	5.844	6.184	7.278	1.00
47	$5 \times 10^6$	0.11	$257 \times 81 \times 401$	4	7.949	8.242	7.414	8.367	1.05
48	$6 \times 10^6$	0.12	$257 \times 81 \times 401$	4	9.060	10.233	8.572	9.147	1.04
49	$7 \times 10^6$	0.13	$257 \times 81 \times 401$	4	9.996	11.913	9.328	9.941	1.08
50	$8 \times 10^6$	0.14	$257 \times 81 \times 401$	4	10.801	13.309	10.246	10.532	1.07
51	$1 \times 10^7$	0.16	$257 \times 81 \times 401$	4	12.110	15.364	11.286	11.608	1.11
52	$2 \times 10^7$	0.22	$257 \times 101 \times 401$	4	16.381	21.292	15.746	15.167	1.10
53	$3 \times 10^7$	0.27	$257 \times 101 \times 401$	4	19.410	25.163	18.848	18.105	1.08
$Ek = 3 \times 10^{-5}, \eta = 0.6, n_g = 2$									
54	$8 \times 10^5$	0.013	$145 \times 73 \times 217$	4	1.011	1.022	—	—	—

55	$1 \times 10^6$	0.015	$145 \times 73 \times 217$	4	1.039	1.020	—	—	—
56	$1.5 \times 10^6$	0.018	$145 \times 73 \times 217$	4	1.090	1.016	—	—	—
57	$2 \times 10^6$	0.021	$145 \times 73 \times 217$	4	1.148	1.011	—	—	—
58	$3 \times 10^6$	0.026	$145 \times 73 \times 217$	4	1.251	1.008	1.104	1.425	0.921
59	$4 \times 10^6$	0.030	$145 \times 73 \times 217$	4	1.418	1.002	1.185	1.710	0.968
60	$5 \times 10^6$	0.034	$289 \times 73 \times 401$	4	1.604	1.006	1.251	1.985	0.961
61	$6 \times 10^6$	0.037	$289 \times 73 \times 401$	4	1.978	1.014	1.490	2.591	0.993
62	$7 \times 10^6$	0.040	$289 \times 73 \times 401$	4	2.435	1.061	1.785	3.316	1.006
63	$8 \times 10^6$	0.042	$289 \times 81 \times 401$	4	2.905	1.148	2.062	3.838	0.940
64	$1 \times 10^7$	0.047	$289 \times 81 \times 401$	4	3.865	1.479	2.959	5.351	1.026
65	$1.3 \times 10^7$	0.054	$289 \times 81 \times 401$	4	5.268	2.495	4.302	7.067	1.050
66	$1.5 \times 10^7$	0.058	$289 \times 81 \times 401$	4	6.251	3.514	5.245	8.221	1.078
67	$2 \times 10^7$	0.067	$289 \times 103 \times 433$	4	8.491	6.657	7.414	10.115	1.066
68	$2.5 \times 10^7$	0.075	$289 \times 103 \times 433$	4	10.599	9.998	9.540	11.863	1.081
69	$3 \times 10^7$	0.082	$289 \times 103 \times 433$	4	12.294	12.861	11.164	13.391	1.125
70	$4 \times 10^7$	0.095	$321 \times 103 \times 481$	4	15.054	16.930	14.064	15.427	1.120
71	$5 \times 10^7$	0.106	$321 \times 103 \times 481$	4	17.148	19.940	15.847	17.549	1.158
$Ek = 1 \times 10^{-5}, \eta = 0.6, n_g = 2$									
72	$1 \times 10^7$	0.016	$201 \times 91 \times 401$	8	1.190	1.007	—	—	—
73	$2 \times 10^7$	0.022	$201 \times 91 \times 401$	8	1.554	1.001	1.280	1.987	1.059
74	$3 \times 10^7$	0.027	$201 \times 91 \times 401$	8	2.537	1.097	1.780	3.449	0.988
75	$4 \times 10^7$	0.032	$201 \times 91 \times 401$	8	3.784	1.363	2.750	5.607	1.076
76	$5 \times 10^7$	0.035	$201 \times 91 \times 401$	8	5.097	1.897	3.754	7.169	1.055
77	$6 \times 10^7$	0.039	$241 \times 96 \times 481$	8	6.296	2.757	4.970	9.120	1.132
78	$7 \times 10^7$	0.042	$241 \times 96 \times 481$	8	7.644	3.995	6.166	10.746	1.129
79	$8 \times 10^7$	0.045	$241 \times 96 \times 481$	8	9.114	5.585	7.472	12.311	1.119
80	$1 \times 10^8$	0.050	$289 \times 115 \times 577$	8	11.697	9.153	10.089	14.710	1.138
81	$1.5 \times 10^8$	0.061	$289 \times 115 \times 577$	8	16.815	16.786	14.865	18.800	1.138
82	$2 \times 10^8$	0.071	$325 \times 130 \times 649$	8	19.973	19.499	18.912	21.855	1.114
$Ek = 3 \times 10^{-6}, \eta = 0.6, n_g = 2$									
83	$3 \times 10^7$	0.008	$241 \times 97 \times 481$	8	1.101	1.009	—	—	—
84	$7 \times 10^7$	0.013	$241 \times 97 \times 481$	8	1.312	1.022	—	—	—
85	$1.1 \times 10^8$	0.016	$241 \times 97 \times 481$	8	1.770	1.006	1.364	2.332	1.021
86	$1.5 \times 10^8$	0.018	$289 \times 115 \times 577$	8	2.518	1.134	1.798	3.527	1.062
87	$1.8 \times 10^8$	0.020	$325 \times 131 \times 649$	8	3.322	1.297	2.327	4.970	1.097
88	$2 \times 10^8$	0.021	$325 \times 131 \times 649$	8	3.928	1.419	2.689	6.035	1.102
89	$2.5 \times 10^8$	0.024	$385 \times 155 \times 769$	8	5.273	1.910	3.694	7.840	1.076
90	$3 \times 10^8$	0.026	$385 \times 155 \times 769$	8	6.449	2.551	4.930	10.193	1.174
91	$4 \times 10^8$	0.030	$433 \times 173 \times 867$	8	9.537	4.694	7.524	14.390	1.181
92	$5 \times 10^8$	0.034	$433 \times 173 \times 867$	8	12.353	7.674	10.293	18.251	1.237
93	$6 \times 10^8$	0.037	$433 \times 173 \times 867$	8	16.036	12.334	13.775	20.935	1.229
94	$7 \times 10^8$	0.040	$433 \times 173 \times 867$	8	18.554	13.882	15.994	24.444	1.246

$Ek = 1 \times 10^{-5}, \eta = 0.35, n_g = -1$										
95	$2 \times 10^7$	0.022	$301 \times 73 \times 201$	2	1.101	1.010	—	—	—	—
96	$3 \times 10^7$	0.027	$301 \times 73 \times 201$	2	1.224	1.010	—	—	—	—
97	$4 \times 10^7$	0.032	$301 \times 73 \times 201$	2	1.360	1.011	—	—	—	—
98	$5 \times 10^7$	0.035	$301 \times 73 \times 201$	2	1.503	1.010	—	—	—	—
99	$6 \times 10^7$	0.039	$301 \times 73 \times 201$	2	1.639	1.012	—	—	—	—
100	$7 \times 10^7$	0.042	$451 \times 93 \times 301$	2	1.793	1.011	—	—	—	—
101	$8 \times 10^7$	0.045	$451 \times 93 \times 301$	2	1.909	1.001	—	—	—	—
102	$9 \times 10^7$	0.047	$451 \times 93 \times 301$	2	2.168	1.014	—	—	—	—
103	$1 \times 10^8$	0.050	$451 \times 93 \times 301$	2	2.436	1.022	1.769	4.223	1.256	
104	$1.4 \times 10^8$	0.059	$451 \times 93 \times 301$	2	3.458	1.149	2.186	6.567	1.250	
105	$1.8 \times 10^8$	0.067	$451 \times 93 \times 301$	2	4.844	1.874	3.096	9.110	1.247	
106	$2 \times 10^8$	0.071	$451 \times 93 \times 301$	2	5.587	2.666	3.591	9.924	1.229	
107	$2.5 \times 10^8$	0.079	$541 \times 103 \times 361$	2	7.234	5.701	4.881	11.187	1.193	
108	$3 \times 10^8$	0.087	$541 \times 103 \times 361$	2	9.043	10.791	6.546	12.822	1.203	
109	$4 \times 10^8$	0.10	$541 \times 103 \times 361$	2	12.029	18.876	9.546	14.401	1.216	
110	$6 \times 10^8$	0.122	$541 \times 103 \times 361$	2	17.171	27.367	15.087	18.196	1.244	
111	$8 \times 10^8$	0.141	$601 \times 103 \times 361$	2	21.525	31.511	20.098	23.118	1.246	

## C.2 Grid independence and longitudinal domain size

A grid resolution study for case No.76 with  $n_s = 8$  is presented in figure C.1. In rapidly rotating spherical Rayleigh-Bénard (RB) flow, the convective columns are with length scale  $Ek^{1/3}d$  [50], distributed along the longitudinal direction. This explains the large number of grids in the longitudinal direction, which is proportional to  $Ek^{1/3}$ [50]. In our numerical scheme the  $Nu$  number is sensitive to the grid resolution. The effect of the grid resolution in the longitude, radial, and co-latitude direction is shown in figure C.1(a-c). We also verified to convergence by increasing the resolution in all directions simultaneously, i.e. from  $201 \times 91 \times 401$  ( $Nu = 5.097$ ) to  $251 \times 111 \times 451$  ( $Nu = 5.103$ ). Furthermore, we verified that the temperature ( $T_{rms}$ ) and velocity ( $u_{r,rms}$ ) root-mean-square profiles, which are more sensitive to the grid resolution, are fully converged. Overall, the tests confirm that  $N_\theta \times N_r \times N_\varphi = 201 \times 91 \times 401$  is sufficient resolution for case No.76. The resolution of the other cases is adjusted accordingly.

[5] found that the critical azimuthal wavenumber is nearly independent of assumed longitudinal symmetry up to  $n_s = 8$ . We have verified that the heat transfer does not depend on the longitudinal symmetry up to  $n_s = 8$ . Moreover, figure C.2 shows that the first order and second order temperature statistics are independent to  $n_s$ . Therefore, we use  $n_s$  up to eight for high rotation rates to reduce computational cost.

For case No.76 used for Figure 3(c) in the paper, we observe the onset of vertically aligned vortices in the region I, which are “cellular” convective structures (we refer to the review paper [10] about the flow morphology). These cellars result in regular oscillations of  $Nu(\varphi)$  close to the poles. To exclude that the

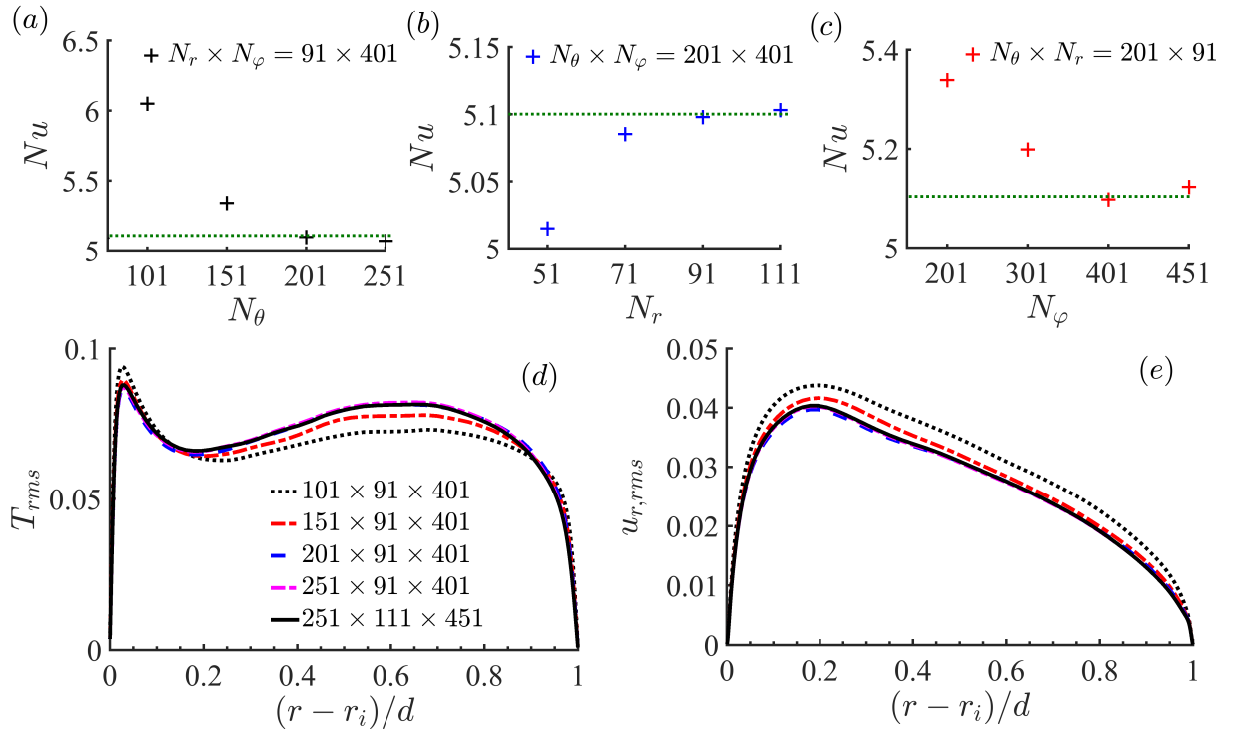


Figure C.1: Grid convergence test for case No.76.  $Nu$  as function of (a) the longitudinal number of grid point  $N_\theta$ ; (b) the radial number of grid points  $N_r$ ; (c) and the co-latitudinal number of grid points  $N_\varphi$ . The dotted line in (a-c) indicates  $Nu = 5.103$  obtained using  $N_\theta \times N_r \times N_\varphi = 251 \times 111 \times 451$ . (d,e) Corresponding  $T_{rms}$  and  $u_{r,rms}$  profiles as a function of radial direction, which show that higher order statistics are also converged.

oscillations are caused by numerical instabilities we perform two additional simulations, one with a finer mesh in the co-latitudinal direction, and one with a smaller CFL number. Figure C.3 shows that the  $Nu$  profiles obtained from these additional cases agrees excellently with standard case No.76, which confirms the accuracy of the results.

### C.3 Line Integral Convolution for spherical surfaces

Line integral convolution (LIC) is a technique introduced by [24] for generating texture from vector data as shown in figure 3(b) in the paper. This technique was initially dedicated to a 2D vector on a flat surface, as shown in figure C.4. The streaking patterns follow vector field tangents. Afterwards it has been extended to volume and arbitrary surfaces. For Figure 3(b) in the paper, we use a 3D vector field projection onto a spherical surface based on triangle tiling. An excellent technical and mathematical description of this approach can, for example, be found in section 3.4 of [67].

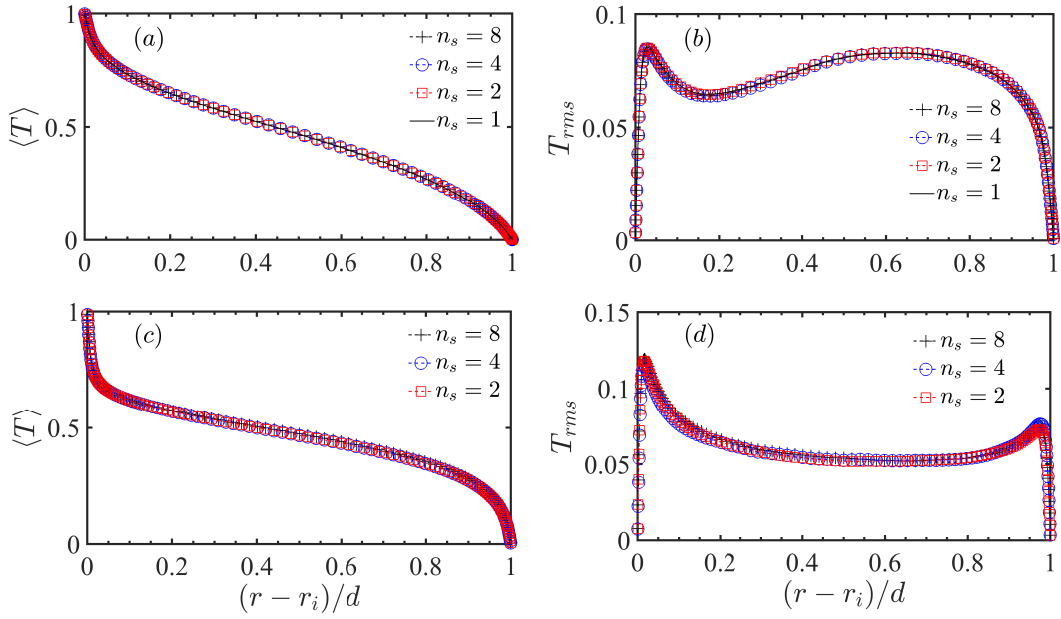


Figure C.2: Number of rotational symmetry order  $n_s$  tests for  $\langle T \rangle$  (a,c) and  $\langle T_{rms} \rangle$  (b,d) as a function of radial direction for case No.76 (a,b) and case No.80 (c,d).

#### C.4 Diffusive free region for $\eta = 0.35$ and $n_g = -1$

The temperature fluctuation  $T'$  in the vicinity of the outer radial surface in figure C.5(a) clearly shows three distinct flow regions from the pole to the equator. The  $Nu$  and  $Nu_{II}$  are shown in figure C.5(b). Again we find the diffusion-free scaling is much more pronounced in region II, similar to what we report for  $\eta = 0.6$  and  $n_g = 2$ . This confirms that the main findings are independent of the selected  $\eta$  and gravity profile.

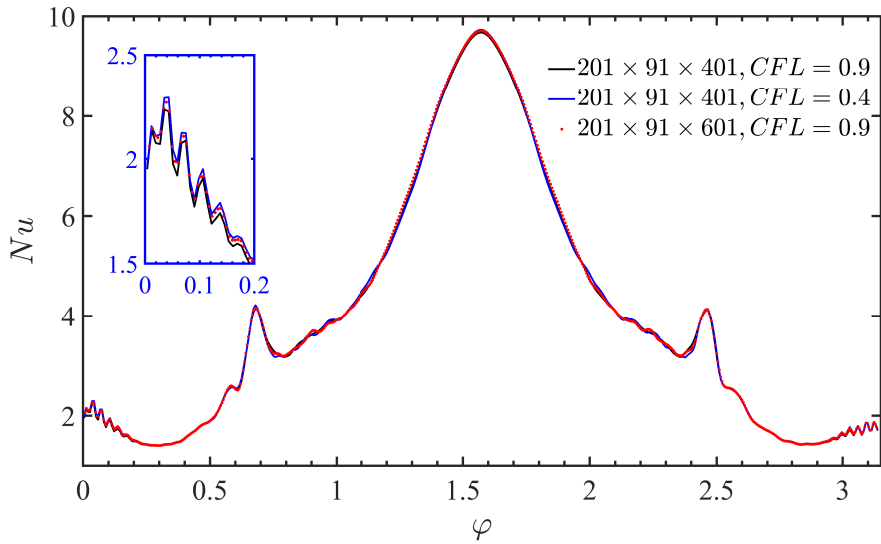


Figure C.3: Resolution and CFL number tests for case No.76 of  $Ek = 1 \times 10^{-5}$ ,  $Ra = 5 \times 10^7$ . Time and azimuthal averaged  $Nu$  as function of the co-latitude  $\varphi$  on the outer sphere.

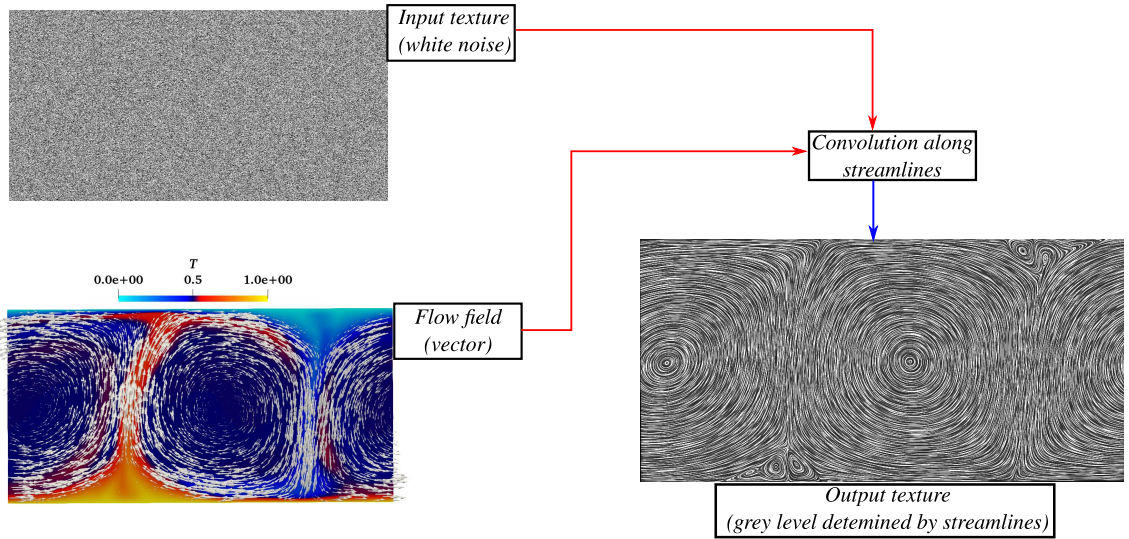


Figure C.4: Schematic process of line integral convolution (LIC) computation for a 2D non-rotating RB flow:  $\{\text{vector field} \rightarrow \text{streamline}\} + \{\text{input texture (white noise)}\} \rightarrow \{\text{output texture (pixel grey level determined by the streamline)}\}$ .

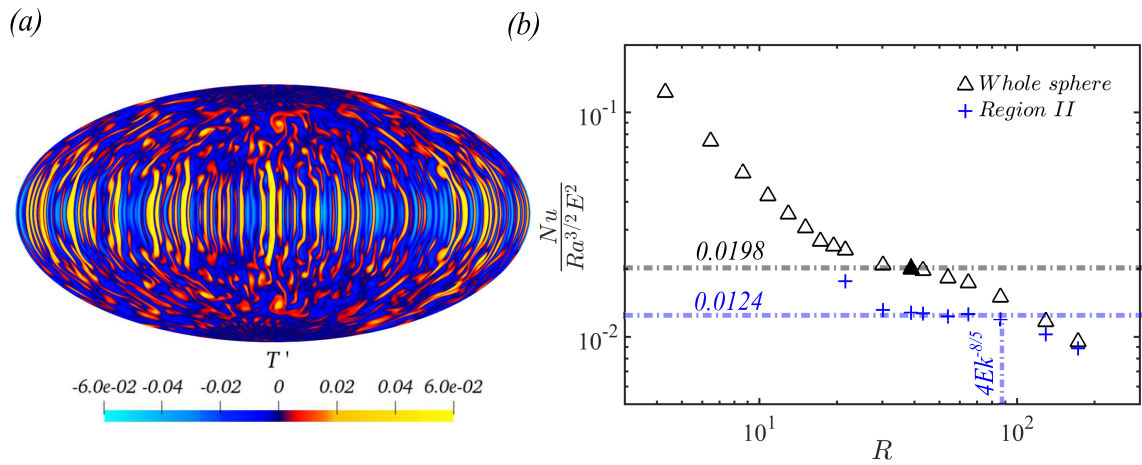


Figure C.5: (a) Temperature fluctuation at the outer thermal boundary layer displayed in a Hammer projection for case No.105, corresponding to the filled-in symbol in (b). (b)  $Nu$  integration over the whole sphere and in region II on the outer sphere compensated by  $R^{-3/2}$  and as a function of  $R \equiv RaEk^{4/3}$ .



# Bibliography

- [1] J. C. ADAMS AND P. N. SWARZTRAUBER, *Spherepack 3.0: A model development facility*, Mon. Weather Rev., 127 (1999), pp. 1872–1878.
- [2] G. AHLERS, S. GROSSMANN, AND D. LOHSE, *Heat transfer and large scale dynamics in turbulent Rayleigh-Bénard convection*, Rev. Mod. Phys., 81 (2009), pp. 503–537.
- [3] G. AHLERS, S. GROSSMANN, AND D. LOHSE, *Heat transfer and large scale dynamics in turbulent Rayleigh-Bénard convection*, Rev. Mod. Phys., 81 (2009), pp. 503–537.
- [4] A. G. AKSENOK, A. V. BABAKOV, AND V. M. CHECHETKIN, *Mathematical simulation of vortex structures in rapidly rotating astrophysical objects*, Comput. Math. and Math. Phys., 58 (2018), pp. 1287–1293.
- [5] F. M. AL-SHAMALI, M. H. HEIMPEL, AND J. M. AURNOU, *Varying the spherical shell geometry in rotating thermal convection*, Geophys. Astrophys. Fluid Dyn., 98 (2004), pp. 153–169.
- [6] T. ALBOUSSIÈRE, R. DEGUEN, AND M. MELZANI, *Melting-induced stratification above the Earth’s inner core due to convective translation*, Nature, 466 (2010), pp. 744–747.
- [7] K. ARAKI, J. MIZUSHIMA, AND S. YANASE, *Thermal instability of a fluid in a spherical shell with thin layer approximation analysis*, Journal of the Physical Society of Japan, 63 (1994), pp. 2123–2132.
- [8] J. AUBERT, J. AURNOU, AND J. WICHT, *The magnetic structure of convection-driven numerical dynamos*, Geophys. J. Int., 172 (2008), pp. 945–956.
- [9] J. AUBERT, T. GASTINE, AND A. FOURNIER, *Spherical convective dynamos in the rapidly rotating asymptotic regime*, J. Fluid Mech., 813 (2017), p. 558–593.
- [10] J. M. AURNOU, M. A. CALKINS, J. S. CHENG, K. JULIEN, E. M. KING, D. NIEVES, K. M. SODERLUND, AND S. STELLMACH, *Rotating convective turbulence in Earth and planetary cores*, Phys. Earth Planet. Inter., 246 (2015), pp. 52–71.

- [11] J. M. AURNOU AND P. L. OLSON, *Strong zonal winds from thermal convection in a rotating spherical shell*, Geophys. Res. Lett., 28 (2001), pp. 2557–2559.
- [12] F. AUTERI AND L. QUARTAPELLE, *Navier–stokes spectral solver in a sphere*, J. of Comput. Phys, 228 (2009), pp. 7197–7214.
- [13] R. AVILA, A. CABELLO-GONZÁLEZ, AND E. RAMOS, *A linear stability analysis of thermal convection in spherical shells with variable radial gravity based on the tau–chebyshev method*, International journal of heat and fluid flow, 44 (2013), pp. 495–508.
- [14] G. K. BATCHELOR, *An introduction to fluid mechanics*, Cambridge University Press, 615 (1967).
- [15] R. M. BEAM AND R. F. WARMING, *An implicit finite-difference algorithm for hyperbolic systems in conservation–law form*, J. Comput. Phys, 22 (1976), pp. 87–110.
- [16] D. BERCOVICI, G. SCHUBERT, AND G. A. GLATZMAIER, *Three-dimensional spherical models of convection in the earth’s mantle*, Science, 244 (1989), pp. 950–955.
- [17] E. BISHOP, L. MACK, AND J. SCANLAN, *Heat transfer by natural convection between concentric spheres*, Int. J. Heat Mass Transfer, 9 (1966), pp. 649–662.
- [18] P. BODENHEIMER, G. P. LAUGHLIN, M. RÓZYCKA, AND H. W. YORKE, *Numerical methods for astrophysics: An introduction*, Taylor & Francis, (2007), p. 352.
- [19] B. J. BOERSMA, G. BRETHOUWER, AND F. T. M. NIEUWSTADT, *A numerical investigation on the effect of the inflow conditions on the self-similar region of a round jet*, Phys. of Fluids, 10 (1998), pp. 899–909.
- [20] F. BUSSE, *Differential rotation in stellar convection zones*, Astrophys. J., 159 (1970), p. 629.
- [21] ——, *Patterns of convection in spherical shells*, J. Fluid Mech., 72 (1975), pp. 67–85.
- [22] F. H. BUSSE, *Thermal instabilities in rapidly rotating systems*, J. Fluid Mech., 44 (1970), pp. 441–460.
- [23] ——, *A model of mean zonal flows in the major planets*, Geophys. Astrophys. Fluid Dyn., 23 (1983), pp. 153–174.
- [24] B. CABRAL AND L. C. LEEDOM, *Imaging vector fields using line integral convolution*, in Proceedings of the 20th annual conference on Computer graphics and interactive techniques, 1993, pp. 263–270.

- [25] H. CAO, R. K. YADAV, AND J. M. AURNOU, *Geomagnetic polar minima do not arise from steady meridional circulation*, Proc. Natl. Acad. Sci. U.S.A., 115 (2018), pp. 11186–11191.
- [26] S. CHANDRASEKHAR, *Hydrodynamic and Hydrodynamic Stability*, Oxford University Press, 1961.
- [27] J. S. CHENG, M. MADONIA, A. J. AGUIRRE GUZMÁN, AND R. P. J. KUNNEN, *Laboratory exploration of heat transfer regimes in rapidly rotating turbulent convection*, Phys. Rev. Fluids, 5 (2020), p. 113501.
- [28] J. S. CHENG, S. STELLMACH, A. RIBEIRO, A. GRANNAN, E. M. KING, AND J. M. AURNOU, *Laboratory-numerical models of rapidly rotating convection in planetary cores*, Geophys J Int, 201 (2015), pp. 1–17.
- [29] F. CHILLA AND J. SCHUMACHER, *New perspectives in turbulent Rayleigh-Bénard convection*, Eur. Phys. J. E, 35 (2012), p. 58.
- [30] C. P. CHIU AND W. R. CHEN, *Transient natural convection heat transfer between concentric and vertically eccentric spheres*, International journal of heat and mass transfer, 39 (1996), pp. 1439–1452.
- [31] U. R. CHRISTENSEN, *Zonal flow driven by strongly supercritical convection in rotating spherical shells*, J. Fluid Mech., 470 (2002), p. 115–133.
- [32] U. R. CHRISTENSEN AND J. AUBERT, *Scaling properties of convection-driven dynamos in rotating spherical shells and application to planetary magnetic fields*, Geophys. J. Int., 166 (2006), pp. 97–114.
- [33] H. CHU AND T. LEE, *Transient natural convection heat transfer between concentric spheres*, Int. J. Heat Mass Transfer, 36 (1993), pp. 3159–3170.
- [34] A. CONSTANTIN AND R. S. JOHNSON, *Steady large-scale ocean flows in spherical coordinates*, Oceanography, 31 (2018), pp. 42–50.
- [35] M. J. P. CULLEN, *Current progress and prospects in numerical techniques for weather prediction models*, J. of Comp. Phys, 50 (1983), pp. 1–37.
- [36] A. DAVAILLE, *Simultaneous generation of hotspots and superswells by convection in a heterogeneous planetary mantle*, Nature, 402 (1999), pp. 756–760.
- [37] A. A. DEHGHAN AND M. KHOSHAB, *Numerical simulation of buoyancy-induced turbulent flow between two concentric isothermal spheres*, Heat transfer engineering, 31 (2010), pp. 33–44.
- [38] F. DESCHAMPS, P. J. TACKLEY, AND T. NAKAGAWA, *Temperature and heat flux scalings for isoviscous thermal convection in spherical geometry*, Geophys. J. Int., 182 (2010), pp. 137–154.

- [39] B. DINTRANS, A. BRANDENBURG, Å. NORDLUND, AND R. F. STEIN, *Spectrum and amplitudes of internal gravity waves excited by penetrative convection in solar-type stars*, *Astronomy & Astrophysics*, 438 (2005), pp. 365–376.
- [40] R. E. ECKE AND J. J. NIEMELA, *Heat transport in the geostrophic regime of rotating Rayleigh-Bénard convection*, *Phys. Rev. Lett.*, 113 (2014), p. 114301.
- [41] J. C. M. EGGELS, F. UNGER, M. H. WEISS, J. WESTERWEEL, R. J. ADRIAN, R. FRIEDRICH, AND F. T. M. NIEUWSTADT, *Fully developed turbulent pipe flow: a comparison between direct numerical simulation and experiment*, *J. Fluid Mech.*, 268 (1994), pp. 175–210.
- [42] Y. FELDMAN AND T. COLONIUS, *On a transitional and turbulent natural convection in spherical shells*, *International Journal of Heat and Mass Transfer*, 64 (2013), pp. 514–525.
- [43] Y. FELDMAN, T. COLONIUS, M. T. PAUKEN, J. L. HALL, AND J. A. JONES, *Simulation and cryogenic experiments of natural convection for the titan montgolfiere*, *AIAA journal*, 50 (2012), pp. 2483–2491.
- [44] B. FORNBERG, *A pseudospectral approach for polar and spherical geometries*, *SIAM J. Sci. Comput.*, 16 (1995), pp. 1071–1081.
- [45] D. FULTZ, R. R. LONG, G. V. OWENS, W. BOHAN, R. KAYLOR, AND J. WEIL, *Studies of thermal convection in a rotating cylinder with some implications for large-scale atmospheric motions*, in *Studies of Thermal Convection in a Rotating Cylinder with Some Implications for Large-Scale Atmospheric Motions*, Springer, 1959, pp. 1–104.
- [46] B. FUTTERER, M. GELLERT, T. VON LARCHER, AND C. EGBERS, *Thermal convection in rotating spherical shells: An experimental and numerical approach within geoflow*, *Acta Astronautica*, 62 (2008), pp. 300–307.
- [47] B. FUTTERER, A. KREBS, A.-C. PLESA, F. ZAUSSINGER, R. HOLLERBACH, D. BREUER, AND C. EGBERS, *Sheet-like and plume-like thermal flow in a spherical convection experiment performed under microgravity*, *J. Fluid Mech.*, 735 (2013), p. 647–683.
- [48] V. K. GARG, *Natural convection between concentric spheres*, *Int. J. Heat Mass Transfer*, 35 (1992), pp. 1935–1945.
- [49] T. GASTINE, J. WICHT, AND J. M. AURNOU, *Turbulent Rayleigh-Bénard convection in spherical shells*, *J. Fluid Mech.*, 778 (2015), p. 721–764.
- [50] ——, *Scaling regimes in spherical shell rotating convection*, *J. Fluid Mech.*, 808 (2016), p. 690–732.

- [51] P. A. GILMAN, *Linear simulations of boussinesq convection in a deep rotating spherical shell*, J. of Atmos. Sci, 32 (1975), pp. 1331–1352.
- [52] ———, *Nonlinear dynamics of boussinesq convection in a deep rotating spherical shell–i*, Geophys. Astrophys. Fluid Dynamics, 8 (1977), pp. 93–135.
- [53] P. A. GILMAN, *Nonlinear dynamics of Boussinesq convection in a deep rotating spherical shell-I*, Geophys. Astrophys. Fluid Dyn., 8 (1977), pp. 93–135.
- [54] G. GLATZMAIER, *Numerical simulations of stellar convective dynamos. i. the model and method*, J. of Comp. Phys, 55 (1984), pp. 461–484.
- [55] G. A. GLATZMAIER, R. S. COE, L. HONGRE, AND P. H. ROBERTS, *The role of the Earth’s mantle in controlling the frequency of geomagnetic reversals*, Nature, 401 (1999), pp. 885–890.
- [56] G. A. GLATZMAIERS AND P. H. ROBERTS, *A three-dimensional self-consistent computer simulation of a geomagnetic field reversal*, Nature, 377 (1995), pp. 203–209.
- [57] P. M. GRESHO, *Incompressible fluid dynamics: Some fundamental formulations issues*, Annu. Rev. Fluid Mech, 23s (1991), pp. 413–453.
- [58] S. GROSSMANN AND D. LOHSE, *Scaling in thermal convection: a unifying theory*, J. Fluid Mech., 407 (2000), pp. 27–56.
- [59] ———, *Thermal convection for large prandtl numbers*, Phys. Rev. Lett., 86 (2001), pp. 3316–3319.
- [60] ———, *Multiple scaling in the ultimate regime of thermal convection*, Phys. Fluids, 23 (2011), p. 045108.
- [61] D. GUBBINS, B. SREENIVASAN, J. MOUND, AND S. ROST, *Melting of the Earth’s inner core*, Nature, 473 (2011), p. 361.
- [62] M. GURNIS, *Large-scale mantle convection and the aggregation and dispersal of supercontinents*, Nature, 332 (1988), pp. 695–699.
- [63] G. HADLEY, *Vi. concerning the cause of the general trade-winds*, Philosophical Transactions of the Royal Society of London, 39 (1735), pp. 58–62.
- [64] F. H. HARLOW AND J. E. WELCH, *Numerical calculation of times-dependent viscous incompressible flow of fluid with free surface*, Phys. of Fluids, 8 (1965), pp. 2182–2189.
- [65] J. E. HART, G. A. GLATZMAIER, AND J. TOOMRE, *Space-laboratory and numerical simulations of thermal convection in a rotating hemispherical shell with radial gravity*, Journal of Fluid Mechanics, 173 (1986), pp. 519–544.

- [66] D. M. HASSLER, I. E. DAMMASCH, P. LEMAIRE, P. BREKKE, W. CURDT, H. E. MASON, J.-C. VIAL, AND K. WILHELM, *Solar wind outflow and the chromospheric magnetic network*, Science, 283 (1999), pp. 810–813.
- [67] H. C. HEGE AND K. POLTHIER, *Visualization and mathematics III*, Springer Science & Business Media, 2013.
- [68] M. J. M. HILL, *Vi. on a spherical vortex*, Phil. Trans. Roy. Soc. A, 185 (1894), pp. 213–245.
- [69] S. HORN AND O. SHISHKINA, *Toroidal and poloidal energy in rotating Rayleigh–Bénard convection*, J. Fluid Mech., 762 (2015), pp. 232–255.
- [70] G. HOUSEMAN, *The dependence of convection planform on mode of heating*, Nature, 332 (1988), pp. 346–349.
- [71] F. P. INCROPERA, *Liquid cooling of electronic devices by single-phase convection*, vol. 3, Wiley-Interscience, 1999.
- [72] Y. IWASE AND S. HONDA, *An interpretation of the Nusselt-Rayleigh number relationship for convection in a spherical shell*, Geophys. J. Int., 130 (1997), pp. 801–804.
- [73] G. T. JARVIS, G. A. GLATZMAIERAND, AND V. I. VANGELOV, *Effects of curvature, aspect ratio and plan form in two-and three-dimensional spherical models of thermal convection*, Geophys. Astrophys. Fluid Dyn., 79 (1995), pp. 147–171.
- [74] C. A. JONES, *Planetary magnetic fields and fluid dynamos*, Annu. Rev. Fluid Mech., 43 (2011), pp. 583–614.
- [75] D. D. JOSEPH AND S. CARMI, *Subcritical convective instability part 2. spherical shells*, Journal of Fluid Mechanics, 26 (1966), pp. 769–777.
- [76] K. JULIEN, J. M. AURNOU, M. A. CALKINS, E. KNOBLOCH, P. MARTI, S. STELLMACH, AND G. M. VASIL, *A nonlinear model for rotationally constrained convection with Ekman pumping*, J. Fluid Mech., 798 (2016), pp. 50–87.
- [77] K. JULIEN, E. KNOBLOCH, A. M. RUBIO, AND G. M. VASIL, *Heat transport in low-Rossby-number Rayleigh–Bénard convection*, Phys. Rev. Lett., 109 (2012a), p. 254503.
- [78] K. JULIEN, A. M. RUBIO, I. GROOMS, AND E. KNOBLOCH, *Statistical and physical balances in low Rossby number Rayleigh–Bénard convection*, Geophys. Astrophys. Fluid Dyn., 106 (2012b), pp. 392–428.
- [79] A. KAGEYAMA AND S. KIDA, *A spectral method in spherical coordinates with coordinate singularity at the origin*, Research Report, NIFS-636 (2000).

- [80] A. KAGEYAMA, K. WATANABE, AND T. SATO, *Simulation study of a magnetohydrodynamic dynamo: Convection in a rotating spherical shell*, Physics of Fluids B, 5 (1993), pp. 2793–2805.
- [81] S. KIDA, *Stability of thermal convection in a rapidly rotating sphere*, J. of Phys. Soc. Jap, 63 (1994), pp. 2964–2973.
- [82] S. KIDA AND K. NAKAYAMA, *Helical flow structure in a precessing sphere*, J. of Phys. Soc. Jap, 77 (2008).
- [83] S. KIDA AND M. SHIMIZU, *A turbulent ring and dynamo in a precessing sphere*, J. of Phys, 318 (2011), p. 072031.
- [84] E. M. KING, S. STELLMACH, AND J. M. AURNOU, *Heat transfer by rapidly rotating Rayleigh–Bénard convection*, J. Fluid Mech., 691 (2012), pp. 568–582.
- [85] E. M. KING, S. STELLMACH, AND B. BUFFETT, *Scaling behaviour in Rayleigh–Bénard convection with and without rotation*, J. Fluid Mech., 717 (2013), pp. 449–471.
- [86] E. M. KING, S. STELLMACH, J. NOIR, U. HANSEN, AND J. M. AURNOU, *Boundary layer control of rotating convection systems*, Nature, 457 (2009), p. 301.
- [87] R. KISSMANN, J. KLEIMANN, B. KREBL, AND T. WIENGARTEN, *The cronos code for astrophysical magnetohydrodynamics*, The Astrophys. J. Supp. Series, 236 (2018).
- [88] H. KITAUCHI, K. ARAKI, AND S. KIDA, *Flow structure of thermal convection in a rotating spherical shell*, Nonlinearity, 10 (1997), pp. 885–904.
- [89] R. H. KRAICHNAN, *Turbulent thermal convection at arbitrary Prandtl number*, Phys. Fluids, 5 (1962), pp. 1374–1389.
- [90] P. K. KUNDU, I. M. COHEN, AND D. R. DOWLING, *Fluid mechanics*, 1990.
- [91] R. P. J. KUNNEN, *The geostrophic regime of rapidly rotating turbulent convection*, J. Turbul., (2021), pp. 1–30.
- [92] R. P. J. KUNNEN, R. OSTILLA-MÓNICO, E. P. VAN DER POEL, R. VERZICCO, AND D. LOHSE, *Transition to geostrophic convection: the role of the boundary conditions*, J. Fluid Mech., 799 (2016), pp. 413–432.
- [93] J. LI, T. SATO, AND A. KAGEYAMA, *Repeated and sudden reversals of the dipole field generated by a spherical dynamo action*, Science, 295 (2002), pp. 1887–1890.
- [94] C. LITHGOW-BERTELLONI AND P. G. SILVER, *Dynamic topography, plate driving forces and the African superswell*, Nature, 395 (1998), pp. 269–272.

- [95] M. LIU, C. BLOHM, C. EGBERS, P. WULF, AND H. RATH, *Taylor vortices in wide spherical shells*, Phys. Rev. Lett., 77 (1996), p. 286.
- [96] Y. LIU AND R. E. ECKE, *Heat transport scaling in turbulent Rayleigh-Bénard convection: effects of rotation and Prandtl number*, Phys. Rev. Lett., 79 (1997), p. 2257.
- [97] R. S. LONG, J. E. MOUND, C. J. DAVIES, AND S. M. TOBIAS, *Scaling behaviour in spherical shell rotating convection with fixed-flux thermal boundary conditions*, J. Fluid Mech., 889 (2020), p. A7.
- [98] R. E. LYNCH, J. R. RICE, AND D. H. THOMAS, *Tensor product analysis of partial difference equations*, Bull. Am. Math. Soc., 70 (1964), pp. 378–384.
- [99] L. R. MACK AND H. C. HARDEE, *Natural convection between concentric spheres at low Rayleigh numbers*, Int. J. Heat Mass Transfer, 11 (1968), pp. 387–396.
- [100] T. M. MACROBERT, *Spherical harmonics: an elementary treatise on harmonic functions with applications*, Dover, 1947.
- [101] W. V. MALKUS, *The heat transport and spectrum of thermal turbulence*, Proc. Math. Phys. Eng. Sci., 225 (1954), pp. 196–212.
- [102] P. MANNIX AND A. MESTEL, *Weakly nonlinear mode interactions in spherical rayleigh-bénard convection*, Journal of Fluid Mechanics, 874 (2019), pp. 359–390.
- [103] J. MARSHALL AND F. SCHOTT, *Open-ocean convection: Observations, theory, and models*, Rev. Geophys., 37 (1999), pp. 1–64.
- [104] R. T. MERRILL AND M. W. MCELHINNY, *The Earth's magnetic field: Its history, origin and planetary perspective*, vol. 401, Academic Press London, 1983.
- [105] K. MOHSENI AND T. COLONIUS, *Numerical treatment of polar coordinate singularities*, J. Comp. Phys., 157 (2000), pp. 787–795.
- [106] P. MOIN AND R. VERZICCO, *On the suitability of second-order accurate discretizations for turbulent flow simulations*, Eur. J. Mech. B/Fluids, 55 (2016), pp. 242–245.
- [107] M. MONNEREAU, M. CALVET, L. MARGERIN, AND A. SOURIAU, *Lopsided growth of Earth's inner core*, Science, 328 (2010), pp. 1014–1017.
- [108] D. NANDY AND A. R. CHOUDHURI, *Explaining the latitudinal distribution of sunspots with deep meridional flow*, Science, 296 (2002), pp. 1671–1673.

- [109] K. A. O'FARRELL, J. P. LOWMAN, AND H.-P. BUNGE, *Comparison of spherical-shell and plane-layer mantle convection thermal structure in viscously stratified models with mixed-mode heating: implications for the incorporation of temperature-dependent parameters*, Geophys. J. Int., 192 (2013), pp. 456–472.
- [110] P. OLSON, *Laboratory experiments on the dynamics of the core*, Phys. Earth Planet. Inter., 187 (2011), pp. 139–156.
- [111] P. OLSON AND G. CORCOS, *A boundary layer model for mantle convection with surface plates*, Geophys. J. Int., 62 (1980), pp. 195–219.
- [112] P. ORLANDI AND R. VERZICCO, *Vortex rings impinging on walls: axisymmetric and three-dimensional simulations*, J. Fluid Mech., 256 (1993), pp. 615–656.
- [113] T. OSCHMANN AND H. KRUGGEL-EMDEN, *A novel method for the calculation of particle heat conduction and resolved 3d wall heat transfer for the cfd/dem approach*, Powder Tech, 338 (2018), pp. 289–303.
- [114] M. PLUMLEY AND K. JULIEN, *Scaling laws in Rayleigh-Bénard convection*, Earth Space Sci., 6 (2019), pp. 1580–1592.
- [115] M. PLUMLEY, K. JULIEN, P. MARTI, AND S. STELLMACH, *The effects of Ekman pumping on quasi-geostrophic Rayleigh–Bénard convection*, J. Fluid Mech., 803 (2016), pp. 51–71.
- [116] D. A. RANDALL, T. D. RINGLER, R. P. HEIKES, P. JONES, AND J. BAUMGARDNER, *Climate modeling with spherical geodesic grids*, Computing in Science & Engineering, 4 (2002), pp. 32–41.
- [117] J. T. RATCLIFF, G. SCHUBERT, AND A. ZEBIB, *Steady tetrahedral and cubic patterns of spherical shell convection with temperature-dependent viscosity*, J. Geophys. Res. Solid Earth, 101 (1996), pp. 25473–25484.
- [118] F. M. RICHTER, *Convection and the large-scale circulation of the mantle*, J. Geophys. Res., 78 (1973), pp. 8735–8745.
- [119] P. H. ROBERTS AND E. M. KING, *On the genesis of the earth's magnetism*, Reports on Progress in Physics, 76 (2013), p. 096801.
- [120] T. ROLF AND J. P. TACKLEY, *Focussing of stress by continents in 3d spherical mantle convection with self-consistent plate tectonics*, Geophys. Res. Lett., 38 (2001).
- [121] M. ROSENFIELD, D. KWAK, AND M. VINOKUR, *A fractional step solution method for the unsteady incompressible navier–stokes equations in generalized coordinate systems*, J. Comput. Phys, 94 (1991), pp. 102–137.
- [122] H. ROSSBY, *A study of Bénard convection with and without rotation*, J. Fluid Mech., 36 (1969), pp. 309–335.

- [123] M. V. SALVETTI, P. ORLANDI, AND R. VERZICCO, *Direct simulations of transitional axisymmetric coaxial jets*, AIAA J, 34 (1995), pp. 736–743.
- [124] L. SANTELLI, P. ORLANDI, AND R. VERZICCO, *A finite-difference scheme for three-dimensional incompressible flows in spherical coordinates*, J. Comput. Phys., (2020), p. 109848.
- [125] ——, *A finite-difference scheme for three-dimensional incompressible flows in spherical coordinates*, J. Comput. Phys., (2020), p. 109848.
- [126] L. SANTELLI, G. WANG, D. LOHSE, R. J. STEVENS, AND R. VERZICCO, *Effect of gravity profiles on rayleigh-benard convection in spherical shells*, in APS Division of Fluid Dynamics Meeting Abstracts, 2020, pp. F16–019.
- [127] S. SCHMITZ AND A. TILGNER, *Heat transport in rotating convection without Ekman layers*, Phys. Rev. E., 80 (2009), p. 015305.
- [128] G. SCHUBERT, D. L. TURCOTTE, AND P. OLSON, *Mantle convection in the Earth and planets*, Cambridge University Press, 2001.
- [129] J. SCHUMACHER AND K. R. SREENIVASAN, *Colloquium: Unusual dynamics of convection in the Sun*, Rev. Mod. Phys., 92 (2020), p. 041001.
- [130] N. SCURTU, B. FUTTERER, AND C. EGBERS, *Three-dimensional natural convection in spherical annuli*, J. Phys. Conf. Ser., 137 (2008), p. 012017.
- [131] N. SCURTU, B. FUTTERER, AND C. EGBERS, *Pulsating and traveling wave modes of natural convection in spherical shells*, Physics of Fluids, 22 (2010), p. 114108.
- [132] R. SEYBOLDT AND F. JÜLICHER, *Role of hydrodynamic flows in chemically driven droplet division*, New J. of Phys, 20 (2018), p. 105010.
- [133] W. SHA, K. NAKABAYASHI, AND H. UEDA, *An accurate second-order approximation factorization method for time dependent incompressible navier-stokes equations in spherical polar coordinates*, J. Comp. Phys, 142 (1998), pp. 47–66.
- [134] M. H. SHAHNAS, J. P. LOWMAN, G. T. JARVIS, AND H.-P. BUNGE, *Convection in a spherical shell heated by an isothermal core and internal sources: Implications for the thermal state of planetary mantles*, Phys. Earth Planet. Inter., 168 (2008), pp. 6–15.
- [135] K. SHARIFF, R. VERZICCO, AND P. ORLANDI, *A numerical study of three-dimensional vortex ring instabilities: viscous corrections and early nonlinear stage*, J. Fluid Mech, 279 (1994), pp. 351–375.
- [136] O. SHISHKINA, R. J. A. M. STEVENS, S. GROSSMANN, AND D. LOHSE, *Boundary layer structure in turbulent thermal convection and its consequences for the required numerical resolution*, New J. Phys., 12 (2010), p. 075022.

- [137] B. I. SHRAIMAN AND E. D. SIGGIA, *Heat transport in high-Rayleigh-number convection*, Phys. Rev. A, 42 (1990), p. 3650.
- [138] E. D. SIGGIA, *High Rayleigh number convection*, Annu. Rev. Fluid Mech., 26 (1994), pp. 137–168.
- [139] E. A. SPIEGEL, *Convection in stars I. Basic Boussinesq convection*, Annu. Rev. Astron. Astrophys, 9 (1971), pp. 323–352.
- [140] M. SPRAGUE, K. JULIEN, E. KNOBLOCH, AND J. WERNE, *Numerical simulation of an asymptotically reduced system for rotationally constrained convection*, J. Fluid Mech., 551 (2006), p. 141.
- [141] S. STELLMACH, M. LISCHPER, K. JULIEN, G. VASIL, J. S. CHENG, A. RIBEIRO, E. M. KING, AND J. M. AURNOU, *Approaching the asymptotic regime of rapidly rotating convection: boundary layers versus interior dynamics*, Phys. Rev. Lett., 113 (2014), p. 254501.
- [142] R. J. A. M. STEVENS, H. J. H. CLERCX, AND D. LOHSE, *Optimal Prandtl number for heat transfer in rotating Rayleigh–Bénard convection*, New J. Phys., 12 (2010), p. 075005.
- [143] R. J. A. M. STEVENS, H. J. H. CLERCX, AND D. LOHSE, *Heat transport and flow structure in rotating Rayleigh–Bénard convection*, Eur. J. Mech. B Fluids, 40 (2013), pp. 41–49.
- [144] R. J. A. M. STEVENS, R. VERZICCO, AND D. LOHSE, *Radial boundary layer structure and nusselt number in Rayleigh–Bénard convection*, J. Fluid Mech., 643 (2010), pp. 495–507.
- [145] R. J. A. M. STEVENS, R. VERZICCO, AND D. LOHSE, *Radial boundary layer structure and Nusselt number in Rayleigh–Bénard convection*, J. Fluid Mech., 643 (2010), pp. 495–507.
- [146] R. J. A. M. STEVENS, J.-Q. ZHONG, H. J. CLERCX, G. AHLERS, AND D. LOHSE, *Transitions between turbulent states in rotating Rayleigh–Bénard convection*, Phys. Rev. Lett., 103 (2009), p. 024503.
- [147] H. SVENSMARK, *Cosmoclimatology: a new theory emerges*, Astronomy & Geophysics, 48 (2007), pp. 1–18.
- [148] H. SVENSMARK AND E. FRIIS-CHRISTENSEN, *Variation of cosmic ray flux and global cloud coverage—a missing link in solar-climate relationships*, Journal of atmospheric and solar-terrestrial physics, 59 (1997), pp. 1225–1232.
- [149] P. SWARZTRAUBER, *A direct method for the discrete solution of separable elliptic equations*, SIAM J. Num. Analysis, 11 (1974), pp. 1136–1150.

- [150] P. J. TACKLEY, *Effects of strongly variable viscosity on three-dimensional compressible convection in planetary mantles*, J. Geophys. Res. Solid Earth, 101 (1996), pp. 3311–3332.
- [151] F. TAKAHASHI, M. MATSUSHIMA, AND Y. HONKURA, *Simulations of a quasi-taylor state geomagnetic field including polarity reversals on the earth simulator*, Science, 309 (2005), pp. 459–461.
- [152] G. I. TAYLOR, *VIII. Stability of a viscous liquid contained between two rotating cylinders*, Philos. Trans. R. Soc. A, 223 (1923), pp. 289–343.
- [153] A. TILGNER, *High-Rayleigh-number convection in spherical shells*, Phys. Rev. E, 53 (1996), p. 4847.
- [154] A. TILGNER, *Spectral methods for the simulation of incompressible flow in spherical shells*, Int. J. Num. Methods Fluids, 30 (1999), pp. 713–724.
- [155] V. TRAVNIKOV, K. ECKERT, AND S. ODENBACH, *Linear stability analysis of the convective flow in a spherical gap with  $\eta = 0.714$* , International Journal of Heat and Mass Transfer, 80 (2015), pp. 266–273.
- [156] V. TRAVNIKOV, C. EGBERS, AND R. HOLLERBACH, *The geoflow-experiment on iss (part ii): Numerical simulation*, Advances in Space Research, 32 (2003), pp. 181–189.
- [157] E. P. VAN DER POEL, R. OSTILLA-MÓNICO, J. DONNERS, AND R. VERZICCO, *A pencil distributed finite difference code for strongly turbulent wall-bounded flows*, Computers & Fluids, 116 (2015), pp. 10–16.
- [158] R. VERZICCO AND P. ORLANDI, *A finite-difference scheme for three-dimensional incompressible flows in cylindrical coordinates*, J. of Comp. Phys, 123 (1996), pp. 402–414.
- [159] G. WANG, L. SANTELLI, D. LOHSE, R. VERZICCO, AND R. J. A. M. STEVENS, *Diffusion-free scaling in rotating spherical rayleigh-bénard convection*, Geophysical Research Letter, 48 (2021).
- [160] G. WANG, L. SANTELLI, R. VERZICCO, D. LOHSE, AND R. J. STEVENS, *Off-center gravity induces large-scale flow patterns in spherical rayleigh-bénard*, arXiv preprint arXiv:2105.03623, (2021).
- [161] M. WEDI, D. P. M. V. GILS, E. BODENSCHATZ, AND S. WEISS, *Rotating turbulent thermal convection at very large Rayleigh numbers*, J. Fluid Mech., 912 (2021), p. A30.
- [162] G. P. WILLIAMS AND J. B. ROBINSON, *Dynamics of a convectively unstable atmosphere: Jupiter?*, J. of Atmos. Sci, 30 (1973), pp. 684–717.

- [163] R. K. YADAV, T. GASTINE, U. R. CHRISTENSEN, L. DUARTE, AND A. REINERS, *Effect of shear and magnetic field on the heat-transfer efficiency of convection in rotating spherical shells*, Geophys. J. Int., 204 (2016), pp. 1120–1133.
- [164] T. YANAGISAWA AND Y. YAMAGISHI, *Rayleigh–Bénard convection in spherical shell with infinite Prandtl number at high Rayleigh number*, J. Earth Simulator, 4 (2005), pp. 11–17.
- [165] A. ZEBIB, G. SCHUBERT, AND J. M. STRAUS, *Infinite prandtl number thermal convection in a spherical shell*, Journal of Fluid Mechanics, 97 (1980), pp. 257–277.
- [166] K. ZHANG AND G. SCHUBERT, *Magnetohydrodynamics in rapidly rotating spherical systems*, Annu. Rev. Fluid Mech., 32 (2000), pp. 409–443.
- [167] X. ZHANG AND O. ZIKANOV, *Mixed convection in a horizontal duct with bottom heating and strong transverse magnetic field*, Journal of fluid mechanics, 757 (2014), pp. 33–56.
- [168] ——, *Two-dimensional turbulent convection in a toroidal duct of a liquid metal blanket of a fusion reactor*, Journal of Fluid Mechanics, 779 (2015), pp. 36–52.
- [169] J.-Q. ZHONG, R. J. A. M. STEVENS, H. J. CLERCX, R. VERZICCO, D. LOHSE, AND G. AHLERS, *Prandtl-, Rayleigh-, and Rossby-number dependence of heat transport in turbulent rotating Rayleigh–Bénard convection*, Phys. Rev. Lett., 102 (2009), p. 044502.
- [170] S. ZHONG AND M. GURNIS, *Mantle convection with plates and mobile, faulted plate margins*, Science, 267 (1995), pp. 838–843.
- [171] S. ZHONG, M. T. ZUBER, L. MORESI, AND M. GURNIS, *Role of temperature-dependent viscosity and surface plates in spherical shell models of mantle convection*, J. Geophys. Res. Solid Earth, 105 (2000), pp. 11063–11082.

